SPECTROSCOPIC STUDIES OF LASER PLASMAS FOR EUV SOURCES

by

SIMI A. GEORGE
B. S. Physics, Florida Atlantic University, 2002
B. S. Chemistry/Biochemistry, Florida Atlantic University, 2002
M. S. Physics, University of Central Florida, 2004

A dissertation submitted in partial fulfillment of the requirements
for the degree of Doctor of Philosophy
in the Department of Physics
in the College of Sciences
at the University of Central Florida
Orlando, Florida

Fall Term
2007

Major Professor: Martin C. Richardson

© 2006 Simi A. George

ABSTRACT

With the availability of high reflectivity multilayer mirrors and zone plate lenses, the EUV region (5nm - 40nm) of the electromagnetic spectrum is currently being explored for applications of nanoscale printing and imaging. Advances made in this area have consequences for many areas of science. Research for producing a compact, bright EUV source for laboratory use has gained momentum in recent years.

For this study, EUV radiation is produced by irradiating target materials using a focused laser beam. Focused laser beam ionizes the target to create a hot, dense, pulsed plasma source, where emission is a result of the relaxation of excited levels. Spectroscopy is used as the main diagnostic to obtain the spectral signature of the plasma.

Spectral characteristics are used to deduce the physical state of plasma, thus enabling the tuning of laser irradiance conditions to maximize the needed emission bandwidth. Various target materials are studied, as well as different target geometries, with spectroscopy below 200 nm on pulsed micro-plasmas being a particularly daunting task. Total range spectroscopy from 1 nm to greater than 1 micron is completed for tin-doped spherical droplet plasma source.

Reliable plasma diagnostics require both accurate measurements and solid theoretical support in order to interpret the experimental results. Using existing 1D-hydrocode, temperature and density characteristics of the expanding plasma is simulated for any set of experimental conditions. Existing atomic codes written for calculating one-electron radial wavefunctions with LS-coupling scheme via Hartree-Fock method is used in order to gain details of the ion stages, populations, transitions, etc, contributing to the spectral data.

To my mom, in memoriam

ACKNOWLEDGMENTS

First and foremost, I wish to express my deepest gratitude to Prof. Martin C. Richardson for giving me every opportunity available to become more than everything I ever thought possible. I have received guidance and kindness in abundance, without which it would have been truly impossible to go forward.

I would like to thank Dr. William T. Silfvast for encouragement and for being a true mentor alongside Dr. Richardson, for nourishing the hope and interest in me to go forward in science. Also, I am thankful to Dr. Silfvast for providing me with free-use of his lab and very expensive instrumentation which I had no idea how to use at the time.

Dr. Greg. Shimkaveg, for always knowing everything, for never turning me away with my questions, and for sharing those invaluable lessons learned in life. Dr. Moza Al-Rabban, for atomic physics calculations, and answering more questions.

I wish to thank Dr. Rob J. Gross for holding my hand through the early classes in physics, and for always willing to discuss and answer the questions I've had throughout the years in physics, mathematics, and computing. Cyndee Finkel and Melissa Troshinsky for being my sisters and best friends, compadres, and partners in mischief. Joshua Duncan for ChicK-fil-A and geeky, fun lunch discussions.

Rob Bernath, for being a true friend, for having patience in teaching me techniques that I was unfamiliar with in the laboratory. For always providing ideas, thus making my experience as a researcher much more pleasant that it would otherwise have been. Congratulations on your graduation, and I wish you all the joys life has to offer.

To Dr. Kazutoshi Takenoshita and Dr. Chiew-Seng Koay, for supporting me through

my training in EUV experiments and for conducting exemplary science as the technology moves forward, many thanks. Kazu, especially for providing peer teaching and mentoring, through the many experiments that proved quite challenging for me; thank you. Tobias Schmid and Jose Cunado for keeping my interests alive.

Everyone at LPL for being my family these last few years. Ji-Yeon Choi, Kelly McKirahan, Vani Kamtaprasad, Michael Hemmer, Mark Ramme, Tim McComb, Chris Brown, Troy Anderson, Matt Weidman, Dr. Santiago Palanco, etc, etc...thank you for all the help, conversations, fun times and support. You guys have made it all worthwhile.

Lastly, I would like to express my gratitude beyond what words can express, to my parents and my brother Ciju.

TABLE OF CONTENTS

LIST OF FIGURES . . . . **xvii**

LIST OF TABLES . . . . **xviii**

LIST OF ACRONYMS/ABBREVIATIONS . . . . **xix**

CHAPTER 1 INTRODUCTION **1**

1.1 EUV Radiation 1

1.2 Optics for the EUV region 3

1.2.1 Absorption and Optical Constants 4

1.2.2 Reflective Optics 6

1.2.3 Diffraction Optics 11

1.3 Need for Sources 14

1.3.1 EUV Lithography 15

1.4 Overview of thesis 17

1.5 References 18

CHAPTER 2 EUV SOURCE GENERATION **22**

2.1 Introduction 22

2.2 Continuous sources 23

2.2.1 Synchrotron Radiation Sources 24

2.2.2 Free Electron Lasers 28

2.3 Pulsed Plasma Sources 29

2.3.1 Discharge Sources 30
2.3.2 EUV/soft x-ray Lasers, and Femtosecond High-Harmonic EUV Generation 31
2.3.3 Laser Plasmas 32
2.4 Target Materials for EUV Generation 34
2.5 References 36

CHAPTER 3 THE PHYSICS OF LASER-PRODUCED PLASMA SOURCES 43
3.1 Introduction 43
3.2 Absorption of Laser Light in a Plasma 43
3.2.1 Critical Electron Density 46
3.2.2 Inverse Bremsstrahlung 47
3.2.3 Resonance absorption 50
3.3 Hydrodynamic Simulations of Laser Plasmas in Lagrangian Coordinates . . . 50
3.4 References 55

CHAPTER 4 PLASMA SPECTROSCOPY 58
4.1 Introduction 58
4.2 Atomic Structure and Spectra 59
4.2.1 Selection Rules 60
4.2.2 Isoelectronic Sequences 61
4.2.3 Transition Probabilities 61
4.2.4 The Principle of Detailed Balance 65
4.3 Plasma in Thermal Equilibrium: Black-Body Radiation Distribution 65

4.4 Emission of Electromagnetic Radiation from Plasmas 68
4.4.1 Bremsstrahlung Continuum 69
4.4.2 Recombination Continuum 70
4.4.3 Line Emission 71
4.4.4 Broadening Mechanisms in Line Radiation 71
4.4.5 The Inglis-Teller Limit 76
4.4.6 Unresolved Transition Arrays and Super Transition Arrays 76
4.5 Equilibrium Conditions for Population Distributions in Plasmas 77
4.5.1 Atomic Processes in Population Kinetics 77
4.5.2 Local Thermodynamic Equilibrium 79
4.5.3 Non-LTE Collisional Radiative Equilibrium Model 80
4.5.4 Coronal Equilibrium Model 82
4.6 Spectroscopy as a plasma diagnostic 83
4.7 References 83

CHAPTER 5 EUV GENERATION FROM PLANAR SOLID TIN TARGET 86

5.1 Introduction 86
5.2 Tin as a Target Material for Plasma EUV source 88
5.2.1 Hydrodynamics and CRE model Calculations for Plasma Dynamics . 89
5.2.2 Atomic Level Structure Determinations 91
5.2.3 Calculated Oscillator Strengths of Transitions 92
5.3 Experimental Arrangements 97
5.3.1 High repetition rate (100Hz) Nd:YAG laser system 97
5.3.2 Vacuum Chamber and Set-up 98

5.3.3 Flat-Field EUV Spectrometer 99
5.3.4 Flying Circus EUV Energy Detector 103
5.4 Experimental Results 104
5.4.1 Spectral Measurements as a Function of Intensity 105
5.4.2 Conversion Efficiency and Calculation Methods 109
5.5 Discussion 115
5.6 Summary 116
5.7 References 116
CHAPTER 6 EUV GENERATION FROM SOLID TIN AND SOLID LITHIUM: A COMPARISON 121
6.1 Introduction 121
6.2 Plasma Generation 122
6.3 Experimental Arrangements 123
6.3.1 Laser 123
6.3.2 Chamber and Instrumentation 125
6.4 Experimental Results 127
6.4.1 Spectral Measurements as a Function of Intensity 127
6.4.2 CE as a function of laser irradiance intensity 129
6.4.3 Debris studies 132
6.5 Comparison to Calculations 132
6.5.1 Atomic Level Structure Determinations 135
6.5.2 Radiation Transport 137
6.6 Discussion 139
6.7 Summary 140

6.8 References 140

CHAPTER 7 CALIBRATED BROAD-BAND SPECTROSCOPY OF SN-DOPED DROPLET LASER PLASMAS 142

7.1 Introduction 142

7.2 High-Repetition Rate Tin-doped Droplet Laser Produced Micro-plasma Source 142

7.2.1 Need for Out-of-Band Emission Studies 143

7.3 Experimental Arrangements 145

7.3.1 Tin-doped Droplet Generation 146

7.4 Emission from Tin-doped Droplets 148

7.4.1 In-band Spectroscopy and Metrology 148

7.4.2 Broad-band EUV Spectroscopy 151

7.4.3 VUV Spectroscopy 153

7.4.4 Visible/IR Spectrocopy 156

7.5 Broad-band spectrum 157

7.6 Summary 160

7.7 References 160

CHAPTER 8 EUV GENERATION WITH A FIBER LASER 163

8.1 Introduction 163

8.1.1 Target System and Configuration 163

8.2 Fiber Laser System 164

8.3 Experimental Configuration 165

8.4 Results 168

8.4.1 Results from pre-plasma generation 168

8.4.2 Results without pre-plasma generation 170
8.4.3 Effects of laser pulse duration on EUV generation 170
8.4.4 Tin debris on lens 171
8.5 Discussion 172
8.6 References 174

CHAPTER 9 CONCLUSION AND FUTURE WORK 178

9.1 Summary 178
9.2 References 181

APPENDIX: LIST OF PAPERS 182

LIST OF FIGURES

1.1 The electromagnetic spectrum. 2
1.2 Kirkpatrick-Baez focusing mirror system [2]. 8
1.3 Multilayer interference coating principles [2]. 9
1.4 Theoretical reflectivity of a Mo-Si multilayer at normal incidence, obtained from the online calculator provided by CXRO [15]. 10
1.5 Illustration of diffraction from a transmission grating. Zeroth and ±1 orders are shown [2]. 12
1.6 Focus formation with a Fresnel zone plate lens [2]. 13
1.7 General schematic of EUVL stepper system design using reflective optics [22], and example of structures printed with EUV radiation taken from ref. [2] . . 16

2.1 Comparison of average spectral brightness of various short wavelength sources. 23
2.2 Early synchrotron facilities, and modern storage rings optimized for high brightness with inclusion of wigglers, undulaters, and bending magnets for turning. Figure reproduced with permission from [2] 25
2.3 Methods of generating radiation from bending magnets, undulators, and wigglers at a synchrotron [2, 11]. 27
2.4 EUV emission as function of atomic number 35

3.1 Cartoon of laser interaction with target surface leading to EUV emission. . . 45

4.1 He-like atom energy level structure showing various atomic processes [16] . . 80

4.2 CRE model calculaiton of Xenon ionic charge densities as function of temperature 82

5.1 Spectrum from a Xenon plasma source in the EUV region [8]. 87
5.2 Plasma electron temperature and density expansion as function of distance at the peak of the laser pulse. Modeled using 200-cell MED103 for a 1064 nm, 10 ns gaussian beam irradiating solid Sn target. 90
5.3 Population distribution as a function of temperature calculated using the CRE model. 91
5.4 Relative Energy levels in Sn^{11+} and Sn^{7+} [13, 12]. 94
5.5 COWAN code calculated transition probabilities for Sn atoms contributing to emission in the 13 nm -14 nm region 95
5.6 COWAN code calculated transition probabilities fitted with a gaussian to generate a spectral distribution for the Sn ions contributing to EUV emission [15, 14] 96
5.7 1 Hz laser and a schematic of the optical layout 98
5.8 Measure far-field beam profile from the 1Hz, 1064 nm laser beam, and the plot of the focal spot region of the 1064 nm beam through a 100 mm lens. The lens is translated in 200 μm steps 99
5.9 Chamber and set-up for planar tin measurements 100
5.10 Rowland circle 101
5.11 Flat-field Spectrometer and design 102
5.12 The Flying Circus EUV energy detector and the measurement scheme of one of the channels [27] 103
5.13 Calibration curves obtained from NIST for the EUV detector components . . 106

5.14 Spectral measurements obtained for pplanar Sn target as the intensity is varied by varying the laser beam focal diameter. Maximum counts are observed for an intensity of 1×10^{11} W/cm^2 107
5.15 The spectra are normalized with respect to the peak emission. The small feature sizes of the spectrum remain at the same position as intensity is increased. The changes predominantly occur in the UTA. The shift to 13.5nm and the narrowing is more obvious here 109
5.16 Intensity and lens spot size dependencies of measured conversion efficiency for 13.5 nm 114
5.17 Conversion efficiency as a function of laser energy 115

6.1 Measured far-field laser beam profile for the 10 Hz laser 124
6.2 Measured focal range of the lens used in the experiments used for calculating irradiances 125
6.3 Experimental configuration of the chamber and instrumentation 126
6.4 Spectrum from a planar lithium laser plasma source in the EUV region as function of laser intensity 128
6.5 Spectra from the planar tin laser plasma source in the EUV region 130
6.6 Highest conversion efficiencies measured for both planar tin and lithium targets 131
6.7 Processed images of the debris deposited on silicon wafer sample surfaces, obtained using optical microscopy 133
6.8 Spectrum from a Li laser plasma source in the EUV region 134
6.9 Lithium charge-state distribution as a function of temperature for two different electron densities 136
6.10 Calculated transition lines for Li^{+} and Li^{2+} ions 138

6.11 CRETIN 2D-radiation transport code [8, 6] calculated spectrum from of lithium laser plasma source at 13.5 nm 139

7.1 Spectrum from water droplet plasma source in the EUV region [3] 144
7.2 Photograph of a thin chain of droplet targets together with a cartoon of a laser beam focused on a droplet 147
7.3 EUV emission in the 12 nm - 20 nm region from Sn-doped droplets at various concentrations 149
7.4 (a) In-band emission spectra and (b) high conversion efficiencies measured from tin-doped droplet targets 150
7.5 Images of the Sn EUV plasma as the focal diameter at the droplet target is varied by translating the lens from from one position to the next. 151
7.6 Picture and schematic of the transmission grating spectrometer 152
7.7 TGS spectral measurements obtained sn-doped droplets in the EUV region from 1 - 28 nm at an intensity of 1.0×10^{11} W/cm^2 153
7.8 Observed lines from all oxygen lines compiled by the National Institute of Standards and Technology 154
7.9 Spectral measurement sn-doped and pure water droplets in the VUV region . 155
7.10 Visible emission from sn-doped droplet targets at optimum EUV emission conditions 159
7.11 Complete spectral emission from the tin-doped droplet target at conditions optimum for EUV emission. Different spectrometric configurations were used for detection of emission into the different wavelength regions. The y-axis units are not used in this plot since the different instruments are not cross calibrated against each other. 162

8.1 The picture of the fiber laser 165

8.2 Yb-doped fiber laser schematic 166

8.3 Chamber set-up and diagnostics 167

8.4 Best results obtained for 13.5 nm generation from the series of experiments conducted using fiber laser. 169

8.5 Energy measurements obtained without the generation of pre-plasma for scale-length optimization. Energies measured are much lower. 171

8.6 Comparing the effect of pulse duration on plasma temperature. 172

8.7 Sn particulates deposited on the lens during an experiment with tin droplets. 173

8.8 Comparison of fiber laser spectral measurement to the highest Nd:YAG laser measurement for the same target 174

LIST OF TABLES

1.1 Joint Requirements for EUV Sources, Barcelona, 2006 17

3.1 Critical densities for some common laser wavelengths 47

5.1 Permitted LS terms for d^n subshells. The subscripts indicate the number of different terms having the same value of LS. All of them are even parity [13]. 93

LIST OF ACRONYMS/ABBREVIATIONS

BW	Bandwidth
CE	Conversion efficiency
CEM	Coronal equilibrium model
CRE	Collisional-radiative equilibrium model
CXRO	Center for X-ray optics
DPP	Discharge produced plasmas
EM	Electro-magnetic
ETS	Engineering test stand
EUV	Extreme ultraviolet
EUVL	Extreme ultraviolet lithography
FEL	Free electron laser
FZP	Fresnel zone plate
HHG	High harmonic generation
IBA	Inverse Bremsstrahlung absorption
IF	Intermediate focus
KE	Kinetic energy
LPP	Laser produced plasmas
LTE	Local thermal equilibrium
MCP	Microchannel plate
ML	Multilayer
MLM	Multilayer mirror
NA	Numerical aperture

OPC	Optical proximity correction technique
PLD	Pulsed laser deposition
PLL	Phase lock loop
SASE	Self amplified spontaneous emission
SRIM	Stopping and range of ions in matter
UV	Ultraviolet
YAG	Yttrium aluminum garnet

CHAPTER 1
INTRODUCTION

1.1 EUV Radiation

In older literatures, the region with wavelengths shorter than 200 nm and longer than x-rays are collectively referred to as the vacuum ultraviolet (VUV). This was because all of the instrumentation used for detecting these wavelengths needed to be evacuated. Recent literature further distinguishes the VUV wavelengths into three separate areas; the Shumann ultraviolet [1] or VUV, the extreme ultraviolet (EUV or XUV), and the soft x-rays. Literatures differ on the exact spectral limits for these proposed regions, and wavelength designations tend to overlap each other. For the purposes of this thesis, the most recent published definitions will be used (Fig.1.1). In this thesis, the EUV region is defined to be the wavelengths between 40 nm (30 eV) and 5 nm (250 eV) and the soft x-ray region is specified to cover the spectral region from 5 nm - 0.3 nm [2].

The EUV and soft x-ray wavelengths have not been well explored for science and engineering. There are several reasons for this treatment. The penetration length or the absorption length of these radiations are very small in almost all materials; generally less than 1μm. Thus, photons at these wavelengths are strongly attenuated in nature and require vacuum environment for applications. These wavelengths are not small enough to meet Bragg reflection conditions for most crystals in x-ray diffraction (below 1 nm) and they are not significantly reflected by optical surfaces at normal incidence. Combining these unique properties of EUV/soft x-rays with the lack of powerful light sources, detectors, and optics,

inhibited exploration of this region.

If these problems can be overcome, many areas of science and technology can be advanced by utilizing EUV and soft x-rays. In microscopy, short wavelength radiation can bridge the gap between optical and electron microscopes by providing sub-100 nm resolution for imaging live cells [3]. Cell damage and subsequent regeneration/self-repairs can be studied with large dose short wavelength radiation at picosecond durations. These photon energies match the primary atomic resonances of many elements, thus providing numerous applications in elemental and chemically specific spectroscopies in surface physics, materials science, and chemistry. The availability synchrotron radiation and advances in the development of highly reflective optics and diffractive optical elements (fresnel zone plates) have brought this wavelength region into the forefront of research and innovation. These include fundamental investigations in materials science and engineering, dynamics of molecular reactions in real time for chemistry, high resolution cell studies in biology near the water-window region, and patterning nano-structures for lithography [2]. Thus, many areas of science have seen rapid development in the last two decades utilizing EUV and soft x-ray radiations as a

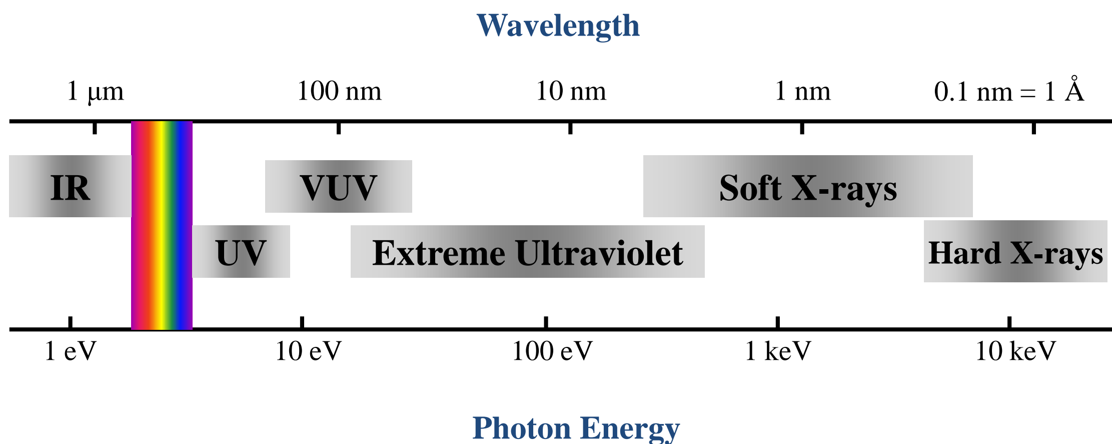

Figure 1.1: The electromagnetic spectrum.

tool for fundamental investigations.

1.2 Optics for the EUV region

An optical system (optical microscopes or telescopes) for visible light, typically consisting of lenses or mirrors, performs fourier transforms and inversions in one operation without resulting in information loss within in the limits of the system resolution. For such an image-forming system, the limit of the resolution is often defined using the Rayleigh criterion. The resolving power defined by the Rayleigh criterion for an optical system at some distance δx or at some angle $\delta\theta$ is given by

$$R = 1.22\frac{\lambda}{2NA} \tag{1.1}$$

and the depth of focus is

$$DOF = \pm 0.5\frac{\lambda}{(NA)^2} \tag{1.2}$$

where λ is the wavelength, and $NA = \sin\theta$ is the numerical aperture [4]. The wavelength of illumination is the resolution limit where details significantly smaller than λ cannot be resolved or reconstructed. Mirrors with multilayer (ML) coatings based on the Bragg reflection principles, and diffractive optical elements such as Fresnel zone-plate lenses allow for the use of short wavelength radiation. Detailed overview of the principles behind these optical elements are provided in later sections (1.2.2 and 1.2.3). As can be seen from Eq. 1.1, the use of EUV radiation extends the capability of classical optical techniques to resolve details that are only a few nanometers.

1.2.1 Absorption and Optical Constants

As stated previously, EUV and soft x-rays are attenuated in materials. Absorption depends on the optical properties of materials, thus knowledge of the interaction of this radiation with matter is necessary. The interaction of EUV/soft x-rays with matter involve photoabsorption and coherent scattering by bound electrons where it is assumed that condensed matter may be modeled as a collection of non-interacting atoms. This assumption is usually valid since the photon energies in this region is much larger than the molecular binding energies and the optical properties are determined by tightly bound core electrons, not the chemical state of atoms. Efforts to provide a short background into the optical components and principles follow.

The Drude model [5] is described in many texts for the classical case of an electron oscillating in an electric field $\mathbf{E}$, where it is shown that the refractive index has a strong dependence on electron oscillation frequency. The Drude model considers the valence electrons in metals to be free. With an electric field applied, the electric displacement, $\mathbf{D}$, is related to the macroscopic polarizability, $\mathbf{P}$, $\mathbf{D} = \varepsilon\mathbf{E} = \mathbf{E} + 4\pi\mathbf{P} = \mathbf{E} + 4\pi N_e\alpha$, where N_e is the free electrons per unit volume, and the polarizability, α is defined as [6]

$$\alpha = \frac{-e^2/m}{\omega^2 + i\omega\gamma} \tag{1.3}$$

where ω is the frequency of oscillations, and γ is the damping constant. The dielectric constant is then

$$\varepsilon = 1 - \frac{\omega_p^2}{\omega^2 + i\omega\gamma}; \quad \omega_p^2 = 4\pi N_e r_e c^2 \tag{1.4}$$

where ω_p is the plasma frequency with the classical electron radius r_e. Then the index of refraction can be related to the dielectric constant by

$$n = \sqrt{\varepsilon} = 1 - \delta + i\beta \tag{1.5}$$

where δ is the refractive index decay and β is the extinction coefficient. The real part of the refractive index approaches unity for short wavelength radiation and the absorption is strong.

For the many atom case, the optical properties are approximated by summing the individual responses of atoms and related to the complex atomic scattering factor, f, where

$$f = f_1 - if_2 \tag{1.6}$$

and

$$n = 1 - \delta + i\beta = 1 - \frac{n_a r_e \lambda^2}{2\pi}[f_1 - if_2] \tag{1.7}$$

where λ is the wavelength in vacuum, n_a is the average density of atoms in material, r_e is the classical electron radius. f_1 relates the phase velocity variation to the complex atomic scattering factor, and the imaginary component f_2 relates the wave amplitude decay due to absorption [2]. δ and β then are

$$\delta = \frac{n_a r_e \lambda^2}{2\pi}[f_1], \quad and \quad \beta = \frac{n_a r_e \lambda^2}{2\pi}[f_2] \tag{1.8}$$

The imaginary part of the index of refraction β for absorption is experimentally determined, where the absorption length or the exponential decay length in materials is inversely proportional to β,

$$l_{abs} = \frac{\lambda}{4\pi\beta} \tag{1.9}$$

Then the dispersive part δ can be calculated using the Kramers-Kronig or dispersion relations [2]. Henke et. al. tabulated values for elements from 1 - 92 for energies from 50 eV to 30 keV, and these can be found in ref. [7]. Many other methods for determining optical constants are available and details can be found in references listed in [8]. Strong absorption of short wavelength radiation demands the use of novel reflective and diffractive optics.

1.2.2 Reflective Optics

Reflection of short wavelength radiation at normal incidence and at various angles of incidence are minimal. One exception is very small glancing angles with the angle reflection depending on the material and wavelength. But even at these small grazing angles, the total reflection is less than unity. Utilizing the concept of total external reflection at glancing incidences and enhancing reflectivity using periodic structures are two methods by which optics are designed for relaying soft x-rays and EUV radiation for investigations. An overview of principles applied and applications of these methods are given in the following sections.

The basic equations governing the reflection of an electromagnetic wave incident upon an interface of two materials with differing refractive indices are the Fresnel equations [2, 9, 10]. The reflectivity amplitude for the two cases, where the the electric field, **E** is perpendicular to the plane of incidence (s-polarization) and **E** parallel to the plane of incidence (p-polarization) is given below.

$$R_{s,\perp} = \frac{|E_{0r}|^2}{|E_{0i}|^2} = \left| \frac{n_i \cos\phi_i - n_t \cos\phi_t}{n_i \cos\phi_i + n_t \cos\phi_t} \right|^2 \tag{1.10}$$

$$R_{p,\parallel} = \frac{|E_{0t}|^2}{|E_{0i}|^2} = \left| \frac{n_t \cos\phi_i - n_i \cos\phi_t}{n_i \cos\phi_t + n_t \cos\phi_i} \right|^2 \tag{1.11}$$

where $\phi_{i,r,t}$ are the angles on incidence, reflection, and transmission respectively and n is the complex refractive index. For normal incidence ($\phi = 0$) at $n_i = 1$, we have

$$R_{s,\perp} = \frac{|1 - n_t|^2}{|1 + n_t|^2} \tag{1.12}$$

For short wavelength radiation, with $n_t = 1 - \delta + i\beta$, $\delta \ll 1$, and $\beta \ll 1$ we have the following solution,

$$R_{s,\perp} \simeq \frac{\delta^2 + \beta^2}{4} \tag{1.13}$$

For this case, the result is identical in the p-polarization case, with reflectivities in the order of 10^{-5}. Basically, this tells us that at normal incidences, the reflectivity of EUV/soft x-rays are too small to be of use with single layer mirrors.

At glancing incidences, for soft x-ray/EUV radiation, Snell's law for a refractive index of $n \simeq 1 - \delta$, with $\beta \to 0$, the critical angle for total external reflection is found to be [2]

$$\theta_c = \sqrt{2\delta}; \quad \theta < \theta_c; \quad \theta + \phi = 90 \tag{1.14}$$

In the case of s-polarization, with $\theta = 90^\circ - \phi \leq \theta_c$, and $\theta_c \ll 1$, we have the solution,

$$R_{s,\theta} = \frac{\left|\theta - \sqrt{(\theta^2 - \theta_c^2) + 2i\beta}\right|^2}{\left|\theta + \sqrt{(\theta^2 - \theta_c^2) + 2i\beta}\right|^2} \tag{1.15}$$

at glancing incidences. In the case of p-polarization and complex n, a minimum in the reflectivity or Brewster's minimum occurs at an angle given by $\tan\phi_B = 1 - \delta$, or

$$\phi_B \simeq \frac{\pi}{4} - \frac{\delta}{2} \tag{1.16}$$

Use of these principles are demonstrated in a number of ways as outlined.

Glancing-Incidence Optics

The critical angle for total external reflection at glancing incidences, θ_c, is proportional to $\lambda\sqrt{Z}$ in the first order. This means that the reflection curve of the optics for short wavelengths depends on the mirror materials and the wavelength. Reflectance spectra for common mirror materials are given by W. R. Hunter in [8] and more complete reference can be found in [7]. The most commonly used imaging set-up is the Kirkpatrick-Baez focusing mirror system (Fig. 1.2) for microscopy, where two spherical mirrors placed orthogonal to

each other[10]. The sagittal focus from the first spherical mirror is used as the source point for the second spherical mirror with strong focus in the tangential direction. This combination provides a real image with proper separation of focal lengths. Another imaging system in use presently is the Wolter systems, utilizing the imaging properties of conicoidal surfaces [11]. There are other compound systems for imaging, discussed by J. H. Underwood in [8], but all are limited in capabilities for high resolution and efficiency.

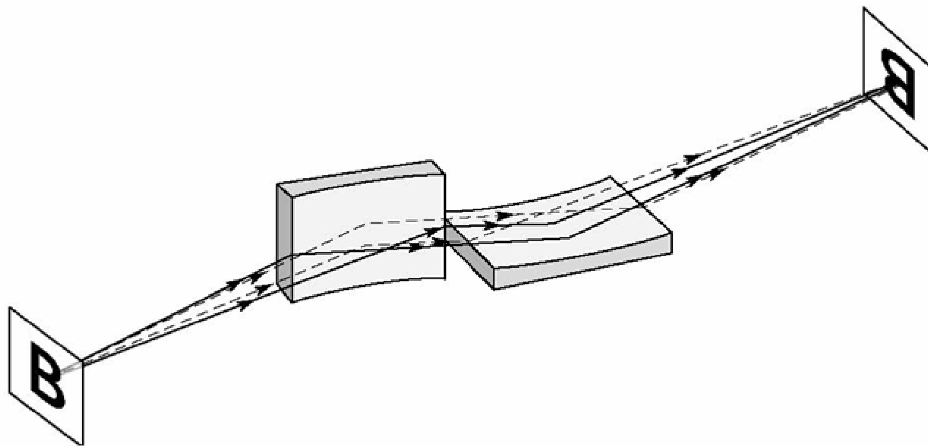

Figure 1.2: Kirkpatrick-Baez focusing mirror system [2].

Multilayer Mirrors

Multilayer (ML) reflective coatings are polycrystalline in nature, consisting typically of two materials in alternating high and low atomic number (Z) layers. Essentially these are artificial Bragg reflectors. Scattering from these periodic structures (Fig. 1.3) conform to Bragg's law corrected for refraction as given below.

$$m\lambda = 2d\sin\theta\sqrt{1-\frac{4\bar{\delta}d^2}{m^2\lambda^2}} \tag{1.17}$$

where m is the diffraction order, d is the periodicity, and δ is the bilayer weighted real part of the refractive index [2]. Thin high Z material provides scattering and minimizes absorption, while the low Z material acts as a spacer with as little absorption as possible for interface contrast. Each layer is a few atoms thick and each layer pair periodicity ($d = \lambda/2$) is for normal incidence illumination at wavelength λ.

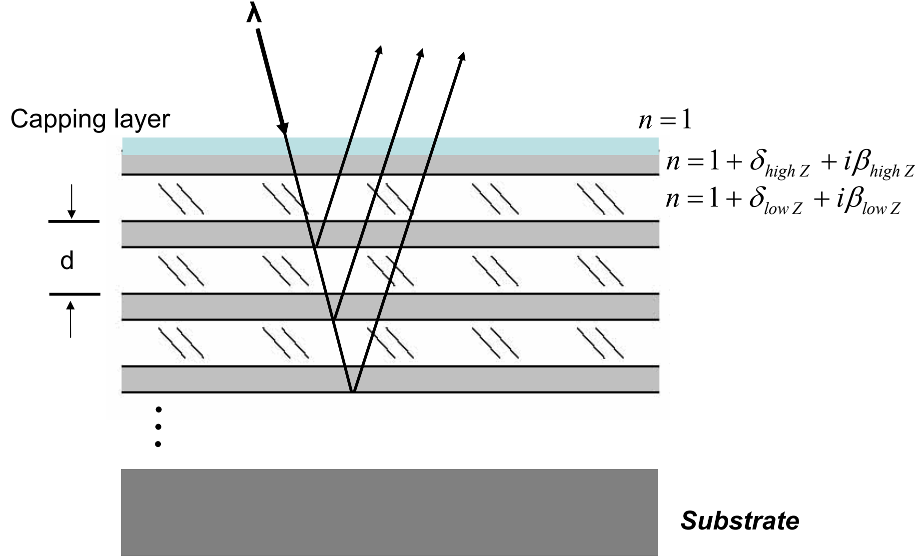

Figure 1.3: Multilayer interference coating principles [2].

An important design parameter for the asymmetric ML coating is the ratio of the high Z material thickness to the bilayer period, denoted as Γ, where

$$\Gamma = \frac{\triangle t_H}{\triangle t_H + \triangle t_L} = \frac{\triangle t_H}{d} \tag{1.18}$$

$\triangle t_H$ is the thickness of the high Z layer, $\triangle t_L$ is the thickness of the low Z layer, totaling the bilayer period d. At normal incidence, Γ is optimized as follows,

$$\tan(\pi\Gamma_{opt}) = \pi \left[\Gamma_{opt} + \frac{\beta_L}{\beta_H - \beta_L}\right] \tag{1.19}$$

where Γ_{opt} is the optimum value of Γ, and β_L and β_H are the absorptive components for the index of refraction for the low and high atomic number materials [2, 12]. Reflectivities over 70% have been achieved for multilayer structures [13, 14] at 13 nm.

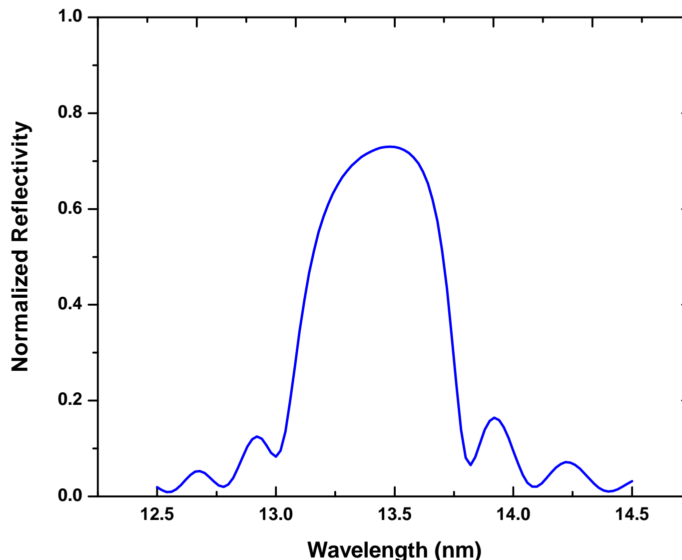

Figure 1.4: Theoretical reflectivity of a Mo-Si multilayer at normal incidence, obtained from the online calculator provided by CXRO [15].

ML coatings can easily be adapted to curved surfaces such as mirrors and gratings, and a variety of different coatings optimized at many different EUV and soft x-ray wavelengths are available today. ML mirrors (MLM) are currently being utilized for photoemission microscopy for surface science (13.5 nm, 9.54 nm), astronomical imaging applications with the use of large collection solid angle optics (Cassini Cassegrain telescope, 17.3 nm), extreme ultraviolet lithography (EUVL) using 13.5 nm source, plasma diagnostics (13.5 nm), polarization studies of magnetic materials (soft x-rays), and x-ray microprobes (soft x-rays) [2]. The highest reflectivity achieved at 70% is for alternating layers of Molybdenum (Mo) and Silicon (Si) for a bandwidth centered at 13.5 nm and this is plotted in Fig. 1.4) [2, 15].

1.2.3 Diffraction Optics

Propagating light waves incident on spatial discontinuities in refractive index (sharp edges) are redirected at specific angles of order, $\theta \sim \lambda/d$. This process is labeled diffraction. The diffracted light interferes with un-diffracted radiation causing light and dark fringes. From very early days of spectroscopy, transmission gratings with many parallel lines and spaces have been utilized to diffract light for wavelength separation (Fig. 7.6). Incident radiation at an angle, θ_i from the normal, the grating equation is given to be,

$$m\lambda = d(\sin\theta - \sin\theta_i) \tag{1.20}$$

where d is grating period, λ is the wavelength, θ is the dispersion angle, and m is the diffracted orders of 0, ± 1, ± 2, $\cdots$ etc. The intensity of energy into the various diffracted orders depend on the complex refractive index affecting the absorption and phase shift in the grating, and the nature of the periodic structure which are the sharpness of profile, and line width. For a transmission grating of opaque lines of width equal to half the grating period, the efficiencies $\eta_m = I/I_0$ of the diffraction in to various orders is given as [2]

$$\eta_m = \begin{cases} 0.25 & \text{m} = 0 \\ 1/m^2\pi^2 & \text{m odd} \\ 0 & \text{m even} \end{cases} \tag{1.21}$$

Fresnel zone plate lens

A Fresnel zone plate (FZP) lens is basically a circular, symmetric diffraction grating with zonal periods adjusted to have shortening of the periods at increasing radius from the optical axis. Alternating and successive, transmissive and opaque zones are constructed so

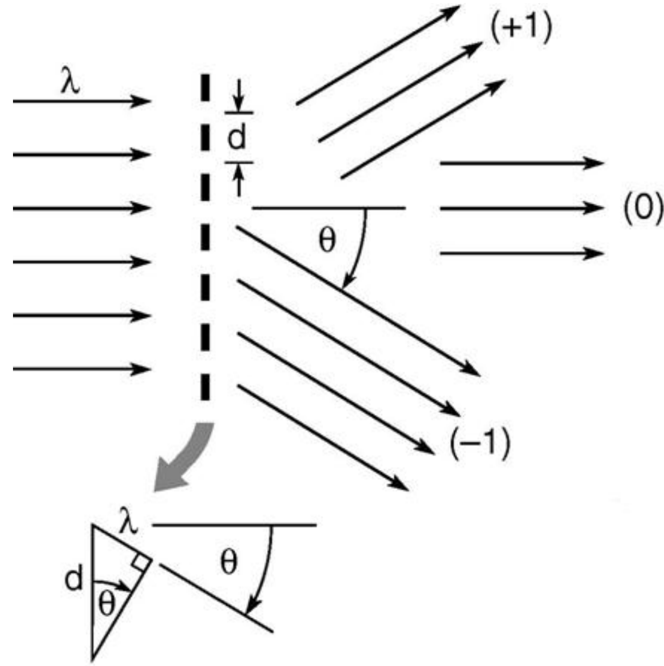

Figure 1.5: Illustration of diffraction from a transmission grating. Zeroth and ±1 orders are shown [2].

as to add $\lambda/2$ successive path lengths. The incident light is diffracted radially inward to the optical axis, and $\sin\theta = \lambda/d$, shortened periods result in larger diffraction angles, giving a real first order focus. A illustration of this is given in (Fig. 1.6), obtained from reference [2]. For a given zone plate with focus at a distance f, the zonal radii are given by the Pythagorean theorem

$$f^2 + r_n^2 = \left(f + \frac{n\lambda}{2}\right)^2 \tag{1.22}$$

$$r_n^2 = n\lambda f + \frac{n^2\lambda^2}{4} \tag{1.23}$$

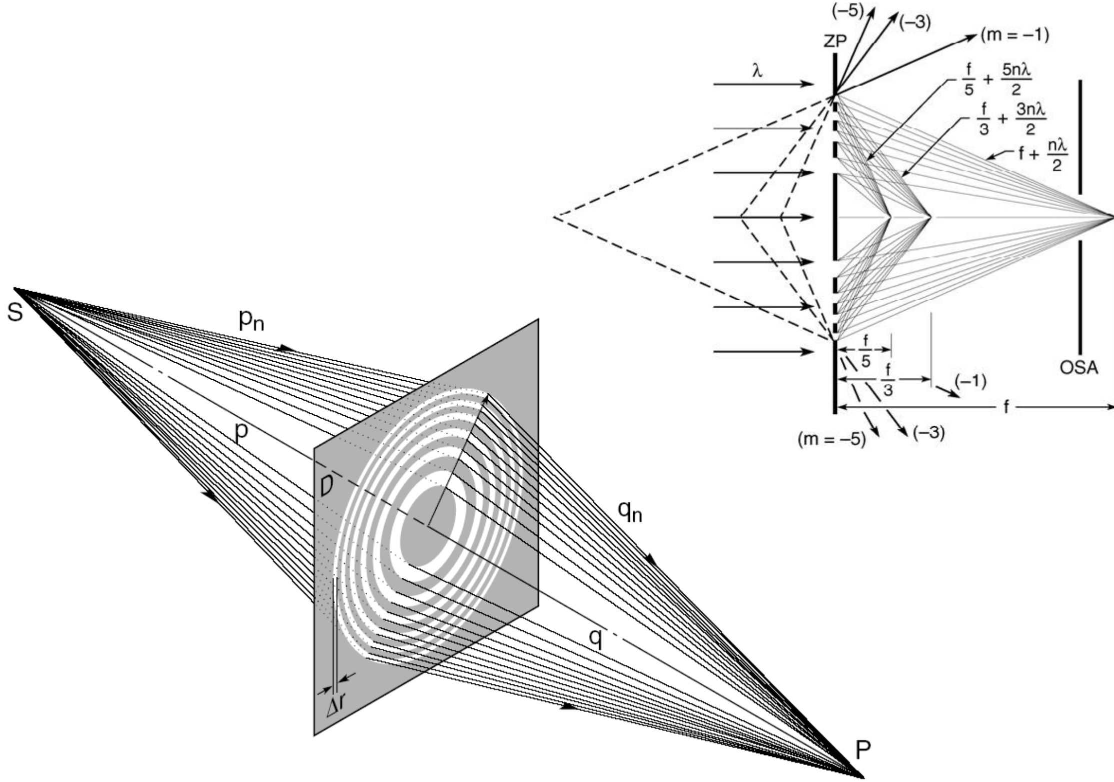

Figure 1.6: Focus formation with a Fresnel zone plate lens [2].

where r_n is the radius of any zone. For EUV/soft x-rays, $\lambda \ll f$, thus the numerical aperture is small and the second term which represents spherical aberration is ignored to give

$$r_n \simeq \sqrt{n\lambda f} \tag{1.24}$$

To describe the properties of a zone plate lens, the following definition is used.

$$\triangle r \equiv r_N - r_{N-1} \tag{1.25}$$

where N is the total number of zones, and $\triangle\ r$ is the outer zone width. Then the total diameter of the lens is given by

$$D \simeq 4N\triangle r \tag{1.26}$$

The focal length is then,

$$f \simeq \frac{D\triangle r}{\lambda} \simeq \frac{4N(\triangle r)^2}{\lambda} \tag{1.27}$$

which shows that the focal length of a zone plate is directly dependent on the number of zones. The numerical aperture of a lens is, $NA = \sin\theta$, where θ is the half angle from focus to the lens along the optical axis. NA of the zone plate lens is

$$NA \simeq \frac{\lambda}{2\triangle r} \tag{1.28}$$

The depth of focus of the zone plate is given by

$$DOF = \pm 2F^{\#2}\lambda = \frac{\pm(\triangle r)^2}{\lambda} \tag{1.29}$$

This provides the basic framework of a zone plate lens, and we can immediately see that the spatial resolution limit is set by the outer zone width $\triangle r$. The practical limitation in resolution at present is the ability to construct smaller zone structures. A more detailed theoretical framework can be found in references [2, 4, 16, 8, 17] including discussions about inaccuracies, fabrication limitations and aberrations. Zone-plates are typically used for soft x-ray microscopy near the water window, but multilayer fabrication of zone plates for 13 nm radiation have been demonstrated [18, 8]. Outer zone widths of 15 nm have been demonstrated [19] and magnetic soft x-ray microscopy at 15 nm resolution for probing nano-scale local magnetic hysteresis was published recently [20].

1.3 Need for Sources

A short wavelength source that does not require researchers to take their experiments to synchrotron facilities has become a necessity for many areas of science. Although

synchrotrons are a powerful source of EUV and soft x-rays, wait times on sychrotrons are long, it is expensive, with unpredictable amount down time, etc. Other sources in this spectral region have not been able to provide the flux needed for use with the optics available. Most sources available may have high average power, but instantaneous energies were low. These problems have lead researchers to seek alternate methods for generating EUV and soft x-rays. Some of this include EUV lasers, high harmonic generation (HHG), and pulsed plasma sources [2].

Current research for EUV sources is driven by the semiconductor manufacturing industry. To extend the life of current silicon microprocessor technology for creating smaller, powerful chips with greater number of transistors embedded, extreme ultraviolet lithography (EUVL) is being developed as the most promising alternative to deep ultraviolet lithography. A feasible light source in the EUV region for EUV Lithography has become an immediate necessity for the next generation high volume manufacturing (HVM) of computer chips.

1.3.1 EUV Lithography

Lithographers utilize the Rayleigh criteria for resolution and imaging to print smaller features. The system dependent equations that describe the resolution and depth of focus for imaging a mask on to a wafer is given to be

$$RES = k_1 \frac{\lambda}{NA} \tag{1.30}$$

and the depth of focus is

$$DOF = k_2 \frac{\lambda}{(NA)^2} \tag{1.31}$$

where k_1 and k_2 are application dependant constants. If $k_1 = k_2 = 0.61$, then the Rayleigh criterion for diffraction limited imaging is satisfied. Best resolution is achieved using short

wavelength, large NA, or small k_1. Lithographers have reached the limits on increasing NA and decreasing k_1, and are now pursuing the short wavelengths for illumination. Thus, EUVL has become the next logical step to printing high-performance and economical computer chips. EUVL will utilize reflective optics, Mo-Si MLM, in near vacuum. Critical requirements for an EUV light source for lithography are listed in Table 1.1 [21].

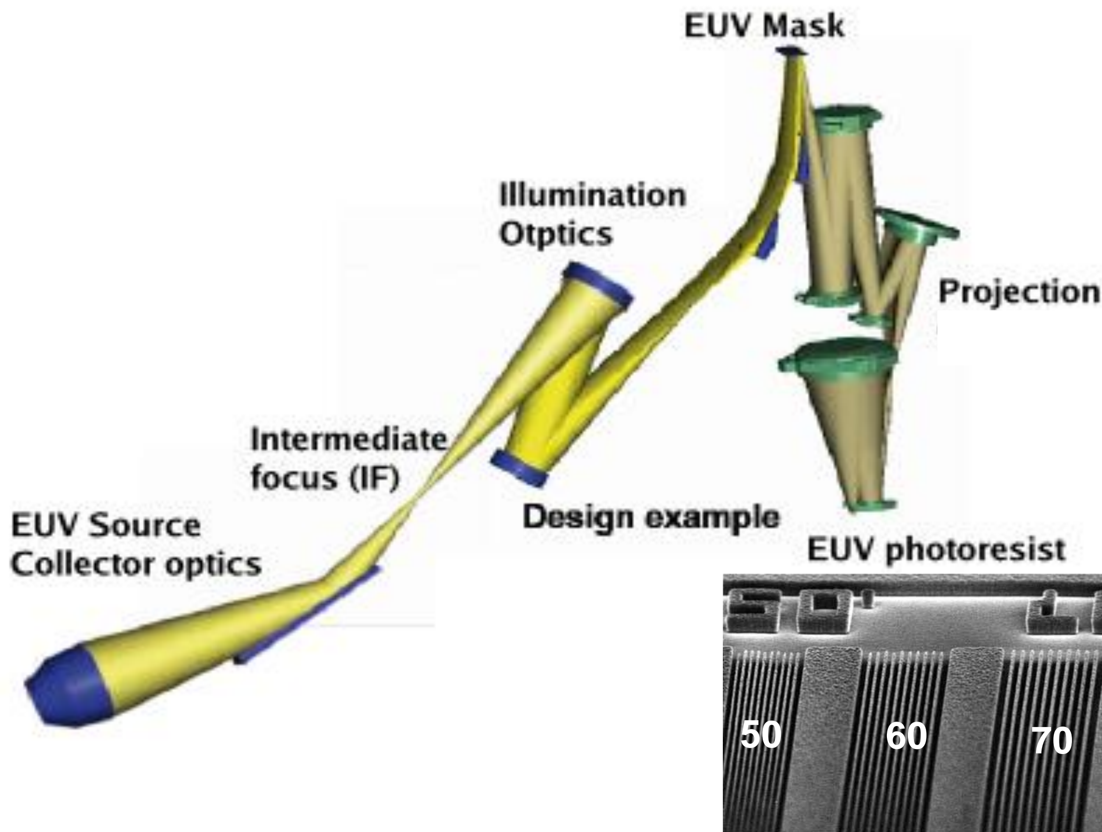

Figure 1.7: General schematic of EUVL stepper system design using reflective optics [22], and example of structures printed with EUV radiation taken from ref. [2]

The ideal source is required to have stable, high power output in the wavelength band of the mirror, long operational lifetime (>30,000 hrs), and spectral purity. Lifetime is related to the length of time the ML coating can withstand continuous, high repetition rate source

Table 1.1: Joint Requirements for EUV Sources, Barcelona, 2006

Source Characteristics	Requirements
Wavelength	13.5 nm
EUV power at Intermediate Focus (in-band)	115 W - 180 W
Repetition Rate	7 kHz - 10 kHz (no upper limit)
Source Cleanliness (light-on hours)	$>$ 30,000 h
Spectral Purity (design dependent):	
130 - 400 nm	$<$ 3% - 7% of the integrated intensity
$>$ 400 nm	To be determined

operation, without major reflectivity degradation requiring cleaning or replacement. Mo-Si ML structures are highly reflective in the VUV/Vis/IR region, thus source spectral purity is a requirement. Mo-Si MLM average reflectivity for 130 nm-400 nm is near 60%, where these wavelengths reaching the wafer behave as a flare affecting the critical dimension control [23]. More than 90% reflectivity is expected for IR radiation where it will be transmitted through the optical system with nominal attenuation, causing thermal expansion of the wafer, therefore, reducing overlay accuracy. Wavelengths absorbed by the mirror surface, can result in mirror heating leading to accelerated degradation of the ML structures.

EUVL is expected for high volume production by 2011 [23]. However, there are many technical challenges that remain. An EUV source that meets all of the requirements put forth by the stepper manufacturers is key to the success of EUVL.

1.4 Overview of thesis

The paper investigates materials for sources with high EUV yield from laser generated plasmas from targets in the low and high-Z regions of the periodic table, as well as multi-component targets. There are a broad range of MLMs available with bandwidths tuned to

a variety wavelengths. Studies completed in this thesis focus on developing sources for the Mo-Si MLM bandwidth centered at 13.5 nm. Mo-Si multilayers have been demonstrated to be the most efficient in reflectivity in the 11 nm - 20 nm region and they are currently most utilized periodic structures in EUV region with many applications. Once a high average power EUV source is realized, it can be extended to other optics such as the 13 nm zone plates used for microscopy.

Laser architectures with power outputs capable of generating plasmas for short-wavelength radiation emission is investigated for multiple sources configurations. The dynamics of laser-plasma interactions are measured in detail for a number of laboratory parameters for a variety of targets using spectroscopic techniques. Measured EUV power levels and spectral results are presented for each of the laser and target configuration under consideration. Interpretation of the experimental data is completed with comparisons to theoretical calculations on atomic emission lines and structure, and simulations of laser-plasma interactions for a given set of laboratory conditions.

1.5 References

[1] James A. R. Samson. *Techniques of Vacuum Ultraviolet Spectrosocpy.* John Wiley and Sons, Inc., New York, first edition, 1967.

[2] David Attwood. *Soft X-rays and Extreme Ultraviolet Radiation: Principles and Applications.* Cambridge University Press, Berkeley, 1999.

[3] Carolyn A. Larabell and Mark A. Le Gros. X-ray Tomography Generates 3-D Recon-

structions of the Yeast, Saccharomyces cerevisiae, at 60-nm Resolution. *Mol. Biol. Cell*, 15(3):957–962, 2004.

[4] Max Born and Emil Wolf. *Principles of Optics: Electromagnetic Theory of Propagation, Interference and Diffraction of Light.* Pergamon Press, New York, sixth edition, 1980.

[5] Mark Fox. *Optical Properties of Solids.* Oxford University Press, New York, first edition, 2001.

[6] E. M. Gullikson. Optical properties of materials. In *Vacuum Ultraviolet Spectroscopy I*, chapter 13, pages 257–270. Academic Press, New York, 1998.

[7] B. L. Henke, E. M. Gullikson, and J. C. Davis. X-ray interactions: photoabsorption, scattering, transmission, and reflection at e=50-30000 ev, z = 1-92. *Atomic Data and Nuclear Data Tables*, 54(2):181–342, July 1993.

[8] James A. Samson and David L. Ederer. *Vacuum Ultraviolet Spectroscopy I.* Academic Press, San Diego, 1972.

[9] John David Jackson. *Classical Electrodynamics.* John Wiley & Sons, Inc., New York, third edition, 1999.

[10] Eugene Hecht. *Optics.* Pearson/Addison Wesley, New York, fourth edition, 2002.

[11] Alan G. Michette. *Optical systems for soft x-rays.* Plenum Press, New York, first edition, 1986.

[12] A. V. Vinogradov and B. Ya Zeldovich. X-ray and far-uv multilayer mirrors: Principles and possibilities. *Applied Optics*, 16:89, 1977.

[13] Sasa Bajt, Jennifer B. Alameda, Troy W. Barbee Jr., W. Miles Clift, James A. Folta, Ben Kaufmann, , and Eberhard A. Spiller. Improved reflectance and stability of mo-si multilayers. *Optical Engineering*, 41(8):17971804, 2002.

[14] E Meltchakov, V Vidal, H Faik, M-J Casanove, and B Vidal. Performance of multilayer coatings in relationship to microstructure of metal layers. characterization and optical properties of mo/si multilayers in extreme ultra-violet and x-ray ranges. *Journal of Physics: Condensed Matter*, 18(13):3355–3365, 2006.

[15] Eric Gullikson. Multilayer reflectivity. Technical report, `http://henke.lbl.gov/optical_constants/`, 2007.

[16] A. I. Erko, V. V. Aristov, and B. Vidal. *Diffraction X-ray Optics*. Institute of Physics Publishing, Philadelphia, 1996.

[17] Eberhard Spiller. *Soft X-ray Optics*. SPIE Optical Engineering Press, Washington, first edition, 1994.

[18] D. Hambach and G. Schneider. High aperture diffractive x-ray and extreme ultraviolet optical elements for microscopy and lithography applications. volume 17, pages 3212–3216. AVS, 1999.

[19] Weilun Chao, Bruce D. Harteneck, J. Alexander Liddle, Erik H. Anderson, and David T. Attwood. Soft x-ray microscopy at a spatial resolution better than 15 nm. *Nature*, 435(7046):1210 – 1213, 2005.

[20] Dong-Hyun Kim, Peter Fischer, Weilun Chao, Erik Anderson, Mi-Young Im, Sung-Chul Shin, and Sug-Bong Choe. Magnetic soft x-ray microscopy at 15 nm resolution probing nanoscale local magnetic hysteresis (invited). volume 99, page 08H303. AIP, 2006.

[21] A. Miyake, H. Kanazawa, V. Banine, and K. Suzuki. "joint requirements". "Presentation at EUV Workshop, Proceedings available at www.sematech.org", "October 19. 2006".

[22] Peter Kürz. The euv optics development program at carl zeiss smt ag. Technical report, `http://www.sematech.org/meetings/archives/litho/euvl/20030930/presentations/8A%20P%20Kurz%20EUV%20Symp.pdf`, 2003.

[23] Vivek Bakshi, editor. *EUV Sources for Lithography.* SPIE Press, Washington, 2005.

CHAPTER 2
EUV SOURCE GENERATION

2.1 Introduction

EUV radiation can be generated in a number of ways and the sources can be categorized according to the method of radiation production. Main categories are: (1) accelarated electron sources such as a synchrotron, (2) high-order harmonic generation (non-linear optics), and (3) thermal sources which include EUV and x-ray lasers. Currently free electron lasers (FEL) are also under consideration as a light source for EUVL and other applications [1]. A potential EUV source for lithography as well as other laboratory applications must meet a few basic criteria; enough intensity for minimum exposure, spatial coherence for uniform illumination, sufficient monochromaticity for reducing chromatic aberrations, low debris associated with source generation to preserve the lifetime of the expensive optics, and the overall source scheme must be inexpensive. Light source parameters are typically described in units of brilliance or brightness with units of $photons/sec \times Sr$ into a given bandwidth (BW) or intensity in units of W/cm^2. Temporal and spatial coherence of the emitted radiation are of importance to many applications as well, especially in the case of microscopy. Thus, further classification of sources are made in terms of coherence properties.

This chapter provides a short description of the various source architectures available for researchers today, ending with the source generation scheme investigated for this thesis. Detailed descriptions of the theory and applications of many EUV sources can be found in references [2, 3, 4, 5]. Figure 2.1 [6], gives a schematic comparison of the spectral brightness

of various sources available in the spectral region of interest for this thesis.

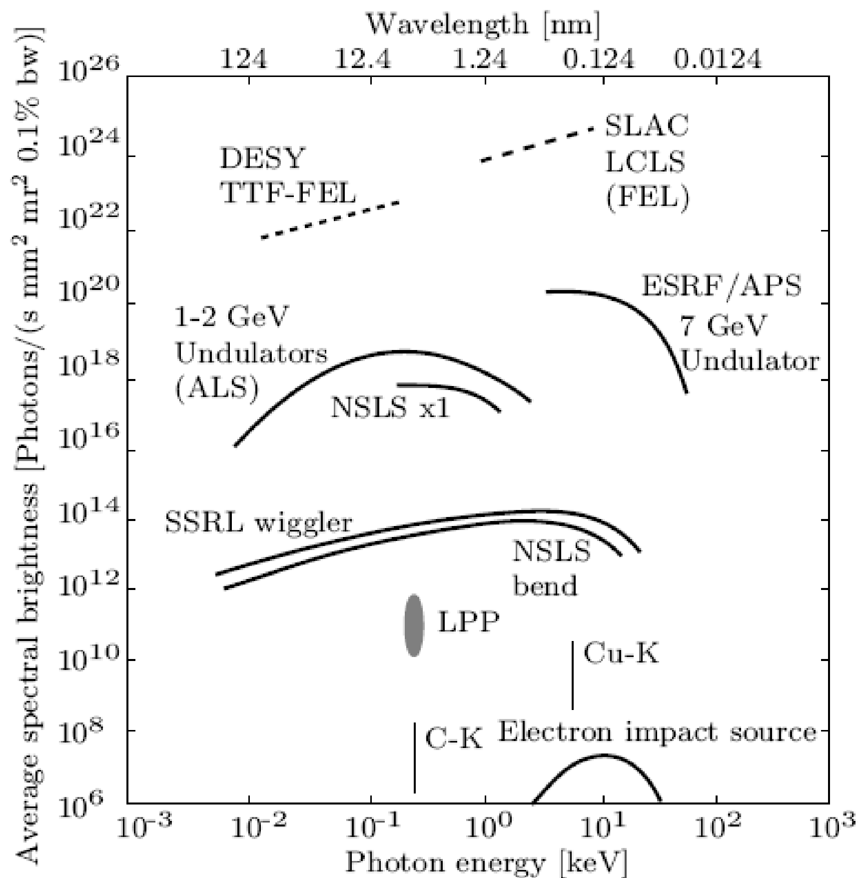

Figure 2.1: Comparison of average spectral brightness of various short wavelength sources.

2.2 Continuous sources

The first hard x-ray source discovered by Wilhelm Conrad Röntgen in 1895 were electron impact sources from high voltage electrical discharges between metal filament and anode in evacuated glass tubes. Both Bremsstrahlung continuum radiation and line emission

characteristic of the anode materials were produced. Although efficient for hard x-rays and forms the basis of medical imaging, these are not of much use in the EUV region. By the nature of electron mean free paths in solid density materials, only a few photons are produced and EUV cannot go through the glass.

Another electron impact source in the EUV/Soft x-ray region is the Penning gas discharge source [7, 8, 9, 10]. The basic principle involves generation of electrons from a self-heated cathode. The electrons are then accelerated in a cycloidal path under the influence of electrical and magnetic fields. 100's of mA of current in a low pressure gas environment is used. Electrons collide with gas molecules and scatter to the anode by means of collisions. Due to collisional avalanche, a high energy distribution of electrons is produced in the discharge region between the two anodes. These electrons excite a variety of lines, lines intrinsic to the discharge gas and more importantly, lines produced by the excitation of highly ionized material sputtered from the cathode faces [8, 9]. This source is simple and compact, free of contamination, but lacks the intensity necessary for many applications. Thus, electron impact sources are generally neglected for EUV and soft x-ray applications.

2.2.1 Synchrotron Radiation Sources

In classical physics it is known that an electrically charged particle emits continuum electromagnetic radiation when accelerated. In a synchrotron, acceleration of electrons at relativistic speeds confined by magnetic fields to a curved trajectory results in the emission of radiation. Detailed theory of generation and applications of the synchrotron radiation can be found in [2, 4]. The synchrotron radiation is a very bright (flux per unit area per solid angle), broadband, polarized, pulsed source of light that covers the entire electromagnetic

spectral region. It is currently the most important source of EUV/soft x-ray radiation in use for fundamental scientific investigations. The older electron storage rings were simply circu-

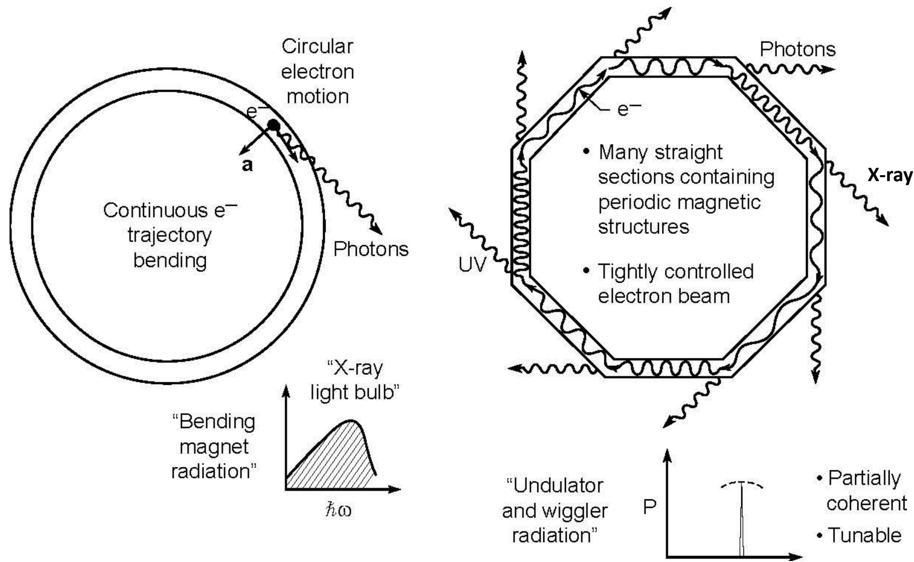

Figure 2.2: Early synchrotron facilities, and modern storage rings optimized for high brightness with inclusion of wigglers, undulaters, and bending magnets for turning. Figure reproduced with permission from [2]

lar rings of ultra high vacuum (10^{-9} Torr) with electrons kept in orbit by bending (dipole) magnets and focusing (quadrupole) magnets used to prevent beam divergence. Modern synchrotron storage rings have a more complex geometry, quasi-polygonal, with three types of magnetic structures used to produce radiation: bending magnets for turning one straight section to the next, with insertion devices called undulators and wigglers utilized at the straight sections for tuning radiation characteristics (fig. 2.2). A brief description of the three types follow.

Bending Magnets

In the bending magnet structure, as the electron traverses a curved path, broadband radiation is emitted tangentially in a narrow radiation cone which is described as a "sweeping searchlight" (Fig. 2.3). For highly relativistic electrons in the laboratory frame of reference, the Lorentz contraction factor $\gamma \equiv 1/(1 - v^2/c^2)^{1/2} \gg 1$, where v is the relative velocity between frames and c is the speed of light. The emission angle θ, is then

$$\theta \simeq \frac{1}{2\gamma} \tag{2.1}$$

The total electron kinetic energy (typically in the order of $10^9\, eV$ in terms of γ and the electron rest energy mc^2, is

$$\gamma = \frac{E_e}{mc^2} = 1957 E_e(GeV) \tag{2.2}$$

The critical photon energy, E_c, with half the radiated power in higher energy and half in lower energy photons, provide the primary characterization parameter for bending magnet radiation

$$E_c = \hbar\omega_c = \frac{3e\hbar B\gamma^2}{2m} = 0.6650 E_e^2(GeV)B(T) \tag{2.3}$$

where B is the bending magnet field. The corresponding critical wavelength is,

$$\lambda_c(nm) = \frac{1.864}{E_e^2(GeV)B(T)} \tag{2.4}$$

Undulators and Wigglers

Third generation electron storage rings use insertion devices called undulators and wigglers (Fig. 2.3). These are periodic magnetic structures inserted at the straight sections

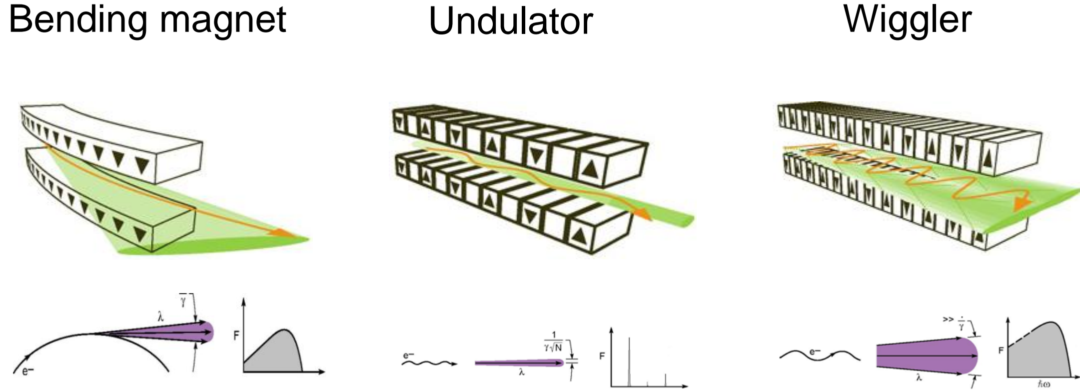

Figure 2.3: Methods of generating radiation from bending magnets, undulators, and wigglers at a synchrotron [2, 11].

of electron storage rings, resulting in sinusoidal electron motion in the horizontal plane. The undulator and wiggler have similar magnetic structures and they are typically a few meters long, but there are significant differences in the emission profile.

The strength of oscillations experienced by a relativistic electron traversing the field of periodic magnetic structures depends on the non-dimensional magnetic deflection parameter K defined to be [2, 4]

$$K \equiv \frac{eB_0\lambda_u}{2\pi mc} = 0.9337B_0(T)\lambda_u(cm) \tag{2.5}$$

where B_0 is magnetic field amplitude, λ_u is the magnet period, and m is the electron rest mass. For the undulator, $K \leq 1$, characterized by weak magnetic fields giving rise to sinusoidal electron motion with emission into a narrow spectral bandwidth. The central radiation cone is defined as

$$\theta = \frac{\sqrt{1+K^2/2}}{\gamma\sqrt{N}} = \frac{1}{\gamma * \sqrt{N}} \tag{2.6}$$

where N is the number periods. This radiation is provides high spectral brightness, partial coherence, tunability, and narrow bandwidth ($\triangle\lambda/\lambda = 1/N$).

Wigglers have large magnetic fields, $K \gg 1$, with large numbers of stronger harmonics extending into higher photon energies. Broadening of the numerous harmonics leads to merging of the emissions into a continuum. The emission angle is much greater than the natural $1/\gamma$ radiation cone. Wiggler radiation is less bright than the undulator radiation but provides higher photon flux for higher photon energies.

$$\theta = \frac{1}{2\gamma} \tag{2.7}$$

For EUVL, it was proposed that an electron beam energy of 700 MeV and magnetic field of 1.0 T provides $4.8mW/mrad/A/2\%BW$ at 13 nm [12]. Unfortunately, synchrotrons are large and too expensive to be economical for EUVL stepper use and for small scale laboratory experiments. Thus, a more modular, less expensive source is desirable in this region.

2.2.2 Free Electron Lasers

The fourth generation synchrotron source for enhanced performance is a free electron laser (FEL). More on the history and current development of FELs can be found in literature [13, 14, 15, 1]. In a free electron laser, a beam of relativistic electrons produced by an electron accelerator passes through a transverse, periodic magnetic field of a very long undulator. The deflection of the electrons in to a sinusoidal path results in Bremsstrahlung emission. The emitted radiation provides the widest frequency range of any laser type, ranging in wavelengths from microwaves, terahertz radiation and infrared, visible, ultraviolet, to soft x-rays. In the laboratory frame, the EM radiation travels along parallel to the electron beam. A FEL is a laser in that the electrons stimulate more EM radiation to form microbunches, moving in phase (coherent) with the field of the light already emitted, so that the fields add coherently, hence amplification. There are several ways to provide the incident optical beam

in the FEL; from an external source (laser), or itself. When an external source is used, the FEL is the amplifier and the source is the master oscillator with the output beam the same as that of the master oscillator.

In the FEL oscillator configuration, the length of the undulator structure is a few meters corresponding to 100 or more periods. The undulator structure is inside the optical resonator mirrors that are separated by approximately twice the undulator length. The mirrors capture the initially released photons to generate resonant gain. By adjusting the beam energy (speed/energy of the electrons) or the magnetic field strength, the wavelength of emission can be tuned rapidly over a wide range. Thus, the output wavelength can have any value. For soft x-rays and EUV amplification in a FEL, it is not possible to use mirrors and seed lasers. Self amplified spontaneous emission (SASE) is another method used where the electron beam forms micro-bunches under the influence of it own synchrotron radiation.

FELs are advantageous for their tunability and the availability of high power accelerators. Disadvantages include the high cost and their large sizes. Also, they have not yet reached the high average power that are necessary for EUV and soft x-ray applications.

2.3 Pulsed Plasma Sources

Much of the universe is in the plasma state, described as the "fourth state of matter that is a quasineutral gas of charged and neutral particles which exhibits a collective behavior" [16]. Electron and ion densities and temperatures are the four characterizing parameters of a plasma. Earliest plasma applications involved gas discharges, in the low density regime [16]. Today's high temperature and density laboratory plasma sources emit continuum and line radiation into a range of wavelengths making the development of a compact, high-power

light source feasible in the short wavelength region.

2.3.1 Discharge Sources

Gas discharge based plasma sources have been known to be emitters in the EUV range for decades. These plasmas are generated by applying a large potential difference across a column of gas, causing electrical breakdown in the gas. Gas pressures of 100's of mTorr to a few Torr are used, and avalanche ionization results from the collisions between a few initial discharge free electrons and the gas atoms. The plasma may initially compress due to magnetic fields generated by the discharge current, but it eventually decays due to hydrodynamic expansions and heat transfer to its surroundings. The duration of the emission is determined by the electron temperature and ion density profile which is usually only a few fraction of the pulse duration of the driving current.

Research interest in investigating discharge produced plasmas (DPP) as a possible high power short wavelength radiation source, especially for EUV-lithography, has increased in the recent years. The design of the discharge sources are relatively simple, and the configurations available today vary in electrode geometry and background gas input schemes. A variety of competing concepts are reported in the literature [4, 3]. Topics relevant for EUVL such as spectral emission characteristics, conversion efficiency (CE), source size, repetitive operation, pulse to pulse stability and lifetimes are also discussed for DPPs in reference [3]. The conversion efficiency (CE) for discharge plasmas is calculated as the ratio of the input electrical power to the EUV radiation output, this efficiency is the major advantage for this source scheme. The source sizes are typically 100's of microns and pulsed operation is generated with high voltage sources. The major disadvantage for these sources are debris,

discussed below.

Some of the concepts investigated for a high power EUV source at 13 nm include the capillary discharge sources [17, 18, 19], the gas puff z-pinch [20, 21], dynamic pinch plasma [22] or the dense plasma focus [23]. Although efficient, these sources suffer from debris resulting from electrode erosion that can damage the collector optics. Damage to the optics will result in decreased source lifetime, which is disadvantageous for applications requiring continuous long term source operation like EUVL.

2.3.2 EUV/soft x-ray Lasers, and Femtosecond High-Harmonic EUV Generation

Unlike FELs, EUV and soft x-ray lasers use discharge produced [24] or laser produced plasmas (LPP) [25] as the active medium by which short wavelength light amplification occur. Lasers are coherent sources that concentrate light into a small beam of narrow line width. The first demonstration of EUV laser was from ionized thin foils of selenium producing population inversion of the $2p^5 3p$ and $2p^5 3s$ levels of the neon like ion. This was achieved in 1985, at the Lawrence Livermore National Laboratory using line-focused beams from a fusion class laser (Novette) [26]. Since then many research groups have demonstrated the feasibility of these lasers [27, 28] and extensive reviews on the theory, development and applications of these lasers can be found in references [2, 25, 24, 5]. While EUV amplifiers have some very specialized applications, their need for large laser systems severely limits their practical utility.

Another approach to generating tabletop, coherent EUV light is to use high harmonic generation (HHG). In the more common harmonic generation processes involving visible or near UV, intense light passing through transparent crystals cause the electrons in the lattice

to move in response to the electric field of the incident beam. With sufficient beam intensity, the motion of the electrons is no longer purely sinusoidal which results in the coherent re-radiation of the electromagnetic waves into the driving laser frequency and at the higher harmonics [5, 29]. In HHG, a short pulsed (sub-picosecond) laser beam with intensities of 10^{13} to 10^{16} W/cm^2 is focused across an atomic jet of rare gas. The laser field is strong enough to remove electrons from their bound states. The ionized electron motion is complex and non-sinusoidal resulting in re-emission into high frequencies. The produced radiation is coherent with minimal divergence, but the energy is distributed among may harmonics and thus far the conversion efficiencies obtained into the EUV range is low. High harmonic generation from ions in a capillary discharge have been demonstrated, as well [30].

2.3.3 Laser Plasmas

A focused laser beam irradiating a target surface creates a hot-dense plasma with temperatures and densities sufficient to produce emission into the EUV and soft x-ray region of the electromagnetic spectrum. Electron temperatures and densities vary with time and distance, as these are rapidly expanding plasmas. Emission characteristics are directly dependent on the plasma temperature and density, and are influenced by laser features, target composition, and geometry. Laser beam intensity, which is a function of focused spot area, beam energy, and pulse duration, is a key factor in obtaining optimum temperatures and densities needed for the required emission. Almost always what is observed is the time and space integrated emission. However, the brightest and shortest wavelength radiation from these plasmas originate from a relatively small region at the peak of the driving laser pulse. Laser plasmas are compact, intense light sources, and are advantageous due to power

scalability, high repetition rates and thus greater dose stability, small source size with large solid angle for collection, and energy stability. Disadvantages of a LLP EUV source include lower electrical conversion efficiency because of the need for a laser and also collateral debris generation where the plasma is found.

Laser produced plasmas (LPP) are attractive because of their small size, they can be extended to higher frequencies, and the laser itself can easily be integrated into the overall design of an imaging system. Many types of target configurations for LPP's are being investigated currently and these include planar slabs [31, 32], cluster targets and cylindrical jets [33], tape targets [34], coated plastic shells, [35] and droplets produced from a variety of materials [36, 37, 38, 39, 40]. Detailed overview of the various architectures and theory behind them can obtained from reference [3].

The plasma spatial dimensions are governed by the laser spot size, typically from 10 to 100's of μm which makes the laser plasma EUV source effectively a point source. The source efficiency or the conversion efficiency (CE) for laser plasma is defined as the ratio of laser input energy to the EUV energy radiated into the 2% bandwidth of the mirror design wavelength and $2\pi Sr$ of the collector optic. As in discharge plasmas, laser plasmas suffer from debris issues from clusters, aerosols, neutrals and ions produced [41]. To control the debris, the mass limited target concept [42] was introduced by the Laser Plasma Laboratory along with other mitigation techniques. 13.5 nm EUV light source generation from laser produced plasmas (LPP) is the focus of the research completed for this thesis.

2.4 Target Materials for EUV Generation

The threshold intensity and the emission characteristics of both discharge and laser plasmas, both line and continuum, are determined by the target material used, plasma parameters, and the temporal development of the plasma. The continuum radiation is similar to black body radiation and is strongly dependent on the temperature and electron density of the plasma. The discrete, or line, emission occurs between bound states of the target atomic species and can only occur if the plasma has reached a stage of ionization high enough that the final states are not occupied and can be filled by the transitioning electrons. Detailed descriptions of the laser-plasma interaction will be given in the following chapter (Chap. 3).

Large EUV illumination intensity from such a small source is required by the EUV community. To achieve increased collectable power levels, conversion efficiency of the input laser energy to the mirror in-band EUV emission needs to be optimized. This must be achieved while keeping the overall costs as well as plasma debris production to a minimum.

A number of elements for use as EUV sources have been investigated, with varying geometry. Nagel et al (Fig.2) investigated cylindrical sources of elements varying in atomic number (Z), and compared broadband x-ray emission as a function of Z [43] (Fig. 2.4). It was observed that there is a maximum in the x-ray conversion efficiency (CE) near Z = 50, this result was later confirmed by others [44]. Progressively, high conversion efficiency of tin (Sn, Z = 50) with spectral data showing strong peak or an intense unresolved transition array in the region of 13 nm in comparison to other materials was reported. Other elements under investigation with discharge and laser produced plasmas for high power EUV source include, Li, Xe, In, and Fe. Pure elements or compounds of them are used in a variety of geometries for the target schemes.

Initially shunned due to the debris problem, with the utilization of the mass-limited

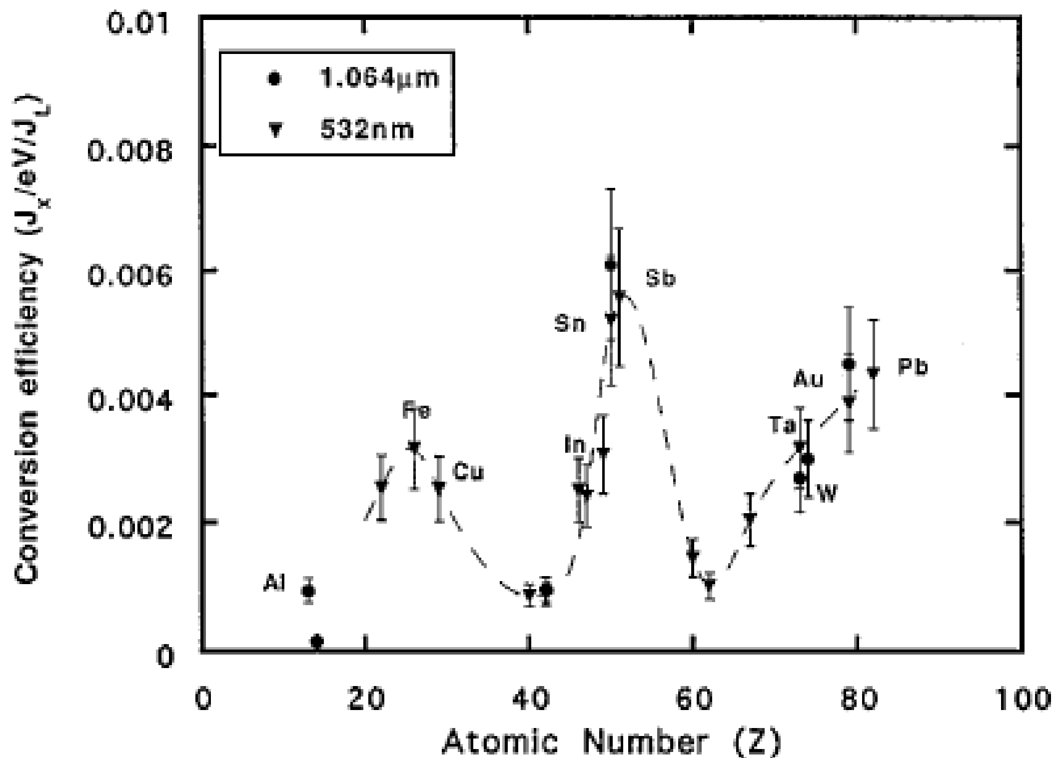

Figure 2.4: EUV emission as function of atomic number

concept, tin based targets have emerged as one of the leading candidates in the race for the high power EUV light source [42]. The Laser Plasma Laboratory began investigating mass limited targets in the early 90's. Christian Keyser obtained CE and spectral measurements for water droplet targets and tin droplets [39], and Chiew-Seng Koay optimized CE of Sn-doped droplet plasmas with 1064 nm, Nd:YAG, solid state laser [40].

For this thesis, extensive measurements of EUV emission from laser plasmas are completed with efforts to model the behavior. Spectroscopic measurement of EUV emissions from planar tin, droplet tin, planar lithium, lithium droplets, and prepulse enhancement of water droplet targets are reported. EUV generation from high power solid-state and fiber

laser pump beams and Sn-doped droplet plasmas are completed to demonstrate the feasibility of a high power source that will meet the requirements of high volume manufacturing for EUVL. Efforts to quantify broadband emission from Sn-doped droplet microplasmas using calibrated spectroscopy is conducted, but this problem proved to be beyond the scope of this thesis and was not completed. Calculations utilizing existing atomic physics code suites are used in the interpretation of experimental spectral data. To determine charge-state populations in the plasma, plasma state parameters are obtained for a given set of experimental conditions through simulations.

2.5 References

[1] E. Di Fabrizio. Fermi project: diffractive optics, microscopy and euv lithography. Technical report, `http://www.frielektronlaser.se/Docs/FERMI/SCDiFabrizio.pdf`, 2004.

[2] David Attwood. *Soft X-rays and Extreme Ultraviolet Radiation: Principles and Applications.* Cambridge University Press, Berkeley, 1999.

[3] Vivek Bakshi, editor. *EUV Sources for Lithography.* SPIE Press, Washington, 2005.

[4] James A. Samson and David L. Ederer. *Vacuum Ultraviolet Spectroscopy I.* Academic Press, San Diego, 1972.

[5] Pierre Jaeglé. *Coherent Sources of XUV Radiation: Soft X-ray Laser and High-Order Harmonic Generation.* Springer, New York, first edition, 2006.

[6] Göran Johansson. *Compact Soft X-Ray Microscopy.* PhD thesis, Royal Institute of Technology, Department of Physics, 2003.

[7] Stuart Bowyer. Continuous emission source covering the 50-300-a band. *Appl. Opt.*, 32(34):6930, 1993.

[8] David S. Finley, Stuart Bowyer, Francesco Paresce, and Roger F. Malina. Continuous discharge penning source with emission lines between 50 a and 300 a. *Appl. Opt.*, 18(5):649, 1979.

[9] J. Cao, F. Li, L. Qian, B. Chen, Y. Ma, and X. Chen. Penning discharge vuv and soft x-ray source. In J. P. Knauer and G. K. Shenoy, editors, *Proc. SPIE Vol. 1345, p. 71-77, Advanced X-Ray/EUV Radiation Sources and Applications, James P. Knauer; Gopal K. Shenoy; Eds.*, volume 1345 of *Presented at the Society of Photo-Optical Instrumentation Engineers (SPIE) Conference*, pages 71–77, January 1991.

[10] Kellogg E. M., Wargelin B. J., Norton T. J., Eng R., and Kolodziejczak J. J. Penning source for calibration of x-ray and euv optics and spectrometers at wavelengths as short as 50 a. In R. B. Hoover and A. B. Walker, editors, *Proc. SPIE Vol. 2515, p. 418-419, X-Ray and Extreme Ultraviolet Optics, Richard B. Hoover; Arthur B. Walker; Eds.*, volume 2515 of *Presented at the Society of Photo-Optical Instrumentation Engineers (SPIE) Conference*, pages 418–419, June 1995.

[11] How is synchrotron light created? Technical report, `http://www.synchrotron.vic.gov.au/content.asp?Document_ID=97`, 2004.

[12] D. C. Ockwell, N. C. E. Crosland, and V. C. Kempson. Synchrotron light as a source for extreme ultraviolet lithography. volume 17, pages 3043–3046. AVS, 1999.

[13] W. B. Colson. Theory of a free electron laser. *Physics Letters A*, 59(3):187–190, 29 November 1976.

[14] D. A. G. Deacon, L. R. Elias, J. M. J. Madey, G. J. Ramian, H. A. Schwettman, and T. I. Smith. First operation of a free-electron laser. *Phys. Rev. Lett.*, 38(16):892–894, Apr 1977.

[15] G. Ramian. Free electron laser: The world wide web virtual library: Free electron laser research and applications. Technical report, `http://sbfel3.ucsb.edu/www/vl_fel.html`, 2006.

[16] Francis F. Chen. *Introduction to Plasma Physics*. Plenum Press, New York, first edition, 1974.

[17] Marc A. Klosner. *Intense capillary dischrge plasma extreme-ultraviolet sources for EUV lithography and other EUV imaging applications*. PhD thesis, University of Central Florida, CREOL & FPCE: The College of Optics and Photonics, 1998.

[18] W. T. Silfvast, M. Klosner, G.M. Shimkaveg, H. Bender, G.D. Kubiak, and N. Fornaciari. High-power plasma discharge source at 13.5 nm and 11.4 nm for EUV lithography. In Y. Vladimirsky, editor, *Proc. SPIE Vol. 3676, p. 272-275, Emerging Lithographic Technologies III, Yuli Vladimirsky; Ed.*, volume 3676 of *Presented at the Society of Photo-Optical Instrumentation Engineers (SPIE) Conference*, pages 272–275, June 1999.

[19] M. A. Klosner, H. A. Bender, W. T. Silfvast, and J. J. Rocca. Intense plasma discharge source at 13.5 nm for extreme-ultraviolet lithography. *Opt. Lett.*, 22(1):34–36, 1997.

[20] Malcolm McGeoch. Radio-frequency-preionized xenon z-pinch source for extreme ultraviolet lithography. *Appl. Opt.*, 37(9):1651–1658, 1998.

[21] Vladimir M Borisov, Aleksander V Eltsov, Aleksander S Ivanov, Yuriy B Kiryukhin, Oleg B Khristoforov, Valentin A Mishchenko, Aleksander V Prokofiev, Aleksander Yu Vinokhodov, and Vladimir A Vodchits. Euv sources using xe and sn discharge plasmas. *Journal of Physics D: Applied Physics*, 37(23):3254–3265, 2004.

[22] Klaus Bergmann, Guido Schriever, Oliver Rosier, Martin Müller, Willi Neff, and Rainer Lebert. Highly repetitive, extreme-ultraviolet radiation source based on a gas-discharge plasma. *Appl. Opt.*, 38(25):5413–5417, 1999.

[23] I V Fomenkov, N Böwering, C L Rettig, S T Melnychuk, I R Oliver, J R Hoffman, O V Khodykin, R M Ness, and W N Partlo. Euv discharge light source based on a dense plasma focus operated with positive and negative polarity. *Journal of Physics D: Applied Physics*, 37(23):3266–3276, 2004.

[24] Howard A. Bender III. *Analysis of the operation and plasma dynamics of extreme-ultraviolet and soft x-ray lasers.* PhD thesis, University of Central Florida, Department of Physics, 1998.

[25] Hiroyuki Daido. Review of soft x-ray laser researches and developments. *Reports on Progress in Physics*, 65(10):1513–1576, 2002.

[26] D. L. Matthews, P. L. Hagelstein, M. D. Rosen, M. J. Eckart, N. M. Ceglio, A. U. Hazi, H. Medecki, B. J. MacGowan, J. E. Trebes, B. L. Whitten, E. M. Campbell, C. W. Hatcher, A. M. Hawryluk, R. L. Kauffman, L. D. Pleasance, G. Rambach, J. H.

Scofield, G. Stone, and T. A. Weaver. Demonstration of a soft x-ray amplifier. *Phys. Rev. Lett.*, 54(2):110–113, Jan 1985.

[27] J. J. Rocca, E. C. Hammarsten, E. Jankowska, J. Filevich, M. C. Marconi, S. Moon, and V. N. Shlyaptsev. Application of extremely compact capillary discharge soft x-ray lasers to dense plasma diagnostics. *Physics of Plasmas*, 10(5):2031–2038, 2003.

[28] B. R. Benware, C. D. Macchietto, C. H. Moreno, and J. J. Rocca. Demonstration of a high average power tabletop soft x-ray laser. *Phys. Rev. Lett.*, 81(26):5804–5807, Dec 1998.

[29] P. M. Paul, E. S. Toma, P. Breger, G. Mullot, F. Auge, Ph. Balcou, H. G. Muller, and P. Agostini. Observation of a Train of Attosecond Pulses from High Harmonic Generation. *Science*, 292(5522):1689–1692, 2001.

[30] Tenio Popmintchev, Michael E. Grisham, David M. Gaudiosi, Brendan A. Reagan, Oren Cohen, Mark A. Berrill, Margaret M. Murnane, Henry C. Kapteyn, and Jorge J. Rocca. Enhanced high harmonic generation in xe, kr and ar using a capillary discharge. In *Conference on Lasers and Electro-Optics/Quantum Electronics and Laser Science Conference and Photonic Applications Systems Technologies*, page JFA3. Optical Society of America, 2007.

[31] Donna J. O'Connell. Characterization of a lithium laser produced plasma at 135 å for extreme ultraviolet projection lithography. Master's thesis, University of Central Florida, CREOL & FPCE: The College of Optics and Photonics, 1994.

[32] Paddy Hayden, Anthony Cummings, Nicola Murphy, Gerry O'Sullivan, Paul Sheridan,

John White, and Padraig Dunne. 13.5 nm extreme ultraviolet emission from tin based laser produced plasma sources. *Journal of Applied Physics*, 99(9), 2006.

[33] Björn A M Hansson and Hans M Hertz. Liquid-jet laser plasma extreme ultraviolet sources: from droplets to filaments. *Journal of Physics D: Applied Physics*, 37(23):3233–3243, 2004.

[34] S. Bollanti, F. Bonfigli, E. Burattini, P. Di Lazzaro, F. Flora, A. Grilli, T. Letardi, N. Lisi, A. Marinai, L. Mezi, D. Murra, and C. Zheng. High-efficiency clean euv plasma source at 1030 nm, driven by a long-pulse-width excimer laser. *Applied Physics B: Lasers and Optics*, 76(3):277–, 2003.

[35] S. Namba, S. Fujioka, H. Nishimura, Y. Yasuda, K. Nagai, N. Miyanaga, Y. Izawa, K. Mima, and K. Takiyama. Spectroscopic study of debris mitigation with minimum-mass sn laser plasma for extreme ultraviolet lithography. *Applied Physics Letters*, 88(17):171503, 2006.

[36] T. Auguste, F. de Gaufridy de Dortan, T. Ceccotti, J. F. Hergott, O. Sublemontier, D. Descamps, and M. Schmidt. Numerical study of nanosecond laser interactions with micro-sized single droplets and sprays of xenon. *Journal of Applied Physics*, 101(4):043302, 2007.

[37] M. Richardson, C.-S. Koay, K. Takenoshita, C. Keyser, and M. Al-Rabban. High conversion efficiency mass-limited sn-based laser plasma source for extreme ultraviolet lithography. *Journal of Vacuum Science and Technology B: Microelectronics and Nanometer Structures*, 22(2):785–790, 2004.

[38] Martin Richardson, David Torres, Chris DePriest, Feng Jin, and Gregory Shimkaveg.

Mass-limited, debris-free laser-plasma euv source. *Optics Communications*, 145:109–112, 1998.

[39] Christian Keyser. *Optical and spectral characterization of the water droplet laser plasma EUV source*. PhD thesis, University of Central Florida, Department of Physics, 1994.

[40] Chiew-Seng Koay. *Radiation studies of the tin-doped microscopic droplet laser plasma light source specific to EUV lithography*. PhD thesis, University of Central Florida, CREOL & FPCE: The College of Optics and Photonics, 2005.

[41] Kazutoshi Takenoshita. *Debris characterization and mitigation of droplet laser plasma sources for EUV lithography*. PhD thesis, University of Central Florida, Department of Electrical Enigineering and Computer Engineering, 2006.

[42] F. Jin and M. Richardson. New laser plasma source for extreme-ultraviolet lithography. *Appl. Opt.*, 34(25):5750, 1995.

[43] R. C. Spitzer, T. J. Orzechowski, D. W. Phillion, R. L. Kauffman, and C. Cerjan. Conversion efficiencies from laser-produced plasmas in the extreme ultraviolet regime. *Journal of Applied Physics*, 79(5):2251–2258, 1996.

[44] H. C. Gerritsen, H. van Brug, F. Bijkerk, and M. J. van der Wiel. Laser-generated plasma as soft x-ray source. *Journal of Applied Physics*, 59(7):2337–2344, 1986.

CHAPTER 3

THE PHYSICS OF LASER-PRODUCED PLASMA SOURCES

3.1 Introduction

Since the invention of laser in the 1960's, theoretical and experimental work in laser-plasma interactions emerged as a major sub-field in plasma physics. Numerous publications exist on laser light absorption processes in plasmas and the resulting emission of radiation. The phenomena of interest for this thesis is the conversion of laser light into EUV radiation. For the experiments completed for this thesis, the relevant absorption process is the inverse bremsstrahlung absorption (IBA), also known as the collisional absorption and resonance absorption. Plasma generation, laser-plasma absorption processes, and the framework of the code and calculations used for this thesis for simulating laser-plasma interactions are discussed in this chapter.

3.2 Absorption of Laser Light in a Plasma

Laser plasmas are produced by focusing a high intensity laser beam onto the surface of a target. Laser photon energy (near 1 eV for 1064 nm) by itself cannot produce ionization, since the ionization potentials of elements are much greater. Direct photo-ionization is not possible, but ionization takes place as a result of the high intensity light beams providing intense electromagnetic field with large photon flux. Poynting's theorem illustrates the

relationship of the irradiance intensity, I (W/cm^2), to the electric field vector where we have $E = \sqrt{2I/\epsilon_0 c}$ (V/cm). A threshold irradiance intensity, typically greater than 10^8 W/cm^2, will provide large enough electric fields and photon flux to facilitate laser induced optical breakdown of materials.

Multi-photon ionization is initiated to form a hot plasma conversion layer or corona on the target surface. This initial ionization occurs at much faster timescales than the total duration of the laser pulse, thus, the later part of the incoming laser pulse couples to the initial plasma corona. Laser light interaction with the plasma corona results in electron avalanche, producing electron density growth. Most theoretical work on laser-plasma interactions start from the plasma corona layer, where there is a charge neutral mix of electrons and ions already in existence. The word "ions" is used as a collective reference for the various species of ions and atoms or molecules existing in the plasma.

Hot dense plasma formed from targets are localized into a small spatial volume with rapid expansion perpendicular to the target surface. The expanding plasma continues to absorb laser energy until the plasma frequency equals the laser frequency, at which point the laser light is reflected. A cartoon schematic of these processes is given in Fig. 3.1. Details of the well established laser plasma theory is provided by references [1, 2, 3, 4, 5, 6, 7, 8] and many others.

Large electron density gradients exist in laser plasmas, ranging from $10^{15}\,/cm^2$ to $10^{23}\,/cm^2$. The electron densities, n_e are related to the ion densities n_i existing in the plasma by $n_e = \Sigma_{Z=0}^{q} Z n_i^Z$, where Z is the number of electrons removed, n_i^Z is the ion density for stage Z and q is the integer representation of the ion stage. Basically, the quasineutrality condition of the plasma requires that $n_e \approx n_i$. The electron temperature of laser plasmas are typically expressed in electron volts (eV) (1 eV=11600 Kelvin) and can range from a few

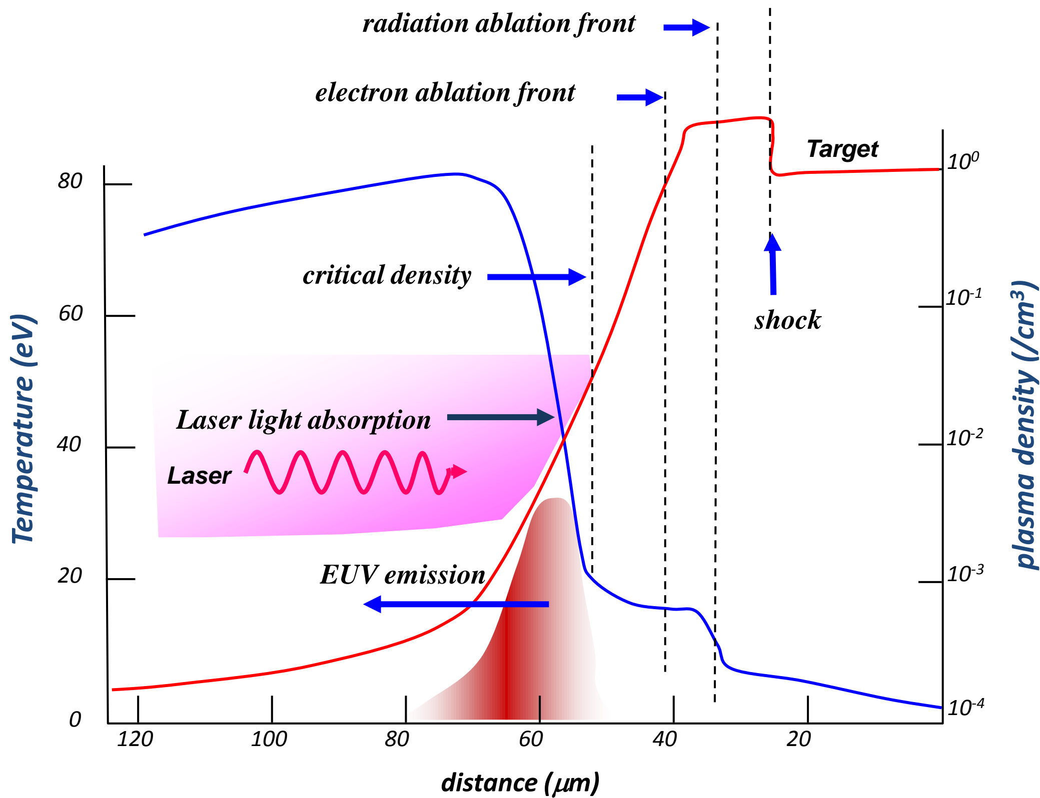

Figure 3.1: Cartoon of laser interaction with target surface leading to EUV emission.

eV's to more than a 100 eV. Laser intensities can vary anywhere from $10^8 - 10^{22}$ W/cm^2, depending on the pulse energies, laser beam spot size, and laser pulse duration (ns - fs). Lifetime of emission from the plasma is closely related to the duration of the laser pulse, since laser plasmas expands and cools rapidly. Several laser-plasma absorption mechanisms, such as resonance absorption, Raman scattering, collisional (IBA) absorption, etc., can take place near the critical density region, depending on the intensity regime of the laser light. The dominant absorption processes in nanosecond plasmas is the IBA or collisional absorption.

3.2.1 Critical Electron Density

The laser beam can propagate through the plasma electron density gradient until it reaches a critical density, which is defined as follows. The wave propagation of the laser light in the presence of free electrons in the plasma follow the dispersion relation

$$\omega_L^2 = \omega_P^2 + k_L^2 c^2 \tag{3.1}$$

where ω_L is the angular frequency, k_L is the wavenumber of the laser light, and c is the speed of light in the vacuum. The plasma frequency, ω_P, is given by

$$\omega_P = \sqrt{4\pi n_e e^2/m} \tag{3.2}$$

where n_e is the plasma electron density, and e and m are the charge and mass of the electron respectively. The incident electromagnetic wave propagates from low density region to high density region until it is completely reflected at a point in the plasma where $\omega_L = \omega_P$. Then the critical density is given to be

$$n_{cr} = \frac{m_e \omega_L^2}{4\pi e^2} \approx \frac{1.1 \times 10^{21}}{\lambda_{\mu m}^2}[cm^{-3}] \tag{3.3}$$

where $\lambda_{\mu m}$ is the laser wavelength in μm. The critical densities for important laser wavelengths are given in table 3.1. EUV/soft x-ray emission tends to occur from the high temperature/high density region near the critical density region, where the highest thermal conduction takes place due to the absorbed laser light. Then, the refractive index of the plasma is given by,

$$n = \sqrt{1 - \frac{w_p^2}{w_L^2}} = \sqrt{1 - \frac{n_e}{n_c}} \tag{3.4}$$

Table 3.1: Critical densities for some common laser wavelengths

Laser	$\lambda(\mu m)$	$n_{cr} cm^{-3}$
CO_2	10.6	10^{19}
Nd:YAG fundamental	1.06	10^{21}
Nd:YAG third harmonic and excimer	.35	9×10^{21}
KrF	.25	1.6×10^{22}

3.2.2 Inverse Bremsstrahlung

Electromagnetic theory states that an accelerating charge produces electromagnetic radiation. Bremsstrahlung (”braking radiation”) is produced when one charged particle is accelerated/decelarated as it is deflected by the strong Coulomb attraction another charged particle. Most used example is the deceleration of an electron over a short distance by the Coulomb interaction with an atomic nuclei or ions, with the electron making the transition to a lower energy free state. Thus, electron-ion Coulomb collisions in a plasma result in Bremsstrahlung emission. Electron-electron collisions do not produce radiation since the accelerations of two electrons are equal and opposite; no net net electron current with no radiation in the dipole approximation [2]. Continuum emission is observed in plasmas with overlapping line emission characteristic of the target material. The Bremsstrahlung process can be described as,

$$e^-(E) + atom \longrightarrow e^-(E') + \hbar\omega + atom$$

where $\hbar\omega = E - E'$ gives the energy of the emitted photon.

Inverse Bremsstrahlung (IBA) is then,

$$e^-(E) + \hbar\omega + ion \longrightarrow e^-(E') + ion$$

where $\hbar\omega = E - E'$ describes the laser photon energy absorbed. In the IBA process, free electrons gain energy by absorbing photons from the laser beam in the presence of ions.

This process is also referred to as collisional absorption of energy with collisions between electrons and ions resulting in increased electron energy and electron temperature. The IBA absorption coefficient given in Eq. 3.5 below, decreases inversely as the third power of photon energy [9, 10, 6, 5].

$$\begin{aligned} k_{IB} &= \frac{16\pi Z^2 n_e n_i e^6 \ln\Lambda(\nu)}{3c\nu^2(2\pi m_e k_B T_e)^{3/2}} \frac{1}{(1-\nu_p^2/\nu^2)^{1/2}} \\ &= \frac{7.8\times 10^{-9} Z n_e^2 \ln\Lambda(\nu)}{\nu^2 (k_B T_e)^{3/2}} \frac{1}{(1-\nu_p/\nu^2)^(1/2)} \end{aligned} \tag{3.5}$$

Z is the ionization state of ions, n_e is electron density, n_i is ion density, e is charge unit, c is speed of light, ν is frequency of laser light ($\omega = 2\pi\nu$), m_e is mass of electron, k is Boltzmann constant, T_e is electron temperature, and ν_p is the plasma frequency ($\omega_p = 2\pi\nu_p$).

The parameter Λ can be considered as the ratio of the impact parameters (p_{max}/p_{min}), where p_{max} is the Debye length (screening distance) beyond which the individual charges are effectively screened in the presence of other mobile charges, and p_{min} is the classical distance of closest approach. The Debye screening distance is an important parameter that separates short-range interactions from long-range interactions in a plasma, and is defined as

$$\lambda_D = \left(\frac{\epsilon_0 k_B T_e}{e^2 n_e}\right)^{(1/2)} \tag{3.6}$$

and the number of electrons in the Debye sphere is given to be,

$$N_D = \frac{4\pi}{3}\lambda_D^3 n_e = 1.7\times 10^3 \frac{(k_b T_e)^{(3/2)}}{n_e^{(1/2)}} \tag{3.7}$$

$\ln\Lambda$ is called the Coulomb Logarithm [4] and this is defined to be,

$$\ln\Lambda = \ln\frac{v_T}{\omega_p p_{min}} \tag{3.8}$$

where v_T is the thermal velocity of the electrons and $p_{min} \cong \hbar/(m_e k_B T_e)^{1/2}$ is the minimum impact parameter for the electron collisions. For $T_i\, m_e/m_i < 10Z^2\,(eV) < T_e$ [6],

$$\ln\Lambda = 24 - \ln\frac{n_e^{1/2}}{T_e(eV)} \tag{3.9}$$

which is a slowly varying function of electron temperature and density. For the plasma regime considered in this chapter, Coulomb Logarithm varies from 5-15. For most calculation purposes a normalized constant of 5 is used for $\ln \Lambda$ [5]. IBA is strongest for low temperature, high density, high Z material plasmas and it is the main absorption mechanism in a plasma where laser irradiances are in the range of 10^{10} to 10^{12} W/cm^2 and the interaction scalelength of the laser pulse with plasma is much longer than the laser wavelength.

In a uniform plasma, the fraction of the absorbed laser energy after light propagation over a distance L is give as

$$\alpha_{abs} = 1 - \exp[-k_{ib}L] \tag{3.10}$$

L is the plasma scale length. The scale length is related to the plasma expansion velocity and laser pulse duration to be

$$L = \tau C_s \tag{3.11}$$

where C_s is the ion sound speed [4],

$$C_s = \sqrt{\frac{(\gamma k T_i + Z\gamma k T_e)}{M_i}} \simeq \sqrt{\frac{Z\gamma k T_e}{M_i}} \tag{3.12}$$

where Z is the ion charge state, M_i is the ion mass, and T_e and T_i are the electron and ion temperatures, respectively. The ion temperature term in the sound speed is often neglected since energy is delivered to the electrons and only indirectly transferred to the ions through collisions, with $T_e \gg T_i$. γ is taken to be equal to unity is most analysis and it is the adiabatic coefficient for ions and electrons that depends on the nature of the wave [7].

Determining if a laser-plasma interaction regime is dominated by IBA absorption is conducted by defining a specific intensity at which IBA is significantly reduced [11]. This characteristic intensity is defined as

$$I^* = \frac{10^{12} Z L_\mu f}{\lambda^4(\mu m)} \tag{3.13}$$

assuming that the plasma is under-dense and isothermal, where L_μ is the plasma scale length (μm), Z is the ion charge state, f is the flux limit, and λ is the laser wavelength. For $I \ll I^*$, IBA is nearly 100% and the heated plasma remains collisional. For $I \gg I^*$, the fraction of the incident energy absorbed is given by $\alpha_{abs} = \sqrt{I^*/I}$, and the plasma is less collisional. For $I = I^*$, $\alpha_{abs} \simeq 74\%$. Various parametric instabilities such as stimulated Brillouin scattering (SBS), stimulated Raman scattering (SRS), two plasmon decay (TPD), etc. can occur in plasmas at high intensity conditions ($> 10^{15}$ W/cm^2) diminishing IBA absorption.

3.2.3 Resonance absorption

In addition to the IBA process, resonant absorption can occur at the critical density for an obliquely incident laser beam having a component of the electric field polarized parallel to the density gradient [4]. This process is strongly linear, resulting in strong local energy deposition causing hot (non-thermal, collision-less) electron generation. The hot electrons can escape from the plasma once they become out of phase with the resonant oscillation due to collisions with ions. The escaping hot electrons will then drag nearby ions by Coulomb attraction with the result that these ions acquire high kinetic energies. This latter process is not likely to occur in the laser intensity region of this study.

3.3 Hydrodynamic Simulations of Laser Plasmas in Lagrangian Coordinates

High temperature/density plasmas are characterized by steep density profiles, rapid thermal expansion, and a number of non-linear terms making a mathematical description of

plasma evolution quite difficult to complete analytically. One numerical solution to approximate the plasma expansion, treats the plasma as two fluids of electrons and ions. The initial plasma is grouped into zones or cells of specified mass with the appropriate parameters, with the evolution computed as energy is absorbed, leading to higher temperature and pressure causing expansion. Electron and ion density, temperature, expansion velocity, pressure, etc, are calculated for each cell, as a function of time and space. The fluid-like Lagrangian code used for the laser-plasma simulation studies conducted for this thesis is a version of the MEDUSA code [12] called MED103 [13], developed at the Rutherford Appleton Laboratory.

The one-dimensional Lagrangian hydrodynamic code, MEDUSA, was initially designed for inertially confined fusion (ICF) studies of implosion and thermo- nuclear burn with controlled time steps. The assumption that the target is uniformly irradiated giving isotropic emission reduces the problem to one-dimension. Then, the thermodynamic and hydrodynamic behavior of plasmas generated with high intensity laser beams on a fusion fuel pellet are obtained by treating electrons and ions as two components in a fluid. The "ions" in this case include various species of ions, atoms or molecules, collectively. The plasma is described by 4 main dependent variables ρ, u, T_i, T_e, which are density, velocity and ion and electron temperatures, respectively. All are functions of time, t, and single space variable, r, for slab (planar), cylindrical or spherical geometry as required. Other parameters that can be specified are the chemical composition of the plasma in terms of the fractions of the various ionic species that are present, with the composition varying in space and time due to the thermonuclear reactions that occur. The Navier-Stokes equations are supplemented by separate heat conduction equations for the ion and electron temperatures and a variety of additional effects are included. A Lagrangian difference mesh is employed with the integration scheme explicitly implemented for hydrodynamics, and implicit for the

heat conduction equations using the Crank-Nicholson scheme and the Gauss elimination method. Several iterations are performed at each time-step in order to take into account the non-linear dependence of the physical coefficients on the density and temperatures and to ensure convergence [12].

The physical model implemented in the code outlined here [12] assumes a charge neutral mix of the electron subsystem with an electron density, n_e, and "ion" subsystem with an ion density, n_i. Both are related by

$$n_e = Zn_i \quad (m^{-3}) \tag{3.14}$$

where Z is the average ion charge state, and the physical mass density is specified to be,

$$\rho = n_i M m_H = \frac{1}{V} \qquad (kg/m^3) \tag{3.15}$$

where m_H is the proton mass, M is the average ion mass number, and V is the specific volume. For laser plasmas, the ions are assumed to behave as a perfect gas and the electrons are described by an ideal gas equation of state (EOS) or by a Thomas-Fermi EOS. The charge neutrality requirement specifies the same velocity for both the electron and ion fluids. Then the motion of the plasma is governed by the Navier-Stokes equation

$$\rho \frac{du}{dt} = -\nabla p \tag{3.16}$$

where u is the velocity of the plasma which defines motion of the Lagrangian coordinates, $dr/dt = u(r,t)$, and the hydrodynamics pressure, p, is defined as $p = p_i + p_e \quad (N/m^2)$.

The internal energies per unit mass, U with independent equations of state for the two subsystems, is denoted by

$$U = \frac{pV}{\gamma - 1} \quad (J/Kg) \tag{3.17}$$

$$U = U(\rho, T), \qquad p = P(\rho, T) \tag{3.18}$$

Then, the energy equation that partitions the absorbed laser energy into thermos=dynamic and kinetic states is given by

$$C_v \frac{dT}{dt} + B_T \frac{d\rho}{dt} + p\frac{dV}{dt} = S \qquad (W/Kg) \tag{3.19}$$

where C_v is the specific heat per unit volume and B_T is the variation of the internal energy within the subsystem due to particle interaction. Both quantities are defined to be,

$$C_v = \left(\frac{dU}{dT}\right)_\rho, \qquad B_T = \left(\frac{dU}{d\rho}\right)_T \tag{3.20}$$

S is the rate of input energy per unit mass. The terms, S_i and S_e for electrons and ions specified to be,

$$S_i = H_i - K + Y_i + Q \qquad (W/Kg) \tag{3.21}$$

$$S_e = H_e - K + Y_e + J + X \qquad (W/Kg) \tag{3.22}$$

where the energy exchange rates result from, thermal conduction (H), electro-ion collisions (K), viscous shock heating (Q), thermonuclear energy release (Y), and the Bremsstrahlung emission (J) and absorption (X) of laser light.

The heat conduction term is given by

$$H = \frac{1}{\rho}\nabla \cdot \kappa \nabla T \tag{3.23}$$

where κ is the thermal conductivity. For electrons and ions the expressions for κ [12] are

$$\kappa_i = 4.3 \times 10^{-12} \frac{T_i^{5/2}}{\log \Lambda \overline{\overline{M^{1/2} Z^2}}} \frac{1}{\overline{\overline{Z^2}}} \quad (W/mK) \tag{3.24}$$

$$\kappa_e = 1.83 \times 10^{-10} \frac{T_e^{5/2Z}}{\log \Lambda} \frac{1}{\overline{\overline{Z^2}}} \quad (W/mK) \tag{3.25}$$

where $\log \Lambda$ is the Coulomb Logarithm, with Λ in this case is given by

$$\Lambda = 1.24 \times 10^6 \frac{T_e^{3/2}}{n_e^{1/2} Z} \tag{3.26}$$

Absorption of laser light is assumed to occur via inverse Bremsstrahlung at densities below critical density and it is modeled using classical coefficients described in the previously in 3.2.2. The electron heat flux is proportional to the electron temperature gradient, $F_e = K_e \nabla T_e$, where K_e is the Spitzer-Härm conductivity, which is only valid if the electron temperature gradient is not too large.

Laser plasmas are characterized by steep temperature and density gradients and are not properly described by the Spitzer-Härm conductivity [8]. A limit called "free streaming limit" was imposed on the electron thermal flux in order to circumvent this problem and to approximate the appropriate physical result, which is

$$\frac{1}{F_{(e,limited)}} = \frac{1}{F_e} + \frac{1}{(F_e)_{max}}, \qquad (F_e)_{max} = f v_e n_e k_B T_e \tag{3.27}$$

where f is the flux limiter parameter with $f < 1$, which is usually adjusted to match experimental results [8].

In modeling nanosecond laser plasma experiments, the target parameters can be specified with the atomic number, atomic mass, mass density, thickness, and boundary conditions. For the laser pulse, number of pulses for multiple pulse irradiation, temporal shapes, pulse durations, wavelength, intensity, etc can be specified in the calculations. Physical processes such as resonance absorption, hot electron generation, and ponderomotive force effects can be accounted for and controlled through logical switches. The true or false logical switches

included in the code can be used to select the physical processes that should be included in each calculation. This makes it possible to simulate a wide range of experimental conditions.

With the recent modifications added to the code by the developers, better control of the initialization conditions for the beam/target is obtained. The physics is improved by adding a high-field correction to the inverse bremsstrahlung with a non-local heat condition subroutine [14], and x-ray laser gain calculations for Ne-like, H-like, Li-like, and Na-like recombination schemes are added [15]. A non-LTE time-dependent average atom model is added with the energies involved in the excitation and ionization coupled to the free electron energy balance equation [15]. Other modifications in the physics and code implementation is completed by this user in order to generate experiment specific results. Thus, plasma expansion dynamics are modeled using MED103 for each experiment completed in this paper.

3.4 References

[1] Francis F. Chen. *Introduction to Plasma Physics*. Plenum Press, New York, first edition, 1974.

[2] Robert J. Goldston and Paul H. Rutherford. *Introduction to Plasma Physics*. Institute of Physics Publishing, Philadelphia, first edition, 1995.

[3] William L. Kruer. *The Physics of Laser Plasma Interactions*. Westview Press, Colorado, 2003.

[4] L. Spitzer. *Physics of Fully Ionized Gases*. Interscience, New York, second edition, 1962.

[5] I. C. E. Turcu and J. B. Dance. *X-rays from Laser Plasmas: Generation and Applications*. Wiley, New York, first edition, 1999.

[6] Danilo Giulietti and Leonida A. Gizzi. X-ray emission from laser produced plasmas. *La Rivista del Nuovo Cimento*, 21(10):1–93, 1998.

[7] David Attwood. *Soft X-rays and Extreme Ultraviolet Radiation: Principles and Applications*. Cambridge University Press, Berkeley, 1999.

[8] Christian Keyser. *Optical and spectral characterization of the water droplet laser plasma EUV source*. PhD thesis, University of Central Florida, Department of Physics, 1994.

[9] John M. Dawson. On the production of plasma by giant pulse lasers. *Physics of Fluids*, 7(7):981–987, 1964.

[10] Tudor Wyatt Johnston and John M. Dawson. Correct values for high-frequency power absorption by inverse bremsstrahlung in plasmas. *Physics of Fluids*, 16(5):722–722, 1973.

[11] H. A. Baldis, E. M. Campbell, and W. L. Kruer. Laser-plasma interactions. In *Physics of Laser Plasma*, chapter 9, pages 361–435. North-Holland, New York, 1991.

[12] J. P. Christiansen, D. E. T. F. Ashby, , and K. V. Roberts. Medusa - a one-dimensional laser fusion code. *Comput. Phys. Commun.*, 7:271, 1974.

[13] A. Djaoui. *A User Guide for the Laser-Plasma Simulation Code: MED103*. The Central Laboratory of the Research Councils, Rutheford Appleton Laboratory, Oxfordshire, 1996. Technical Report RAL-TR-96-099.

[14] A. Djaoui and A. A. Offenberger. Heating of underdense plasmas by intense short-pulse lasers. *Phys. Rev. E*, 50(6):4961–4968, Dec 1994.

[15] A. Djaoui and S. J. Rose. Calculation of the time-dependent excitation and ionization in a laser-produced plasma. *Journal of Physics B: Atomic, Molecular and Optical Physics*, 25(11):2745–2762, 1992.

CHAPTER 4
PLASMA SPECTROSCOPY

4.1 Introduction

Spectroscopy began over three hundred years ago with Newton observing dispersion of visible light through a glass prism. Since then, throughout the history of spectroscopy, plasmas have served as a source of radiation for spectrochemical analysis and atomic structure determination, contributing to the establishment of quantum mechanics. Plasma spectroscopy, also known as atomic physics in hot plasmas, is the study of electromagnetic radiation emitted and the properties of the ionized medium of electrons and ions generating emission. In other words, plasma spectroscopy relates the state of the plasma to the spectral characteristics of the emitted radiation.

A plasma, astrophysical or generated in the laboratory, emits line and continuum radiation of varying intensities which are distributed over a range of wavelengths. Emission is influenced by the average charge-state distribution in the plasma, which is governed by numerous atomic processes. This chapter provides a basic framework of several concepts involved in plasma spectroscopy starting with atomic structure and a brief outline of terminology and notation. Various equilibrium conditions and atomic processes involved in the emission of radiation from plasmas, and a number of models that are in use for determining population distribution and kinetics in plasmas are described. There are many excellent textbooks that describe plasma spectroscopy in detail [1, 2, 3, 4, 5, 6, 7]. The outline provided here primarily utilizes the notation used by David Salzmann [5] for the atomic processes

in hot plasmas, and the text by R. D. Cowan [8] for the atomic structure theory. Studies conducted for this thesis use emission spectroscopy as the primary plasma diagnostic for determining the plasma electron temperature and density of states.

4.2 Atomic Structure and Spectra

The description of the atomic world is given by quantum mechanics. Coulomb interaction between electrons and the nucleus, and the interaction between electrons and other electrons determine the electronic structure of an atom. The Bohr frequency condition states that a system absorbs or emits light if the energy of that light equals the energy difference between the two states involved in the spectroscopic transition. Meeting this condition might not guarantee emission, thus additional criteria are given for determining whether an absorption or emission occurs. These are called the selection rules. In the electric dipole approximation, if a transition is favored by a selection rule, then it is an *allowed* transition. If a transition is not favored by the electric dipole approximation restricted selection rules, then it is labeled *forbidden*. Forbidden transitions are allowed if no approximations are made, or if the magnetic dipole or electric quadrupole, octupole, ... radiations are considered. Forbidden transitions occur with reduced probability and are much weaker than the allowed transitions. Following section outlines selection rules for one-electron atom and multi-electron atoms.

4.2.1 Selection Rules

Hydrogen atom wave functions are described by four quantum numbers and they are the principal quantum number n, the angular momentum quantum number $l\,(= 0,\ 1,\ 2,\ \ldots,\ n-1)$, the z-component of the angular momentum quantum number $m_l\,(= 0,\ \pm 1,\ \pm 2,\ \ldots,\ \pm l)$, and the z-component of the spin angular momentum number m_s. The spin angular momentum quantum number s for all electrons is 1/2. When there is state change in Hydrogen atom leading to absorption or emission of photons, there is a change in one or more quantum numbers giving a different wavefunction. For the allowed transitions in a one electron atom, the selection rules are

$$\begin{aligned}
&\Delta n = 0, 1, 2, 3, \ldots \texttt{can be any integer}\\
&\Delta l = \pm 1\\
&\Delta m_l = 0, \pm 1\\
&\Delta m_s = 0
\end{aligned}$$

The selection rules for multi-electron atoms are very similar to the single-electron hydrogen atom. For atoms with $Z < 20$, the electrons are treated as if their orbital angular momenta couple to generate an overall orbital angular momentum with values labeled L, and similarly for the coupling of spin angular momenta producing an overall spin angular momenta with values of S. Then, the total orbital angular momentum can couple to the total spin angular momentum to give the total angular momentum number J which has a z-component represented by M_J. Then the selection rules are modified to include,

$$\begin{aligned}
&\Delta n = 0, 1, 2, 3, \ldots \texttt{can be any integer}\\
&\Delta L = 0, \pm 1; \quad L = 0 \not\leftrightarrow L = 0\\
&\Delta l = \pm 1\\
&\Delta J = 0, \pm 1; \quad J = 0 \not\leftrightarrow J = 0\\
&\Delta S = 0\\
&\mathbf{J} = \mathbf{L} + \mathbf{S}
\end{aligned}$$

Transitions from $L = 0$ to $L = 0$, and from $J = 0$ to $J = 0$ are not allowed. This coupling scheme is called the **LS** coupling scheme or the Russell-Sanders coupling scheme. The

electronic energy levels of atom are called terms and they are labeled by the term symbol, $^{2S+1}\mathcal{L}_J$.

For larger atoms, a better approximation of the electronic behavior is obtained by assuming that the orbital angular momentum and the spin angular momentum of the individual electrons couple to make a total electronic angular momentum j. This coupling scheme is commonly referred to as **jj**-coupling. Nevertheless, LS coupling is still useful and is commonly used for large atoms.

4.2.2 Isoelectronic Sequences

Spectra of ions of different elements having the same number of electrons tend to be very similar in general structure. This is especially true for highly ionized atoms. A sequence of ions having fixed N, or the corresponding sequence of spectra is called an isoelectronic sequence, usually denoted by the first neutral atom member. Generally, the sequence starts with any element in the periodic table followed by other elements in the order of the atomic number. For example, a Calcium-like isoelectronic sequence contain *Ca I*, *Sc II*, *Ti III*, *V IV*, *Cr V*, etc. Isoelectronic sequences are useful in predicting unknown spectra of ions belonging to a sequence in which the spectra of other atoms are known.

4.2.3 Transition Probabilities

For this thesis, the transition probabilities are calculated using a code suite developed by the R. D. Cowan, thus this section outlines the theoretical development described in reference [8]. For an isolated and field free atom in a state with total angular momentum,

J_i, there are [8]

$$g_i = 2J_i + 1 \tag{4.1}$$

degenerate quantum states of energy E_i corresponding to $2J_i + 1$ possible values of the magnetic quantum number M_i, and

$$A_{ji} = \sum_{M_i} a_{ji} \tag{4.2}$$

where A_{ji} is the Einstein A-coefficient of spontaneous transition probability per unit time of an electron in a specific excited state j making a transition to any of the g_i states of the lower energy level i. The weighted transition probability is then

$$g_j A_{ji} = g_j \sum_{M_i} a_{ji} = \sum_{M_j} \sum_{M_i} a_{ji} \tag{4.3}$$

The weighted transition probability is more symmetric in the upper and lower energy levels than the Einstein transition probability. Assuming isotropic excitation and same number of atoms in each of the states belonging to level j, the intensity of the spectrum line or the energy radiated per unit time is calculated to be

$$I(t) = hc\sigma_{ji} g_i A_{ji} N_j(t) \tag{4.4}$$

where $N_j(t)$ is the number of atoms in state j at time t. σ_{ji} is the spectrum line or wave number where,

$$\sigma_{ji} = \frac{1}{\lambda_{ji}} = \frac{E_j - E_i}{hc} \tag{4.5}$$

The total rate of change N_j due to all possible spontaneous transitions is

$$\frac{dN_j}{dt} = -N_j(t) \sum_i A_{ji}, \qquad N_j(t) = N_0 \exp[-t/\tau_j] \tag{4.6}$$

For the transitions induced by the presence of isotropic and unpolarized radiation field, the Einstein coefficients for absorption B_{ij} and simulated emission, B_{ji} are related to the spontaneous transition probability, A_{ji}, by

$$g_j A_{ji} = 8\pi hc\sigma_{ji}^3 g_j B_{ji}, \qquad g_j B_{ji} = g_i B_{ij} \tag{4.7}$$

From, Eq.4.7 it can be understood that g_j is always the statistical weight of the initial level, so the subscripts are dropped in further references to the quantity gA. Obtaining an expression for gA involves accounting for the contributions from the interaction between the electromagnetic field and each electric and magnetic multipole moment of the atom. From the quantum mechanical electric dipole radiation considerations dealing with radiative transitions between two states Ψ and Ψ', the average displacement during the time of radiation is given by,

$$\langle\Psi|\, r\,|\Psi'\rangle = \langle\Psi_0|\, r\,|\Psi_0'\rangle \exp[i(E - E')t/\hbar] \tag{4.8}$$

The spontaneous-emission transition probability a obtained per unit time from an excited state $\gamma' J' M'$ to a lower energy state γJM is [8]

$$a = \frac{64\pi^4 e^2 a_0^2 \sigma^3}{3h} \sum_q | \underbrace{\langle\gamma JM|\, \mathbb{P}_q^{(1)}\, |\gamma' J' M'\rangle}_{\texttt{Dipole matrix element}} |^2 \tag{4.9}$$

where

$$\mathbb{P}_q^{(1)} = \sum_{i=1}^{N} r_q^{(1)}(i) = \sum_{i=1}^{N} r_i C_q^{(1)}(i) \tag{4.10}$$

is the qth component of the classical dipole moment of the atom measured in units of $-ea_0$. Alternate forms of dipole matrix elements are used by various texts, relating to the classical momentum and force. Electric dipole transition can only occur when the matrix element (4.9) is non-zero. The dipole operator has odd parity, and transitions occur between states

with opposite parity. The selection rules follow the Wigner-Eckart theorem to give,

$$\langle \gamma JM|\, \mathbb{P}_q^{(1)}\, |\gamma' J' M'\rangle = (-1)^{J-M} \begin{pmatrix} J & 1 & J' \\ -M & q & M' \end{pmatrix} \langle \gamma J|\, |\mathbb{P}^{(1)}|\, |\gamma' J'\rangle \tag{4.11}$$

From the dipole line strength and the sum rules for the $3-j$ symbols, the total transition probability from a state $\gamma' J' M'$ to all states M of the level γJ is found to be

$$a = \frac{64\pi^4 e^2 a_0^2 \sigma^3}{3h} \mathcal{S} \sum_{Mq} \begin{pmatrix} J & 1 & J' \\ -M & q & M' \end{pmatrix}^2 = \frac{64\pi^4 e^2 a_0^2 \sigma^3}{3h(2J'+1)} \mathcal{S} \tag{4.12}$$

where $\mathcal{S}$ is the measure of the total strength of the spectrum line

$$\mathcal{S} \equiv |\, \langle \gamma J|\, |\mathbb{P}^{(1)}|\, |\gamma' J'\rangle\, |^2 \tag{4.13}$$

The weighted transition probability is given by

$$gA = (2J'+1)A = \frac{64\pi^4 e^2 a_0^2 \sigma^3}{3h} \mathcal{S} \tag{4.14}$$

which is related to the weighted oscillator strength, gf as follows

$$gA = \frac{8\pi^2 e^2 \sigma^2}{mc} \quad sec^{-1} \tag{4.15}$$

The intensity of the spectrum line is given by

$$I \propto \sigma g A \propto \sigma^4 \mathcal{S} \tag{4.16}$$

For strong spectral lines, f approaches unity and for strong spectral lines of neutral atoms, the transition probability $A \cong 10^8\ sec^{-1}$. For highly ionized atoms, the transition probabilities can be in the order of $10^{14}\ sec^{-1}$ or greater. For theoretical calculation of matrix elements, LS-coupled bases are considered simpler since the electric dipole operator does not involve the spin coordinates. The transition probabilities calculated in this thesis are for the LS-coupled bases.

4.2.4 The Principle of Detailed Balance

In statistical mechanics, the principle of detailed balance [9] relates the probabilities of forward and backward processes with the result that every process has its inverse, such that the initial state of the interacting particles is the final state of the inverse process. From the inverse of Fermi's Golden Rule for forward transition rates per unit time [5], we have

$$w_{f\to i} = \frac{2\pi}{\hbar} |\,\langle f|H|i\rangle\,|^2 \rho_i(E) \tag{4.17}$$

where H is the Hamiltonian of the interaction, $\langle i|$ is the initial state of the particles, $|f\rangle$ is the final state and $\rho_i(E)$ is the density of initial states. Since the Hamiltonian is a Hermitian operator, the matrix element for a process and its inverse are complex conjugates, giving

$$|\,\langle i|H|f\rangle\,|^2 = |\,\langle f|H|i\rangle\,|^2 \tag{4.18}$$

Dividing the forward process with its inverse gives the simple result

$$\frac{w_{i\to f}}{w_{f\to i}} = \frac{\rho_f(E)}{\rho_i(E)} \tag{4.19}$$

The detailed balance principle is used extensively in calculations of the rate coefficients of various atomic and ionic processes in plasmas, where information on the rate of one process enable calculation of its inverse.

4.3 Plasma in Thermal Equilibrium: Black-Body Radiation Distribution

For a plasma to be in thermodynamic equilibrium, all processes by which exchange of energy takes place must be exactly balanced by their reverse processes, so that there is no

net exchange of energy. Thus, in plasmas, ionization must be balanced by recombination, Bremsstrahlung by absorption, line radiation by line absorption, etc. When thermodynamic equilibrium exists, the distribution function of particle energies and excited energy levels of the atoms can be obtained from the Boltzmann distribution which is a function of the temperature. The Boltzmann population distribution for the ratio of the densities of atoms or ions of the same species and same ionization stage existing in two quantum levels with energies, E_n and E_m, is given by

$$\frac{N_n}{N_m} = \frac{g_n}{g_m} \exp[-(E_n - E_m)/k_B T] \tag{4.20}$$

where g is the statistical weight specific to each level. The Saha equation is a special application of this and describes the ionization balance which is given as

$$\frac{n_e N_{Z+1}}{N_Z} = \frac{g_{Z+1}}{g_Z} \left[\frac{2\pi m_e k_B T_e}{h^2}\right]^{3/2} \exp[-(I)/k_B T], \qquad n_e = \sum_{1}^{Z_{max}} Z N_Z \tag{4.21}$$

where n_e is the electron density, N is the populations of ions of various charges, g is the corresponding statistical weight, m_e is the electron mass, h is the Planck's constant, and I is the ionization potential of the ion-species in the lower excited state, or charge Z.

If we assume that thermal equilibrium exists inside a plasma, the radiation emitted can be approximated by treating the plasma as a black-body. Then the spectral distribution is given by the Planck's law

$$I_B(\lambda) = \frac{2\pi h c^2}{\lambda^5 \left(e^{hc/\lambda k_B T} - 1\right)} \tag{4.22}$$

Planck distribution always has its peak (the maximum spectral power) at the Wien's limit of Wien's displacement law, $E_{max} = 2.822 k_B T$, while 50% of the energy is carried by photons with energies greater than $3.505 k_B T$, and 10% of the energy is above $6.555 k_B T$. Most of the energy in the field is thus carried by photons with energies much higher than the average

particle kinetic energy. According to the Stefan-Boltzmann radiation law, the black body will emit radiation with an intensity that is obtained by integrating over all wavelengths and given to be

$$I = \sigma T^4 \tag{4.23}$$

where

$$\sigma = \frac{\pi^2 k_B^4}{60 c^2 \hbar^3} \tag{4.24}$$

is the Stefan-Boltzmann constant written in terms of the Boltzmann constant k_B, the speed of light c and $\hbar$ is the Plancks constant divided by 2π. Experimental comparisons of radiation spectrum from a black-body and a laser plasma at the same temperature have shown that the plasma Bremsstrahlung continuum emission peaks at wavelengths $\approx$ 2.5 longer than for the black body [10]. A rough estimate of plasma temperature, T (eV), necessary for generating photons of energy $\hbar\omega = 92\,eV(13.5nm)$ can be estimated using Wien's limit at $E_{peak} = 2.822kT$, to be near 35 eV with a corresponding intensity of 10^{11} W/cm^2.

There are two cases to be considered for the thermal equilibrium approximation in the limit of negligible and large optical depth, τ. The plasmas can be considered optically thick, or optically thin for the radiation. For $\tau \gg 1$, where the plasma is optically thick, the radiated intensity is reabsorbed (self-absorption) leading to the modification of the original spectrum radiated by the plasma interior. Optically thick, dense plasmas can be considered to be in thermal equilibrium. For $\tau \ll 1$, the plasma is optically thin and the intensity of radiation emitted is proportional to the plasma thickness and to the emission coefficient related to the different mechanisms such as free-free, free-bound, bound-bound emissions that are active inside the plasma. In this case thermodynamic equilibrium is rarely achieved, especially in short-lived, under dense, laboratory plasmas. Deviations from total equilibrium must be taken into consideration leading to more complicated calculations. It is possible for a plasma

to be optically thick for one spectral region while optically thin for another spectral region [10], as well, causing further deviation from thermal equilibrium. An optically thin plasma in characterized by line radiation, since the emitted lines are not reabsorbed into the plasma.

4.4 Emission of Electromagnetic Radiation from Plasmas

Due to the nature of the particles making up the plasma, kinetic, excitation, ionization and radiative energies contribute to the system states. The equilibrium distributions corresponding to each of the mentioned energy states are Maxwell, Boltzmann, Saha, and Planck functions, respectively. Each energy state is determined by a specific temperature T, and complete thermodynamic equilibrium would only exist if all forms of energy distributions are described by the same temperature. Laser plasmas are rarely in thermal equilibrium, but exhibit equilibrium distribution of one type or another. A Maxwell (or Maxwell-Boltzmann) distribution of velocities and populations are typically assumed for laboratory plasmas of low n_e, and high T_e, where

$$n_e \ll \Lambda^{-3} = (2\pi m k_B T_e/h^2)^{3/2}, \qquad \Lambda = h/\sqrt{2\pi m k_B T_e} \tag{4.25}$$

so that the mean distance between electrons are much larger than the De Broglie wavelength Λ. The classical Maxwell distribution is

$$f(v)dv = \left(\frac{m}{2\pi k_B T_e}\right)^{3/2} \exp\left(-\frac{mv^2}{2k_B T_e}\right) 4\pi v^2 dv \tag{4.26}$$

which satisfies the normalization condition $\int f(v)dv = 1$, and the average speed is $\bar{v} = \sqrt{8k_B T_e/\pi m}$. The corresponding energy distribution function is

$$f(E)dE = 2\left(\frac{E}{\pi}\right)^{1/2} (k_B T_e)^{-3/2} \exp[-E/k_B T_e] dE \tag{4.27}$$

with normalization, $\int f(E)dE = 1$. The average energy is $\bar{E} = 3k_BT_e/2$.

Black bodies are opaque to radiation emitted. Laser plasmas can be totally transparent, partially transparent, or totally opaque depending on the plasma parameters, ionic composition, and the wavelength of radiation emitted. Three major mechanisms contribute to the complex emissions, W_t, from a laser plasma, and these are (1) a Bremsstrahlung continuum, W_{ff}, due to free-free transitions, (2) a recombination continuum, W_{fb}, from free-bound, and (3) and line emission, W_{bb}, from bound-bound electron states, where

$$W_t = W_{ff} + W_{fb} + W_{bb} \tag{4.28}$$

4.4.1 Bremsstrahlung Continuum

The Bremsstrahlung continuum is emitted by free electrons of given kinetic energy in the field of ions in a plasma.

$$e^- + E_i + Z \rightarrow e^- + E_f + Z + h\nu_{ff}, \qquad h\nu_{ff} = E_i - E_f \tag{4.29}$$

The electron is free before and after the emission of radiation, hence the label free-free emissions. With Maxwellian distribution of electron velocities, an electron of initial velocity v interacting with an ion giving an impact parameter b has the characteristic interaction time, $\tau = 2b/v$. The dominant frequency in the radiated electromagnetic spectrum is $\nu = 1/2\pi\tau = v/2\pi b$. The power radiated is given to be,

$$W_{ff} = \frac{32\pi^2}{3^{3/2}} \frac{Z^2 e^6}{mc^2} \frac{n_e n_i}{6} \left(\frac{2k_BT_e}{\pi m}\right)^{1/2} = 1.6 \times 10^{-27} Z n_e^2 [T_e(K)]^{1/2} \quad \texttt{erg}\ s^{-1}cm^{-3} \tag{4.30}$$

Strong dependence on the electron density, ionic charge, and the electron temperature is observed. For the spectral distribution, taking into account the spectral intensity per unit

wavelength, is

$$W_{ff}^{\lambda} = 2.0 \times 10^{-27} Z n_e^2 [T_e(K)]^{1/2} \lambda^{-2} \exp\left[-\frac{hc}{\lambda k_B T_e}\right] \quad \texttt{erg}\ s^{-1} cm^{-4} \tag{4.31}$$

The spectral maximum occurs at $\lambda_{max}[nm] = 620/T_e[eV]$ for $hc/\lambda k_B T_e \approx 2$. This emission profiles are similar to that of a black body. The plasma behavior to a certain degree is as if in thermal equilibrium. The major difference is the wavelength of maximum emission for black body radiation which is given by $\lambda_{max}[nm] = 250/Te[eV]$. This is much shorter than for the Bremsstrahlung emission. The temperature for black body scales as T^4 while Bremsstrahlung scales as $T^{1/2}$.

4.4.2 Recombination Continuum

Recombination continuum is emitted when a free electron with a kinetic energy E_i is captured by an ion of charge Z in a plasma. Initially free electron is bound by the ion, hence labeled free-bound emissions. The spectrum begins where the photon energy equals the ionization potential energy, and the shape depends on the local kinetic energy distribution of the electrons.

$$e^- + E_i + Z \rightarrow (Z-1) + h\nu_{fb}, \qquad h\nu_{fb} \leq E_i + E_{\infty}^{Z-1} \tag{4.32}$$

The spectral intensity of recombination continuum is typically expressed in terms of Bremsstrahlung continuum [10] and the ration of the two is given by,

$$\frac{W_{fb}}{W_{ff}} = \frac{2Z^2 E_H}{k_B T_e} \sum_{n=1}^{\infty} \frac{1}{n^3} \approx 2.4 \frac{Z^2 E_H}{k_B T_e} \tag{4.33}$$

where E_H is 13.6 eV. According to this result, for plasmas in low-Z and/or high temperature, Bremsstrahlung emission overcomes recombination emission.

4.4.3 Line Emission

Transitions of bound electrons of an ion from an excited state to lower state emits radiation of given energy.

$$e^- + E_i + Z(m) \rightarrow e^- + E_f + Z(n), \qquad h\nu_{bb} = E_n - E_m = \Delta E_{nm} = E_i - E_f \tag{4.34}$$

The emitted radiation is characteristic of the targets used in the plasma generation. Line emission can result from resonance transitions where transitions are from higher excited states to the ground state and as a result of transitions between excited states. Resonance transitions are intense, but the weaker transitions between excited states are typically more useful in plasma diagnostics. Observed spectral line shapes are typically influenced by the natural lifetime, the motion of the emitting ion and the interactions with the plasma particles and fields. Line emission is of particular importance in the study of hot, dense plasmas where the atoms are not completely stripped. For this study, optimizing line emission from laser plasmas into the 13 nm region of the electromagnetic spectrum is the main focus. For this purpose, the emission spectrum from a laser-plasma source is tuned by varying the target materials and changing key plasma parameters. The following section will outline the various processes that influence line shapes observed from a light source.

4.4.4 Broadening Mechanisms in Line Radiation

In most quantum mechanical considerations, a spectral line is described to have a definite wavelength, to be monochromatic and to have zero energy width. In actuality, spectral lines are not infinitely narrow. Each spectral transition is characterized by an intensity distribution over a finite wavelength/wavenumber range and can be described by a

normalized intensity distribution function. This is called the natural line width or broadening of lines. For spontaneous decay to occur from an excited state to a lower state in an atom, the excited state must have a finite natural lifetime. The natural lifetime τ_j of the atom in any one of the states of the level j is given by

$$\tau_j = \left(\sum_i A_{ji}\right)^{-1} \tag{4.35}$$

For finite lifetimes, the uncertainty principle $\Delta E \cong \hbar/\Delta t$ implies a finite width of the level j. For example, in neutral atoms with typical electronic excited states with energies of several eV has lifetimes, Δt of about or greater than 10^{-8} sec. The corresponding energy uncertainty of any excited level is $\Delta E/hc \cong 1/(2\pi c\Delta t) = 5 \times 10^{-4}\ cm^{-1}$. The uncertainty in the wavenumber of each spectral line is given by

$$\Delta E = h\Delta\nu; \qquad \Delta\nu \approx \frac{1}{2\pi\Delta t} = \frac{1}{\tau_j} = \left(\sum_i A_{ji}\right) \tag{4.36}$$

The natural width is the minimum width possible for a spectral line and it is negligible relative to other line broadening mechnisms. The line shape of a transition with only natural broadening is approximated by a Lorentzian intensity distribution function.

Line shapes are usually approximated by a Lorentzian or a Gaussian distribution function. A Lorentzian has the general formula,

$$F(\upsilon) = K\left[\frac{1}{1 + (\upsilon - \upsilon_0)^2}\right] \tag{4.37}$$

where K is some constant, υ is the frequency, and υ_0 is the center of the line. The Gaussian function has the general formula,

$$F(\upsilon) = K \exp[-k(\upsilon - \upsilon_0)^2] \tag{4.38}$$

These two functions are used in spectroscopic line width studies to fit an experimental spectral line. Line widths in measured spectra can result from several broadening mechanisms

depending on the radiative conditions. In laser plasmas, pressure or collision broadening, Doppler broadening, and Stark broadening, etc. can occur. There can also be broadening as a result of instrument parameters.

Doppler Broadening

This is the most common broadening phenomena in ionized gases. Doppler broadening occurs when gas-phase species moves towards or away from the sources and/or detector causing changes in the apparent energy of transitions. The Doppler line width due to the thermal velocity of the emitting ions of mass, A, in a plasma with an ion temperature of $k_bT\ \ (eV)$ is given by [11],

$$\frac{\Delta\lambda}{\lambda} = 7.7 \times 10^{-5} \left(\frac{k_bT}{A}\right)^{1/2} \tag{4.39}$$

The transition is obviously from a higher level to a lower level. The widening of the spectral line follows the Gaussian intensity distribution profile.

Pressure Broadening

Pressure broadening is caused by collisions between emitters with the neighboring particles. This leads to the alteration of energies of the ground or excited states. Collisions decrease the natural lifetimes of atoms resulting in a Lorentzian line profile. Details on the theory of calculating pressure broadening profiles can be found in references [2, 3]. Pressure broadening is minimized at lower pressures.

Resonance Broadening

Resonance broadening occurs between identical species. It is confined to electric dipole transitions between an upper or lower level to the ground state. The line width displays a Lorentzian profile and is estimated as

$$\Delta\lambda^R_{1/2} \simeq 8.6 \times \left(\frac{g_i}{g_j}\right)^{1/2} \lambda^2 \lambda_r f_r N_i \tag{4.40}$$

where λ is the wavelength of the observed line, f_r and λ_r are the respective oscillator strength and wavelength of the resonance line, g_j and g_i are the statistical weights of the upper and lower levels, N_i is the ground state population.

Stark Broadening

The presence of external electric and magnetic fields will cause either a slight decrease or increase in the energy of an atom. Splitting of the energy levels in to multiple sub-levels occur with the magnitude of the splitting depends on the field strength. This results in splitting a single spectral line into several components where this effect is labeled *Stark Effect* in the case of electric fields and *Zeeman Effect* in the case of magnetic fields. Correspondingly, the broadening mechanisms observed for time averaged spectral measurements is called Stark or Zeeman broadening. Stark broadening due to charged perturbers; electrons and ions, dominates resonance broadening in plasmas. The Stark width for hydrogen lines is given by

$$\Delta\lambda_{1/2} = 2.5 \times 10^{-9} \alpha_{1/2} N_e^{2/3} \tag{4.41}$$

where N_e is the electron density, and $\alpha_{1/2}$ is tabulated half-width parameter from references.

Voigt profiles

Generally, an experimentally observed spectral line shape is a result of several broadening mechanisms. Significant contributions to a line shape arise from resonance and Doppler broadening or from pressure and Doppler broadening. Thus, the observed line shapes are convolutions of both Gaussian and Lorentzian functions and are known as Voigt profiles. Voigt profiles are evaluated by means of numerical integration methods in quantitative spectroscopy.

Other Broadening Mechanisms

Power saturation is another mechanism that effects the line shape. In this case, the incident light beam is extremely intense causing faster absorption than radiative decay of excited states. The ground state populations are almost completely depleted.

Line shapes can also be influenced by hyperfine structure, isotopic shift and self-absorption. Another major source of observed line broadening is due to the properties of the instruments being used. A slit of a given physical width in a dispersive spectrometer adds to the broadening of spectral lines. Diffraction effects, optical aberrations, and finite resolving power of the spectroscopic apparatus being used will alter the line shape [8]. Spectrometer components also attenuate the line intensities, thus for absolute intensity measurements calibration of instrument sensitivity to a source with known energies is necessary.

4.4.5 The Inglis-Teller Limit

A result of Stark line broadening is the merging of broadened spectral lines at the Inglis-Teller limit [12]. The highest resolvable principal quantum number n_p for ions of charge Z_e perturbed by single charges ions is [13, 1].

$$7.5 \log n_p = 23.26 - \log N_e + 4.5 \log Z \tag{4.42}$$

In cases where the reduction of ionization potential is not dominant, this limit can be used as an approximate indicator of electron density.

4.4.6 Unresolved Transition Arrays and Super Transition Arrays

Discrete line radiation from bound-bound transitions are typically observed for low-Z plasmas with a few bound electrons. The line radiation emitted from a high-Z, highly ionized plasma is numerous. Many ionization stages existing in the plasma emit 100's of lines in to the same spectral region where the line spacing between transitions become smaller than the line width of each transition. Thus, these lines are said to be unresolvably close together resulting in observed spectral features that are labeled as *unresolved transition arrays (UTA)*.

In extremely high density plasmas, the number of populated configurations increase rapidly due to collisional excitation among various states and the number UTAs grow to intractable quantity [5]. An ion with $n_{max} = 10$ bound ionic shells gives 10^{15} individual transitions in to about 10^9 UTAs. For analysis of such spectra, the closely spaced electronic configurations are grouped together in to a *superconfiguration* and the transitions between the superconfigurations are called the *super transitions arrays (STA)* [5].

4.5 Equilibrium Conditions for Population Distributions in Plasmas

For a plasma with Maxwellian free electron velocity distribution, several models exist where information on the ionic population distribution as a function of temperature can be calculated for given electron densities. The models are specific for the equilibrium conditions where certain intrinsic assumptions are made about the nature of the plasmas and an outline of these models and validity conditions are provided in the following sections.

4.5.1 Atomic Processes in Population Kinetics

As stated previously, the radiation emitted from a plasma is determined by the combined effects of a large number of physical processes. McWhirter and Hearn [14, 15], J. Davis et. al [16], D. Saltzmann [5], and many others have formulated extensive descriptions and have completed calculations on the various atomic processes involved in the dynamics of laboratory plasmas. In hydrogen like ions, a multitude of competing processes take place in the recombination of electrons, e, with bare ion, Ze, with the reversible reaction written as (fig. 4.1) [17, 16],

$$S_Z + e \Leftrightarrow S_{Z-1} \tag{4.43}$$

Some of the more important processes that are of relevance to laboratory plasmas are:
Three-body recombination, $\beta(p)$:

$$S_Z + e + e \rightarrow S_{Z-1}(p) + e \tag{4.44}$$

Collisional Ionization, $S(p)$:

$$S_{Z-1}(p) + e \rightarrow S_Z + e + e \tag{4.45}$$

Radiative Recombination, $\alpha(p)$:

$$S_Z + e \rightarrow S_{Z-1}(p) + h\nu \tag{4.46}$$

Photoionization, $B(q,p)J$:

$$S_{Z-1}(p) + h\nu \rightarrow S_Z + e \tag{4.47}$$

Collisional De-excitation, $X(p,q)$:

$$S_{Z-1}(p) + e \rightarrow S_{Z-1}(q) + e \tag{4.48}$$

Collisional Excitation, $X(q,p)$:

$$S_{Z-1}(q) + e \rightarrow S_{Z-1}(p) + e \tag{4.49}$$

Spontaneous/Stimulated Emission, $A(p,q)$:

$$S_{Z-1}(p) \rightarrow S_{Z-1}(q) + h\nu \tag{4.50}$$

Photoexcitation, $B(q,p)J'$:

$$S_{Z-1}(q) + h\nu \rightarrow S_{Z-1}(p) \tag{4.51}$$

where p and q are the principal quantum numbers of the discrete levels. The rate coefficients for the first six processes listed above, depend upon the plasma electron temperature. There are two additional processes that need to be considered for non-hydrogenic plasmas and these are;

Dielectronic recombination:

$$S_Z(i) + e \rightarrow S_{Z-1}(nl) \tag{4.52}$$

and Autoionization:

$$S_{Z-1}(j,nl) \rightarrow S_{Z-1}(i,nl) + h\nu(ij) \tag{4.53}$$

Other processes involved, but not considered, are inner shell, higher-order processes and charge exchange. The rate coefficients with electron density n_e are given by equations of the form,

$$\begin{aligned}\frac{dn(Z,p)}{dt} &= -n(Z,p)\left(n_e S(T_e,Z,p) + N_e \sum_{q\neq p} X(T_e,Z,p,q) + \sum_{q<p} A(Z,p,q)\right) \\ &+ N_e \sum_{q\neq p} n(Z,q) X(T_e,Z,p,q) + \sum_{q<p} n(Z,q) A(Z,p,q) \\ &+ n_e n(Z+1,g) \times (n_e \beta(T_e,Z+1,p) + \alpha(T_e,Z+1,P)) \end{aligned} \quad (4.54)$$

To simulate plasma emission and to determine charge-state distributions in plasmas, these processes are calculated over many energy levels and several ionization stages.

4.5.2 Local Thermodynamic Equilibrium

In a high density plasma, collisional processes dominate with higher probability of collisional de-excitation than radiative decay. Plasma is optically thick to its own thermal radiation. For the case of energy levels within a given ionization state, collisional cross sections increase with increasing quantum number and radiative rates decrease giving a critical quantum level above which LTE prevails. The density and temperature of the plasma above this critical level is treated the same as in thermal equilibrium, except lines are the characteristic emissions of a plasma in LTE.

For LTE thermodynamics to be valid in an optically thin plasma, the density requirement [1, 16],

$$n_e \geq 9 \times 10^{17} T_e^{1/2} \left(\frac{\Delta E}{E_H}\right)^2 \left(\frac{T_e}{E_H}\right)^(1/2) \quad cm^{-3} \quad (4.55)$$

must be met, where $\Delta E(eV)$ is the largest interval between adjacent energy levels of the ions and temperature, T_e is in eV. LTE applies to low-Z plasma states and the SAHA equation

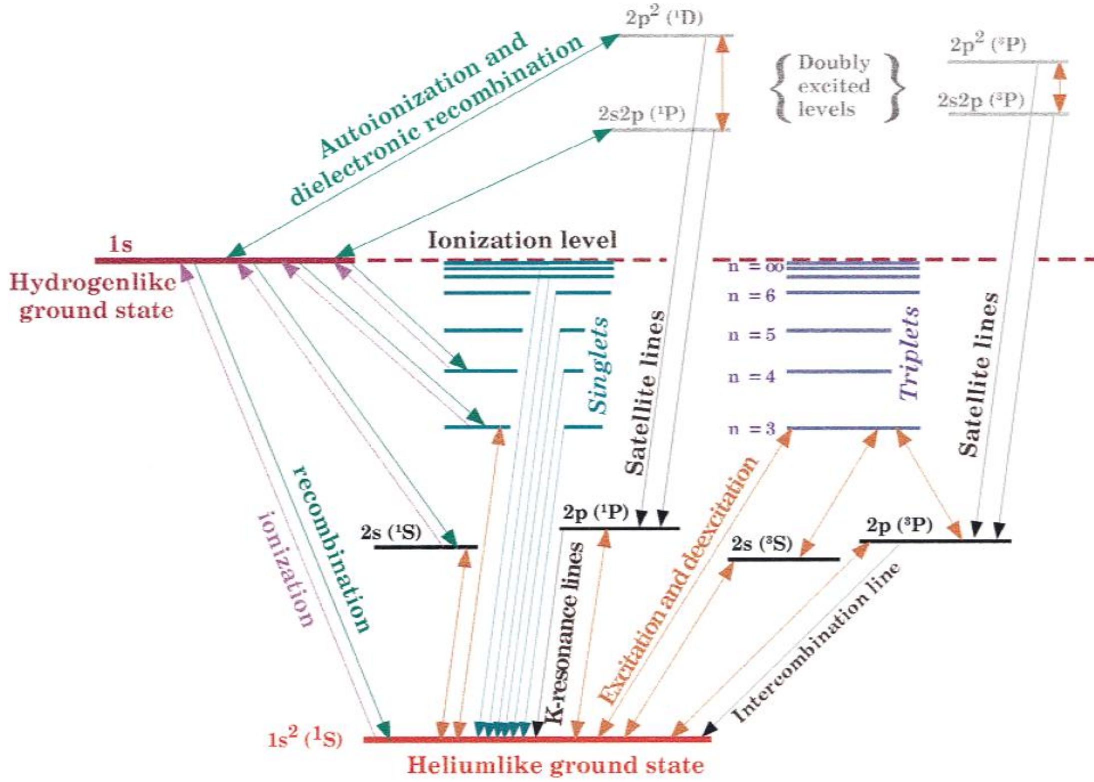

Figure 4.1: He-like atom energy level structure showing various atomic processes [16]

can be used to approximate density of states.

$$\frac{n_e N_{Z+1}}{N_Z} = \frac{2g_{Z+1}}{g_Z}\left[\frac{2\pi m_e k_B T_e}{h^2}\right]^{3/2} \exp(-(I)/k_B T), \qquad n_e = \sum_{1}^{Z_{max}} Z N_Z \tag{4.56}$$

4.5.3 Non-LTE Collisional Radiative Equilibrium Model

Collisional Radiative Equilibrium (CRE) Model takes into account both radiative and collisional processes. This model is considered to be the most appropriate model for a high temperature, high-density, laser produced plasma. For CRE equilibrium considerations of a Maxwellian plasma that has shorter electron-electron relaxation times than the electron heating time, several validity conditions must be met, and they are

- During plasma evolution, the $Z+1$ ion charge density do not change significantly while the ions of charge Z are reaching near steady-state population distribution, i.e, difference between ionization and recombination rate is negligible compared to other processes.

- $k_B T_e$ must be greater that 10 eV.

- Plasma must be optically thin to its own radiation. In the case of line emissions, plasma opacity must be considered for each transition.

For time dependent rates of population, the CRE model takes the simple form

$$\frac{dn(Z)}{dt} = n_e \left[-S(Z)n(Z) - \alpha_R(Z)n(Z) + S(Z-1)n(Z-1) + \alpha_R(Z+1)n(Z+1)\right] \quad (4.57)$$

where $S(Z)$ is the collisional ionization rate and the total recombination rate α_R is the sum of radiative and three-body recombination rates

$$\alpha_R(Z) = \alpha_r(Z) + \beta_{3b}(Z) \quad (4.58)$$

House [18], Colombant and Tonon [19], etc. have shown that for two successive ionization stages in a plasma,

$$\frac{n(Z+1)}{Z} = \frac{S(Z)}{\alpha_r(Z+1) + N_e \beta_{3b(Z+1)}} \quad (4.59)$$

This formulation allows the calculation of fractional ionic density of charge Z of the total ionic population in the plasma. Fig. 4.2 shows an example of the CRE model based calculation completed for Xenon [20] giving the ionic distribution as a function of temperature.

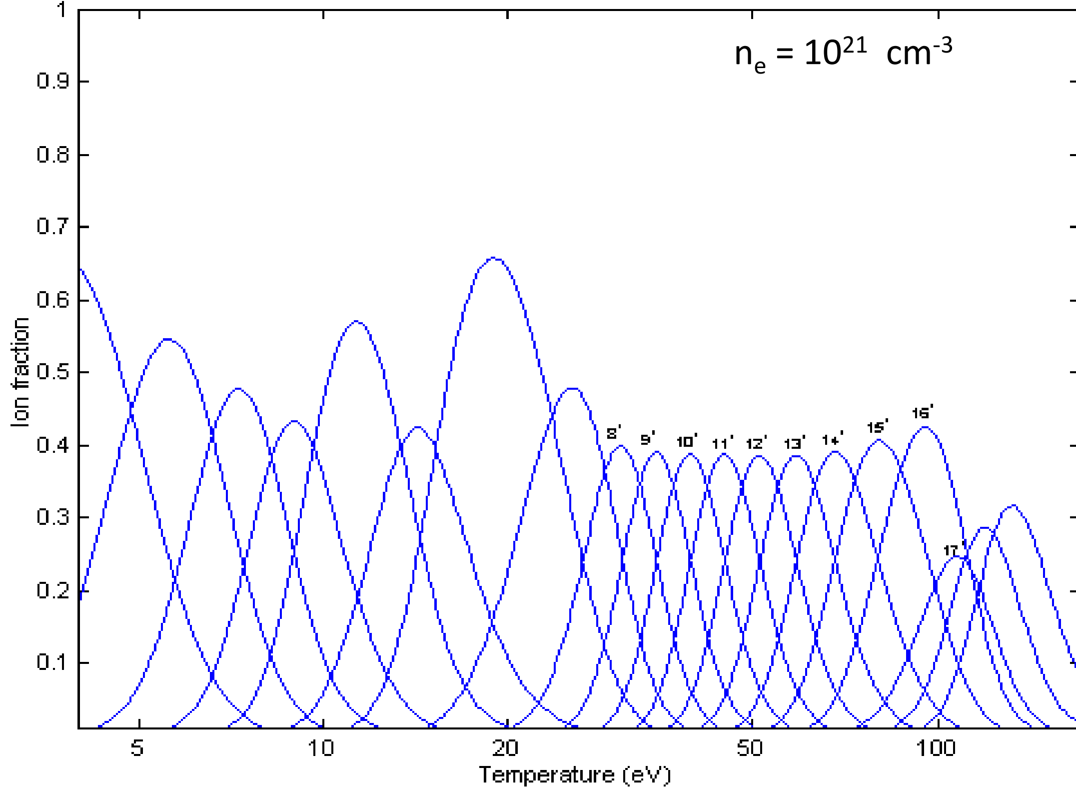

Figure 4.2: CRE model calculaiton of Xenon ionic charge densities as function of temperature

4.5.4 Coronal Equilibrium Model

Coronal Equilibrium Model (CEM) is valid in the outer regions of an optically thin, low mass and density plasma where most of the ion populations exist in the ground state. Again, a maxwellian plasma is assumed to be optically thin with collisional excitation from the ground state assumed to be balanced by radiative decay from upper level to all lower levels. Thus, the validity condition requires that the ions of charge Z in level n

$$n_e \leq 6 \times 10^{10}(Z+1)^6 T_e^{1/2} \exp\left[\frac{(Z+1)}{10T_e}\right] \quad cm^{-3} \tag{4.60}$$

where T_e is in eV. Then the relationship between different ionization stages in the steady state coronal equilibrium is given by

$$\frac{n(Z-1)}{n(Z)} = \frac{\alpha_r}{S(Z-1)} \tag{4.61}$$

The above relationship shows no dependence on electron density, since all rates involved in reaching equilibrium is proportional to the electron density. There is no three-body recombination as well. Thus, CRE model approximates to LTE when collisions dominate radiative decay and it approximates to CEM when radiative rates dominate collional de-excitations.

4.6 Spectroscopy as a plasma diagnostic

Plasma spectroscopy establishes relationships between the line and continuum emissions from a plasma to the physical nature of the plasma. Thus, a detected spectrum is essentially the fingerprint of the plasma physical state. The average plasma temperatures and densities, ionic distributions, particle transport properties, and much more can be calculated from a measured emission spectrum of a plasma. The experiments described in the subsequent chapters of this document utilize emission spectroscopy as the primary analytical method for the determination of plasma state. Spectroscopy is used to isolate plasma conditions that provide maximum emission of 13 nm radiation for various laser and target combinations.

4.7 References

[1] Hans R. Griem. *Plasma Spectroscopy.* McGraw-Hill Book Company, New York, 1964.

[2] Hans R. Griem. *Principles of Plasma Spectroscopy.* Cambridge University Press, New York, 1997.

[3] Hans R. Griem. *Spectral Line Broadening by Plasmas.* Academic Press, New York, 1974.

[4] Takashi Fujimoto. *Plasma Spectroscopy.* Clarendon Press, Oxford, 2004.

[5] David Salzmann. *Atomic Physics in Hot Plasmas.* Oxford University Press, New York, 1998.

[6] V. P. Shevelko and L. A. Vainshtein. *Atomic Physics for Hot Plasmas.* Institute of Physics Publishing, Philadelphia, 1993.

[7] Harvey Elliot White. *Introduction to Atomic Spectra.* McGraw-Hill Book Company, New York, first edition, 1934.

[8] Robert D. Cowan. *The Theory of Atomic Structure and Spectra.* University of California Press, Berkeley, first edition, 1981.

[9] F. Coester. Principle of detailed balance. *Phys. Rev.*, 84(6):1259, Dec 1951.

[10] Danilo Giulietti and Leonida A. Gizzi. X-ray emission from laser produced plasmas. *La Rivista del Nuovo Cimento*, 21(10):1–93, 1998.

[11] I. C. E. Turcu and J. B. Dance. *X-rays from Laser Plasmas: Generation and Applications.* Wiley, New York, first edition, 1999.

[12] D. R. Inglis and E. Teller. Ionic depression of series limits in cne-electron spectra. *The Astrophysical Journal*, 90:439–448, October 1939.

[13] M. H. Key and R. J. Hutcheon. Spectroscopy of laser-produced plasmas. *Adv. At. Mol. Phys.*, 16:201–280, 1980.

[14] R W P McWhirter and A G Hearn. A calculation of the instantaneous population densities of the excited levels of hydrogen-like ions in a plasma. *Proceedings of the Physical Society*, 82(5):641–654, 1963.

[15] R. W. P. McWhirter. Spectral intensities. In R. H. Huddlestone and S. L. Leonard, editors, *Plasma Diagnostic Techniques*, pages 201–210, 1965.

[16] J. Davis, R. Clark, M. Blaha, and J.L. Giuliani. Atomic physics and non-lte effects. *Laser and Particle Beams*, 19:557–577, October 2001.

[17] D. R. Bates, A. E. Kingston, and R. W. P. McWhirter. Recombination between electrons and atomic ions. ii. optically thick plasmas. *Royal Society of London Proceedings Series A*, 270:155–167, November 1962.

[18] L. L. House. Ionization equilibrium of the elements from h to fe. *Astrophysical Journal Supplement*, 8:307–320, January 1964.

[19] D. Colombant and G. F. Tonon. X-ray emission in laser-produced plasmas. *Journal of Applied Physics*, 44(8):3524–3537, 1973.

[20] Gerry O'Sullivan, Padraig Dunne, Emma Sokell, Anthony Cummings, Nicola Murphy, Kenneth Fahy, Paddy Hayden, Michael Lysaght, Luke McKinney, Paul Sheridan, and John White. Recent results on euv emission from laser produced plasmas with slab targets containing sn. Presentation at 3rd EUVL Symposium in Miyazaki in Japan. Proceedings available at www.sematech.org, November 2004.

CHAPTER 5

EUV GENERATION FROM PLANAR SOLID TIN TARGET

5.1 Introduction

Laser produced plasmas (LPP) that are generated from high-Z metal solid targets have demonstrated to be efficient emitters of EUV radiation. Among all of the elements investigated, tin (Sn) metal targets have shown to emit the most into the 13.5 nm BW [1, 2, 3]. The design and development of a high power EUV source for 13.5 nm requires adherence to a number of constraints that are related to efficiency and lifetime. The efficiency of the source into the needed emission BW is given by the conversion efficiency (CE). CE for laser plasmas is defined as the ratio of the laser energy input to the useful EUV light output generated. High-intensity, high repetition rate source operation for a large period of time (30,000 hrs for EUVL) is necessary for many applications, especially EUVL. The optics that are being used at these wavelength range are expensive, time consuming to fabricate, and are easily degraded. Because of this, any debris (particles, ions, clusters, aerosols, etc) produced during plasma generation and operation need to stay under acceptable limits [4, 5]. Early LPP experiments with tin slab targets showed copious amounts of debris being generated [6]. This lead to the dismissal of tin as a feasible target for high power EUV source development. In recent years, source developers have turned the focus back on to tin-based sources in order to generate the EUV power levels needed.

In order to produce a high power EUV source at 13.5 nm, Xenon (Xe) gas was initially

considered for gas discharge [7] and laser plasma sources. Target configurations of droplets and cylindrical jets were used in source schemes with the various geometries obtained by cryo-cooling of the Xe gas. With Xe being an inert gas, debris produced during plasma generation was expected to be lower. Unfortunately, the major emission band of Xenon in the EUV region is centered at 10.6 nm and not at 13.5 nm (Fig. 5.1). As a result, CE from Xe targets could not reach the levels necessary. Thus, Xe was deemed unsuitable as a target material for 13.5 nm EUV generation.

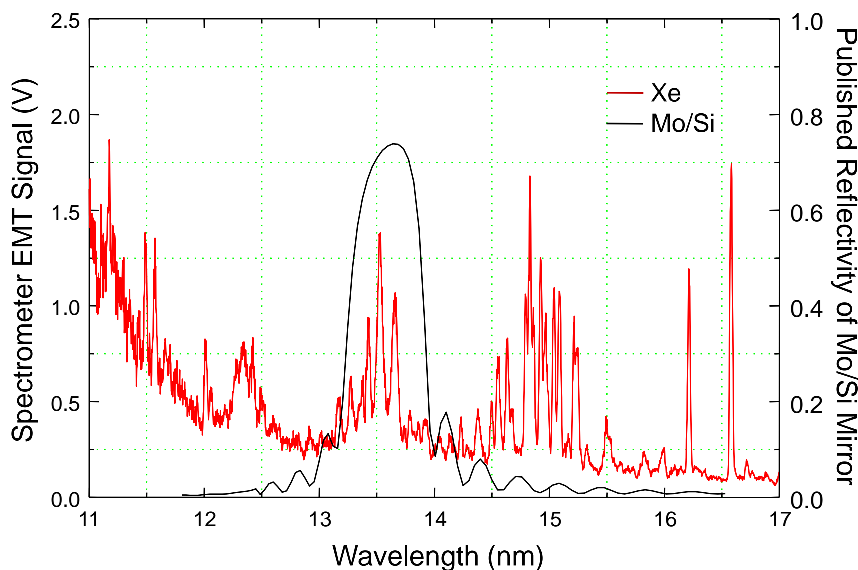

Figure 5.1: Spectrum from a Xenon plasma source in the EUV region [8].

In this chapter, extensive studies are completed for EUV generation from planar, solid Sn target. Plasma is generated by irradiating a tin slab using a focused laser beam from a solid-state Nd:YAG laser. Spectra are obtained for a number of input laser energies at the target. The energies used vary from 70mJ to 5mJ. Data was also collected for varying laser beam focus at fixed energies. Calibrated CE of laser light into EUV light into the narrow

2% bandwidth of the Mo-Si MLM is calculated for each measurement. The maximum CE calculated is approximately 4.9% at an intensity region near 1.2×10^{11} W/cm^2. It is observed that there is a strong dependence of laser irradiation intensity on the EUV conversion efficiency. Irradiance intensity is directly proportional to the plasma temperatures, thus the average Sn ion populations existing in the plasma. Varying intensity is shown to produce changes in the spectral measurements.

5.2 Tin as a Target Material for Plasma EUV source

Researchers around the globe are working on the radiative and spectral properties of materials for efficient EUV generation. They have identified a few elements to be the possible choices for high EUV-yield. Mo-Si MLMs have demonstrated reflectivities greater than 70% into a narrow (0.5 nm) BW centered at 13.5 nm. Tin, in comparison to the other elements that are being investigated for an EUV source, is shown to have many transitions in the required 13.5 nm region. The broad-band, UTA emission from Sn originating from the Sn^{12+} to Sn^{7+} ions with the ground configuration, [Kr] $4p^6 4d^n$ with n = 2 to 7 was found to be one of the highest near 13 nm.

From the black body radiation distribution laws it was estimated that an average plasma temperature of 35 eV at an intensity near 10^{11} W/cm^2 is needed to generate 92 eV (13.5 nm) photons. Results from higher level calculations completed for simulating the dynamics and for determining conditions required for 92 eV photon generation is presented in the next section.

5.2.1 Hydrodynamics and CRE model Calculations for Plasma Dynamics

Development of temperatures and densities in laser produced plasmas of planar solid tin target is modeled using the 1-D Lagrangian hydrodynamic code MED103 which is a modified MEDUSA code [9]. Details of the calculations implemented are described in detail in Chap. 3. Cell numbers of more than a 1000 can be used. In each cell, the electron and ion densities and temperatures, the average ion states and many other plasma parameters (velocity, pressure, etc.) are determined. Laser parameters such as laser pulse-shape, wavelength and intensity used and target parameters such as geometry, size, and atomic data can be specified for each calculation. Targets consisting of many layers of different materials can be evaluated. The ions in the code are always considered to have a perfect gas equation of state, usually with electron density obtained from the Fermi-Dirac distribution.

Fig. 5.2 models the solid Sn target irradiation with a 1064 nm, 10 ns pulse width, gaussian laser beam with a 35 μm beam diameter at focus. The irradiance intensity is specified to be 1×10^{11} W/cm^2. Plasma electron density and temperature as a function of plasma expansion is obtained from the data for specified number of time-steps from the beginning to the end of the laser pulse. Fig. 5.2 plots density and temperature information from 200 cells collected at 10 ns after the laser was turned on, which is the peak of the laser pulse width. Data was tabulated for many time-steps with the time separation for this calculation specified to be at 1 ns. Shorter time-steps can be specified, if better time resolution is required. The maximum electron temperature calculated by the code is 34 eV for a plasma generated under the specified conditions.

The CRE model is used to determine the average charge state populations of the Sn

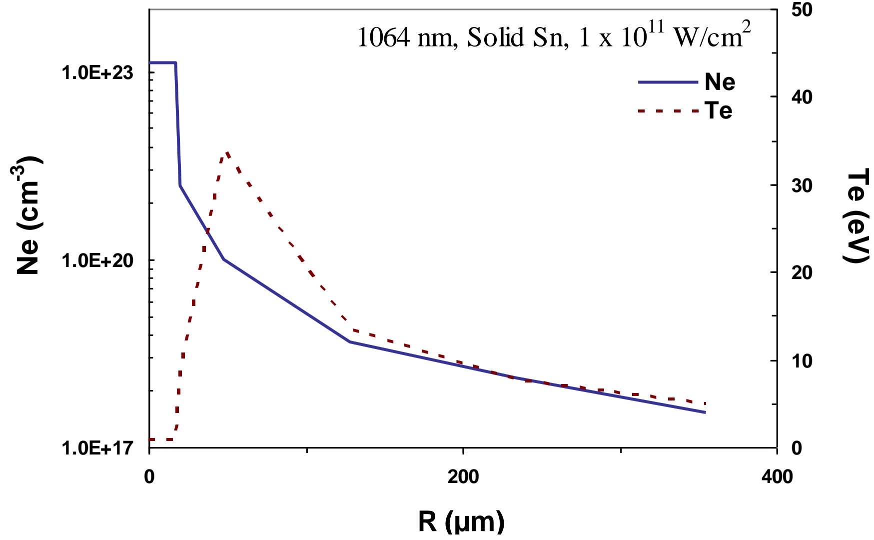

Figure 5.2: Plasma electron temperature and density expansion as function of distance at the peak of the laser pulse. Modeled using 200-cell MED103 for a 1064 nm, 10 ns gaussian beam irradiating solid Sn target.

ions as a function of temperature for a given electron density. CRE model is considered to be the most appropriate for a high temperature, high-density, laser produced plasma. Calculation of fractional ionic densities of the total ionic population based on the formulation below is completed for Sn ions of charge states up to Sn^{13+}. It is shown in 5.3 [5]. An electron density of 10^{21} /cm^3 is assumed, since the critical density of the 1064 nm laser beam is the same. The calculation shows that in the 30 eV- 40 eV plasma temperature region, the Sn ions, Sn^{9+} to Sn^{11+} is populated.

$$\frac{n(Z+1)}{Z} = \frac{S(Z)}{\alpha_r(Z+1) + N_e \beta_{3b(Z+1)}} \tag{5.1}$$

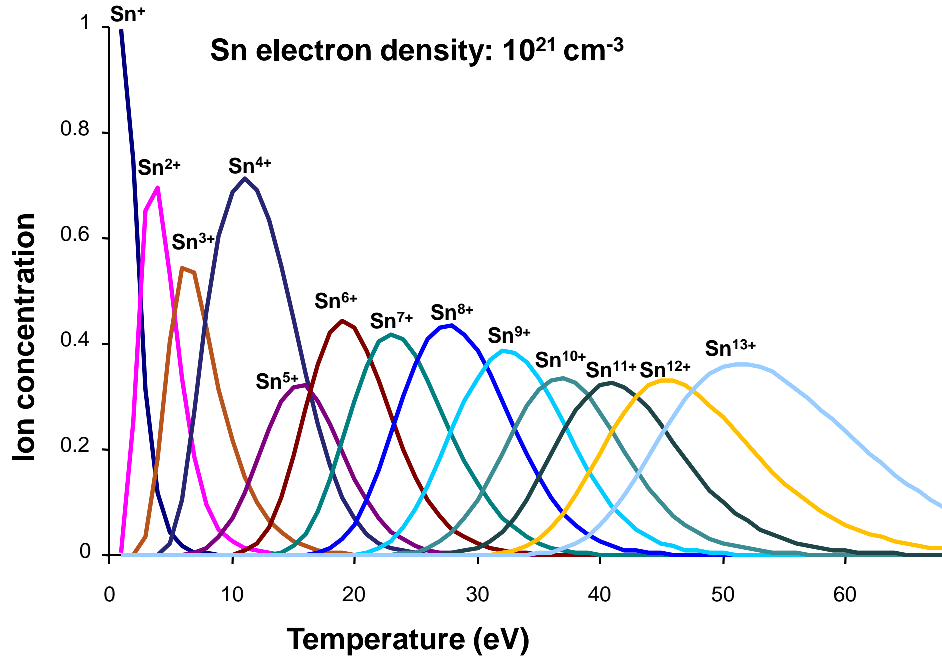

Figure 5.3: Population distribution as a function of temperature calculated using the CRE model.

5.2.2 Atomic Level Structure Determinations

A suite of four programs called the COWAN code was developed by R. D.Cowan for relatively simplified calculations of the atomic structures of elements. The COWAN code suite is freely available to the spectroscopy research community. These codes calculate atomic structures and spectra by utilizing the superposition-of-configuration method [10, 11]. Using the Hartree-Fock configuration interaction, bound or free one electron radial wavefunctions are calculated for specified electron configurations giving the center-of-gravity energy, E_{av}, and Coulomb and spin-orbit integrals for calculating the related energy levels in the first program of the suite. The second program in the code suite then calculates the configuration-interaction Coulomb integrals between each pair of interacting configurations

and the electric-dipole and/or electric quadrupole radial integrals between each pair of configurations. The third program computes angular matrix elements, energy levels, and atomic spectra with energy levels, transition wavelengths, radiative and autoionization transition rates, dielectronic recombination cross-sections, electron-impact excitation cross-sections and so on by setting up matrices for each possible value of the total angular momentum. For higher accuracy results, the fourth program in the code suite makes a least-squares fitting of atomic energy levels to obtain the best fit of experimentally known energy levels [11].

5.2.3 Calculated Oscillator Strengths of Transitions

As stated previously, Sn^{12+} to Sn^{7+} have the ground configuration, [Kr] $4p^6$ $4d^n$, n = 2 to 7. The structure of these spectra are determined by the incomplete shells of equivalent d electrons. The structure of d^{10-n} is the same as that of d^n [10]. Therefore, to evaluate these configurations, only the expressions for d^2 through d^5 are needed. For l^n, the quantum numbers are γLSJ (and M), the level structure depends on the Coulomb parameters $F^k(ll)$ and on the single spin-orbit parameter ζl. Because the electrons are equivalent and lie spatially close together, at least in the radial direction- their mutual Coulomb interactions are large and the physical coupling conditions tend to lie closer to the LS than to the jj limit. The exceptions are very heavy atoms where the spin-orbit interactions are also very large. The lowest-energy term of l^n is that term of maximum S, which has the largest value of L as expected from Hund's rule [10].

The $4d^n$ electron configurations (n =2 to 7) fall into the transition-series elements ^{38}Sr to ^{43}Tc. This series are preceded by the collapse into the atom core of a $4d$ orbital and involve the subsequent filling of the $4d$ subshell, which in neutral atoms is not the outermost subshell. Atomic orbitals are generated for the ground configurations $4d^n$ using

the radial wave-function code developed by COWAN. For a set of equivalent electrons (nl^n), the LS terms can be predicted by the vector model after the limitation of Pauli principle. In Table 5.1, a list the permitted LS terms for the configurations d^n, with n = 2 to 7 are given [12, 13]. Fig. 5.4 is an example of the term structure determination from the average

Table 5.1: Permitted LS terms for d^n subshells. The subscripts indicate the number of different terms having the same value of LS. All of them are even parity [13].

				Total Number
d^2, d^8	^{1}(SDG)	^{3}PF		5
d^3, d^7	^{2}(PD$_2$FGH)	^{4}PF		8
d^4, d^6	^{1}(S$_2$D$_2$FG$_2$I)	^{3}(P$_2$DF$_2$GH)	^{5}D	16
d^5	^{2}(SPD$_3$F$_2$G$_2$HI)	^{4}(PDFG)	^{6}S	16

configuration energies for tin ions that emit in the EUV region [13, 12]. The term structures are shown to be the same for $4d^n$ and $4d^{10-n}$, but the energy levels are different because of the Coulomb parameter, F^k. The LS interaction separations (ζ) are different, as well as the intervals between the levels of the same term. The LS composition in the corresponding levels demonstrate small variations, which are accounted for in the statistical weight term, g. In Fig. 5.4, Sn^{11+} ion is shown to have 39 electrons (Y-like). The ground configuration is $[Kr]4p^6 4d^3$, which has eight terms with 19 levels separated by 11.33 eV, and an average ionization energy of 231.33 eV. The ground state is $[Kr]4p^6\,(^1S)4d^3\,{}^4F_{3/2}$. In comparison, the Sn^{7+} ion has 43 electrons (Tc-like). The ground configuration is $[Kr]4p^6 4d^7$ with eight terms and 19 levels separated by 9.8 eV. The average ionization energy is 137.83 eV. The ground state is $[Kr]4p^6\,(^1S)4d^7\,{}^4F_{9/2}$ [12].

In the case of tin, most of the lines in the spectral region around 13.5 nm come from the transitions between the excited configurations, $4p^5 4d^{n+1}$ and $4p^6 4d^{n-1} 4f^1$. The transition probabilities are calculated using COWAN suite of codes is given in fig. 5.5. Most of the emission into 13.5 nm BW comes from the ions Sn^{9+}, Sn^{10+} and Sn^{11+}.

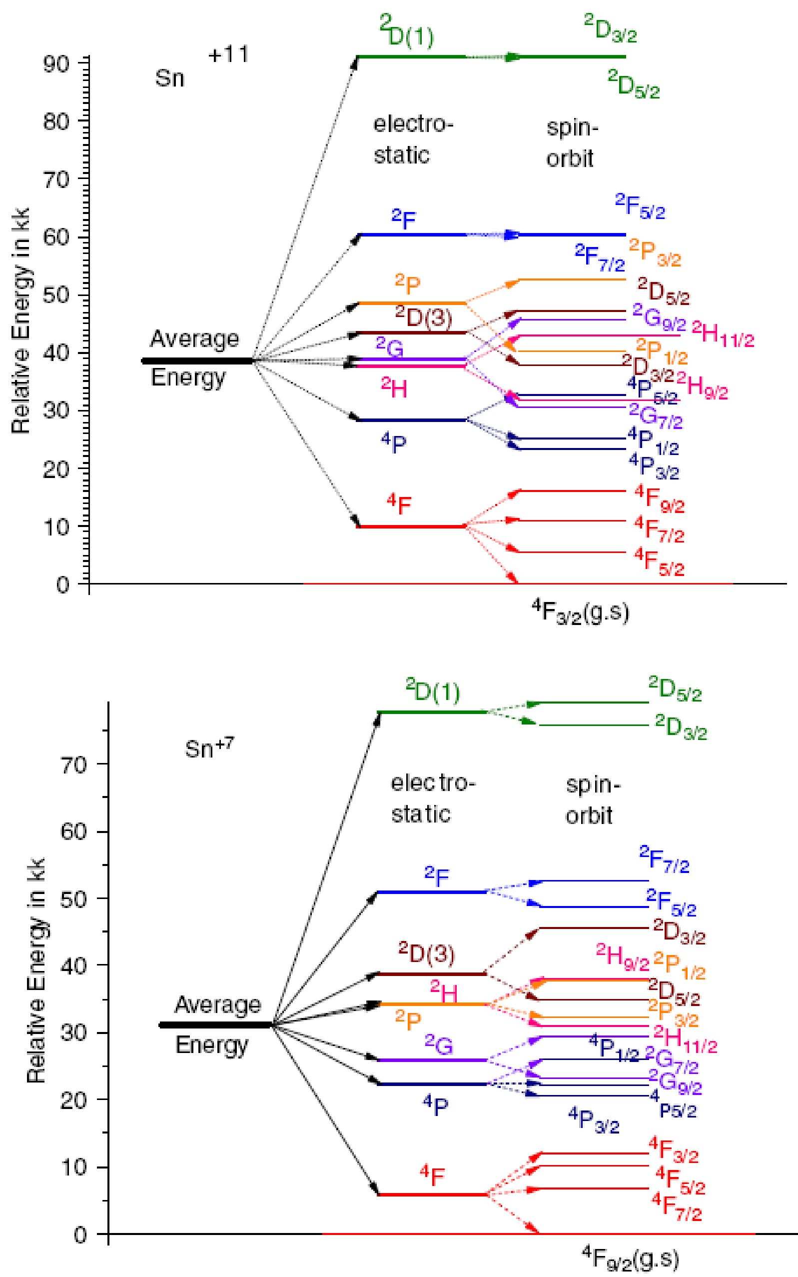

Figure 5.4: Relative Energy levels in Sn^{11+} and Sn^{7+} [13, 12].

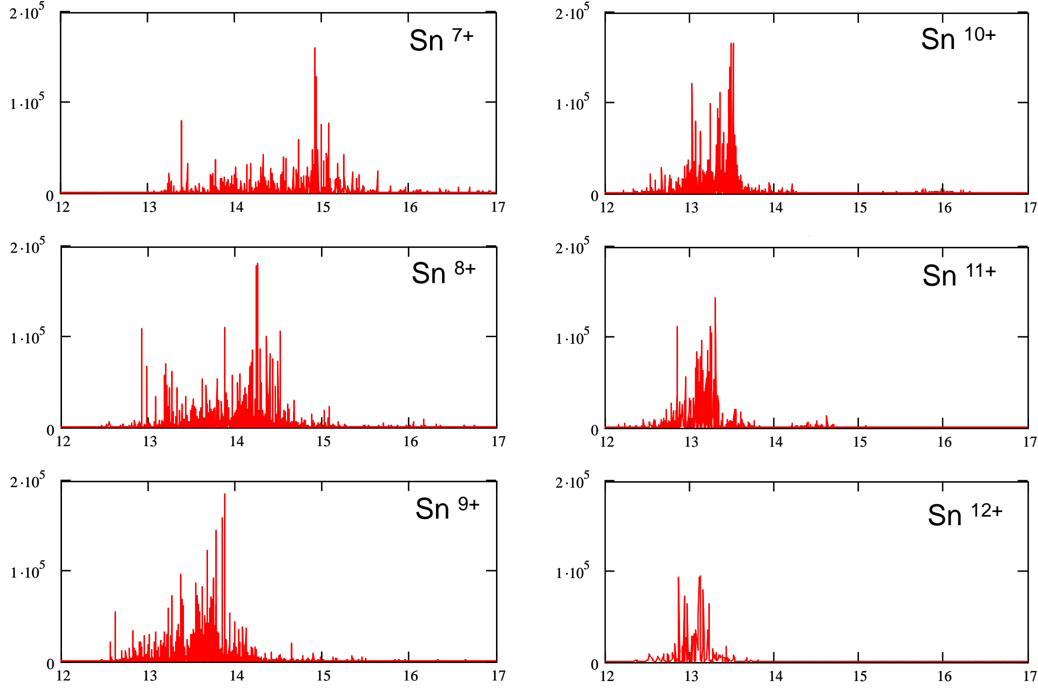

Figure 5.5: COWAN code calculated transition probabilities for Sn atoms contributing to emission in the 13 nm -14 nm region

The high density of transitions leads to unresolved transition arrays in the Sn spectral profile. Analysis of the UTA features require statistical methods. The UTA arising from each Sn ions is characterized by position width and symmetry. A method to simplify plasma modeling with nth-order, noncentered moments of the distribution μ_n is presented in reference [14]. μ_n are determined and expressed in terms of λ_i and weighted oscillator strength gf_i for each line i and this given below.

$$\mu_n = \frac{\sum_{i=1}^{N}(\lambda_1)^n gf_i}{\sum_{i=1}^{N} gf_i} \tag{5.2}$$

Then, expressed in terms of the mean (μ_1) and the standard deviation (σ), an UTA can be

represented by a Gaussian,

$$f(x) = \frac{1}{\sigma\sqrt{2\pi}} \exp[(x - \mu_1)^2/2\sigma^2] \tag{5.3}$$

where the area is equal to the summed oscillator strengths [14].

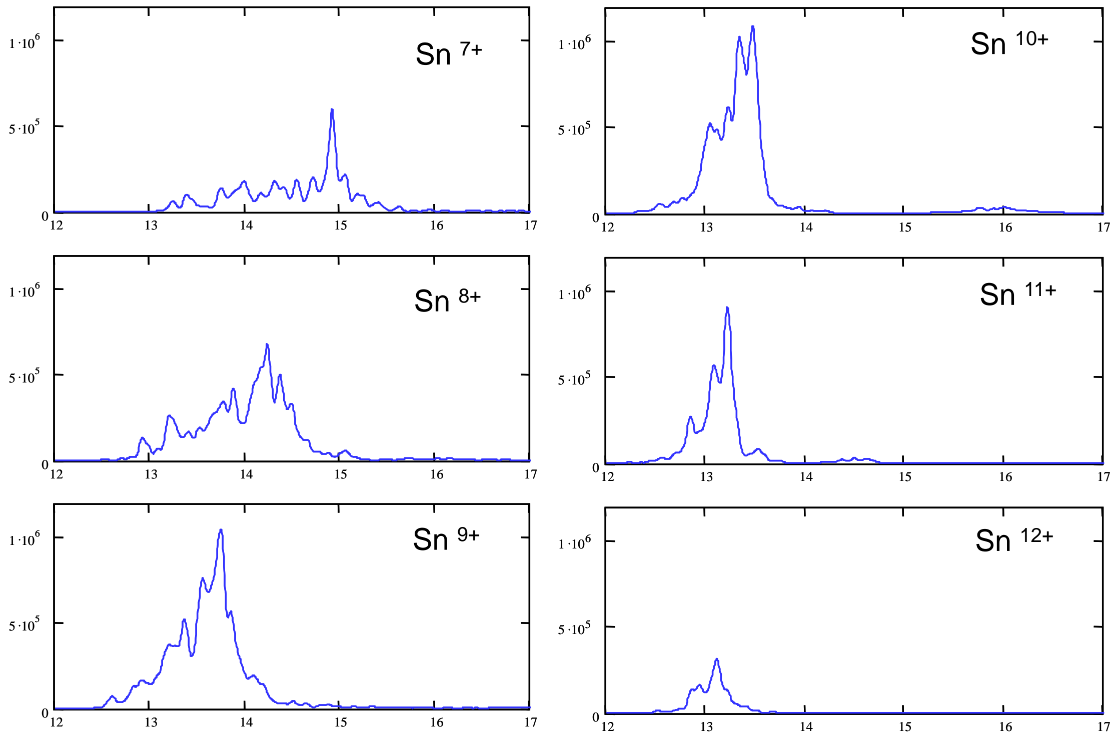

Figure 5.6: COWAN code calculated transition probabilities fitted with a gaussian to generate a spectral distribution for the Sn ions contributing to EUV emission [15, 14]

The gaussian convolved Sn transitions for the various tin ions are shown in fig. 5.6. The region of intense emission shifts toward shorter wavelength for increasing ionization. These results will be compared with experimental spectral results for qualitative determintation of the Sn ion stages producing the EUV emission.

5.3 Experimental Arrangements

The major components in the entire source generation system that includes the laser and vacuum chamber for plasma generation. The instrumentation include a spectrometer and an energy detector for spectral and energy measurements. Details of the experimental set-up, the instrumentation, and the analytical methods used are provided in the following section.

5.3.1 High repetition rate (100Hz) Nd:YAG laser system

The laser used in these studies is a precision, custom built, Q-switched Nd:YAG laser with a master oscillator-power amplification (MOPA) laser system producing a beam at a fundamental wavelength of 1064 nm. The repetition rate is 1 Hz with a pulse duration of 11.5 ns in full width-half maximum (FWHM). The laser beam makes two passes through the first amplifier, followed by a single pass through another two amplifiers (Fig. 5.7).

The laser system, far field beam profile, and the mapping of the focal region are all described in detail elsewhere [16, 15]. In order to control the beam irradiation conditions precisely and accurately, the beam profile needs to be as close to a perfect gaussian shape as possible. The map of the beam focal region provides focal spot diameters for calculating laser irradiance at target. The relationship used to calculate the laser irradiance at target is

$$I = \frac{E}{\tau \cdot A(\pi r^2)} \quad (W/cm^2) \tag{5.4}$$

where E is the input laser energy, τ is the laser pulse duration, and r is the radius of the laser beam on target surface. A minimum beam spot size of $35\mu m$ was measured for the 1 Hz laser with a 100 mm focal length lens. For these experiments, the input laser energies

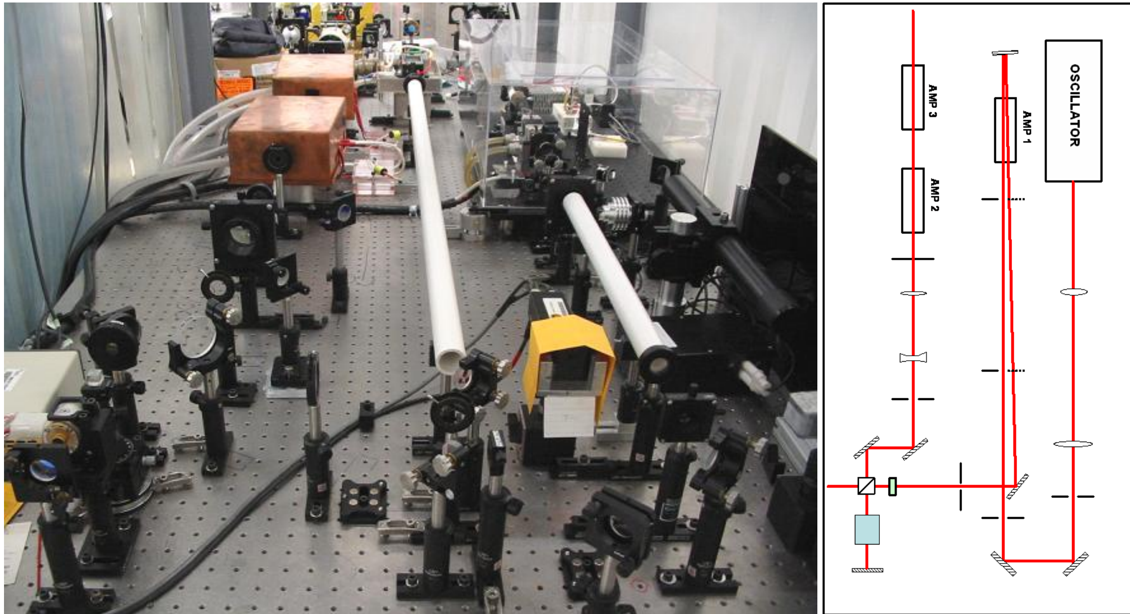

Figure 5.7: 1 Hz laser and a schematic of the optical layout

were selected using a light valve (combination of half-wave plate and a glan-polarizer) and reasonable pulse-to-pulse stability was assumed. The target was moved vertically in order to obtain a fresh surface after each laser shot.

5.3.2 Vacuum Chamber and Set-up

The chamber used for the measurements is a 45 cm diameter, cylindrical vacuum chamber with 12-ports placed with 30° separation angles all around the body. The chamber and operational schematic is shown in Fig. 5.9. The target is positioned at the center of the chamber and the focused laser beam is positioned at 45° angle from normal at the target surface. A lens with focal length of 100 mm which is placed inside the chamber and is used to focus the laser beam. The operating pressure is below 10^{-3} Torr. The EUV energy detector is mounted on the port at 30° angle from the laser beam axis. The flat field grazing incidence

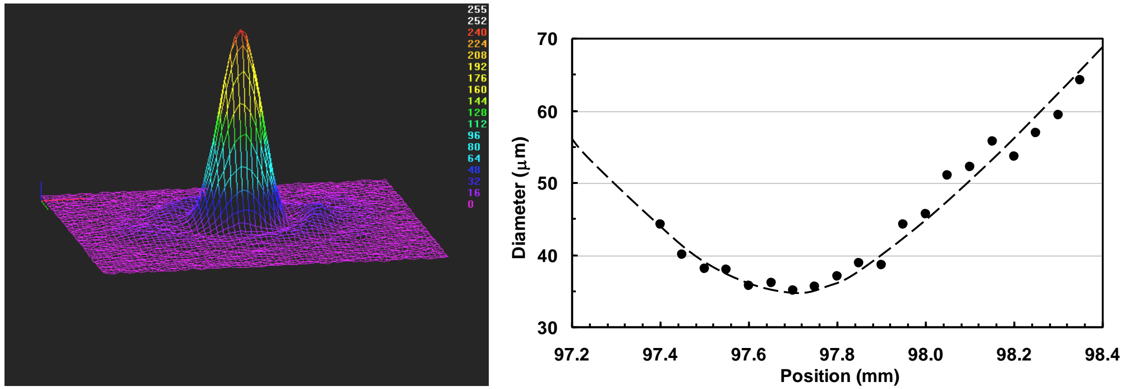

Figure 5.8: Measure far-field beam profile from the 1Hz, 1064 nm laser beam, and the plot of the focal spot region of the 1064 nm beam through a 100 mm lens. The lens is translated in 200 μm steps

spectrometer is located at a 90° angle from the beam axis. The primary instrument used in evaluating EUV emission characteristics of the plasma source is the flat-field spectrometer (FFS).

5.3.3 Flat-Field EUV Spectrometer

The theory of diffraction gratings and vacuum spectroscopic techniques are discussed in detail in many text books. References commonly used by researchers include texts by James Samson [17, 18], Ralph Sawyer [19], and George Harrison et. al. [20].

The idea of combining plane diffraction grating properties with a concave mirror focusing properties was conceived in 1882 by H. A. Rowland. The basis of many vacuum spectrographs in use today utilize the Rowland circle configuration. In this configuration, the concave grating is placed tangentially on a hypothetical circle that has a diameter equal to the radius of curvature of the grating (Fig. 5.10). The center of the grating lies on the

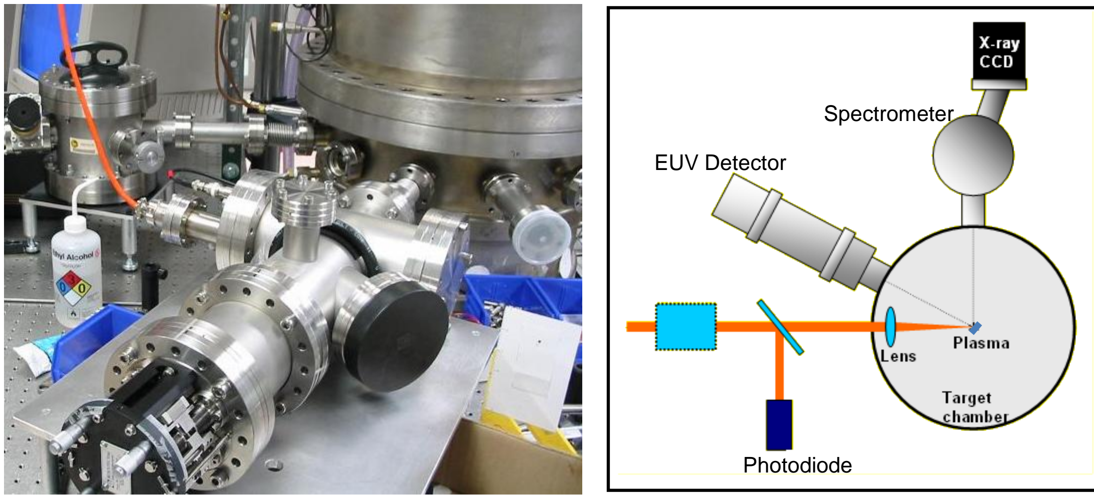

Figure 5.9: Chamber and set-up for planar tin measurements

circumference, and the spectrum of an illuminated slit (I_0) will be focused onto this circle at a point I'. There are several types of mountings available utilizing the Rowland circle. The spectrometer design used for these experiments use a variably spaced, concave grating at grazing incidence for imaging EUV emissions to a charge-coupled device (CCD). A flat detector is used on the Rowland circle to detect the spectral dispersion, and spectrographs that utilize this configuration are labeled flat-field spectrographs/spectrometers (FFS). The variable spacing and curved groove ruling technology [21] eliminates the aberrations inherent to the conventional concave diffraction gratings, thus, enhancing the spectral image focusing properties of these gratings. Details of the geometry and equations for calculating the resolution for a FFS is discussed in detail in references [22, 23, 24].

For this study, the x-ray emission in the 12 nm-18 nm region is investigated thoroughly with a FFS (Fig. 5.11). The concave grating used is obtained from Hitachi [25] and it is a 1200 lines/mm, gold coated, variable spaced reflective grating with a radius of curvature of 5.649 m. The groove spacing varies from 690 nm to 990 nm. The spectrograph is designed

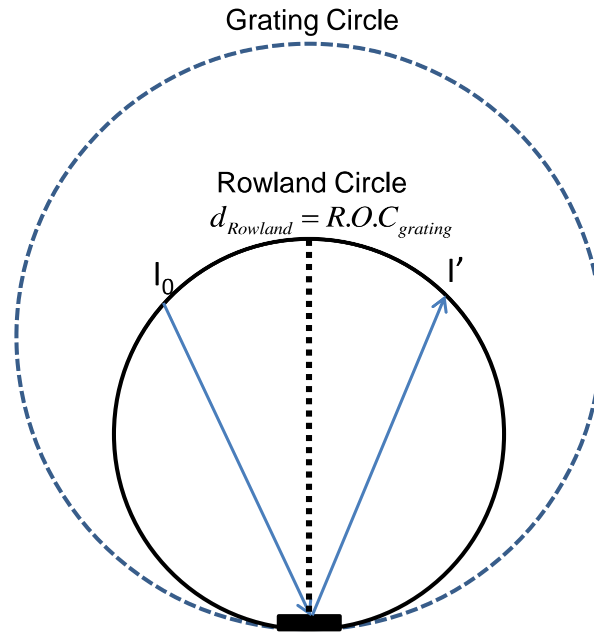

Figure 5.10: Rowland circle

such that the distance from the slit to the grating center is 237 mm and the distance from the grating center to the image plane is 235 mm. The plasma source is collimated onto the grating by an entrance slit and the slit width determines the working spectral resolution of the spectrometer. The angle of incidence of light from the slit to center of the grating is at 87°, and the slit size used is 172 m. The exit angles for a given wavelength, λ, is given as function of distance along the focal plane by

$$m\lambda = \sigma_0(\sin\alpha + \sin\beta) \tag{5.5}$$

where m is the diffraction order, σ is the groove spacing, and α and β are the angles of

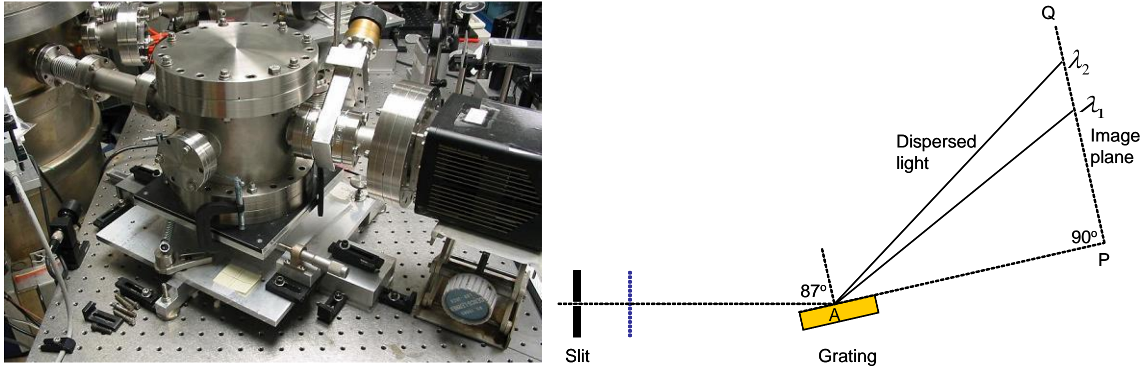

Figure 5.11: Flat-field Spectrometer and design

incidence and diffraction respectively. The resolving power of the spectrometer is given by

$$R = 0.91\frac{m\lambda R_g}{dS} \tag{5.6}$$

where R_g is the radius of curvature of the grating, and S is the slit width. The minimum resolvable wavelength for these set of experiments is calculated to be 0.04 nm.

A 0.5 μm thick Zr filter was used between the slit and the grating in order to filter out any stray light that might reach the image plane. The Zr filter was send to the SURF III synchrotron facility at the National Institute of Standards and Technology (NIST) for obtaining a transmission curve needed for calibrating the spectrometer sensitivity. The first-order diffraction wavelength range is determined to be from 5 nm to greater than 20 nm into a dispersion region of length 25.4 mm. A thinned, back illuminated x-ray CCD camera (PI-SX, Roper Scientific) [26] is used at the dispersion region to record spectra, with the CCD width close to 13 mm selecting a shorter region of the dispersed wavelengths. Diffraction efficiency measurements [22] show that the spatial dispersion in the region of 10 nm - 20 nm is linear on the image plane, thus the diffraction efficiency deconvolution of the spectra is not necessary to determine line ratios. For a number of laser irradiation conditions, a

combination of precision spectroscopy and calibrated 13 nm metrology was implemented to quantify the spectral emission characteristics of the planar Sn target.

5.3.4 Flying Circus EUV Energy Detector

The absolute EUV output energy from the plasma sources needs to be measured in a consistent manner, so that it is repeatable as well as comparable to other results obtained by the global research community. For this purpose, a narrow-bandwidth EUV detector labeled as the *Flying Circus* (Fig. 5.12) by the EUV community, was used [27]. The flying circus (FC) is considered to be the industry standard for EUV energy measurements into the 13.4 nm bandwidth.

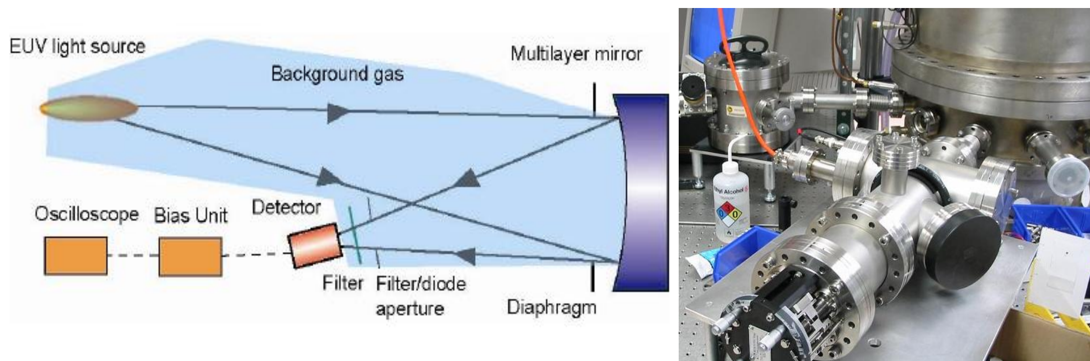

Figure 5.12: The Flying Circus EUV energy detector and the measurement scheme of one of the channels [27]

The major components of the instrument are a curved, normal incidence, Mo/Si multilayer mirror (MLM) that is 25.4 mm in diameter an AXUV-100G photodiode that is radiation hardened to prevent degradation due to energetic wavelength illuminations [28]. The multilayer mirror is used to select the wavelength band at approximately 3%, where

the mirror bandwidth is determined by the d-spacing of the multilayers. The photodiode enables time resolved, and high repetition rate measurements with a spectral responsivity at of 0.24 A/W at 13.5nm determined from the data provided by manufacturer [28]. A 22 V reverse-bias was used with the energy detector for better signal resolution.

The mirror is used in the detector at near normal incidence and the reflected wavelengths from the mirror is focused on to a photodiode surface. Inserted between the MLM and the photodiode is a 0.5 μm thick Zr filter in order to select EUV wavelengths and to eliminate other reflected bands from the mirror since MLMs will reflect visible/IR radiation. The Zr metal filter was purchased from Lebow Inc and its transmission curve was obtained from NIST. The calibration data is plotted in Figure 5.13. The calibration of the Mo-Si multilayer mirror used in the FC shows that it a peak reflectivity of 58% centered at 13.5 nm. In collecting spectra, the lens was translated laterally in 200 μm steps away from the target, and towards the target. During data compilation, the positions notated with positive values indicate that the lens was being translated away from the target surface with the focal region diverging at target surface. All other parameters are kept as constant as possible when scanning across positions. The starting position is labeled to be at zero, thus the position values are rather arbitrary. The intensities are calculated by relating the position to the spot size map obtained for the lens used. The exact method for measuring spot sizes for a lens in described in detail in reference [15].

5.4 Experimental Results

Spectral and energy measurements from planar tin laser plasma was obtained for input laser energies at 70 mJ, 60 mJ, 50 mJ, 40 mJ, 30 mJ, 20 mJ, 15 mJ, 10 mJ, and 5 mJ.

At each energy input a number spectra for the entire focal region of the lens were collected, and spectral measurements were cross calibrated to the FC energy measurements.

5.4.1 Spectral Measurements as a Function of Intensity

The Sn UTA near 13.5nm is a contribution from a multitude of lines arising from the 4d-4f transitions from a number of Sn ion stages. The ions stages contributing to this UTA was determined to range from Sn^{7+} to Sn^{12+}. The plasma electron temperature influences the population of the ion stages created in the plasma. To maximize the CE, it is important to maximize the population of the ionization stages that contribute to the 2%BW of the Mo-Si MLM.

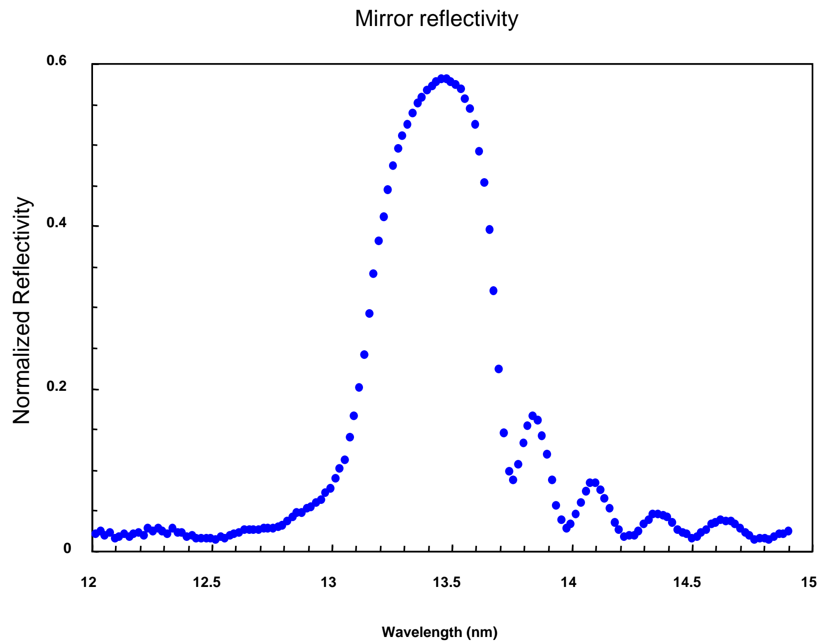

(a) Measured mo-si multilayer mirror reflectivity in the EUV region

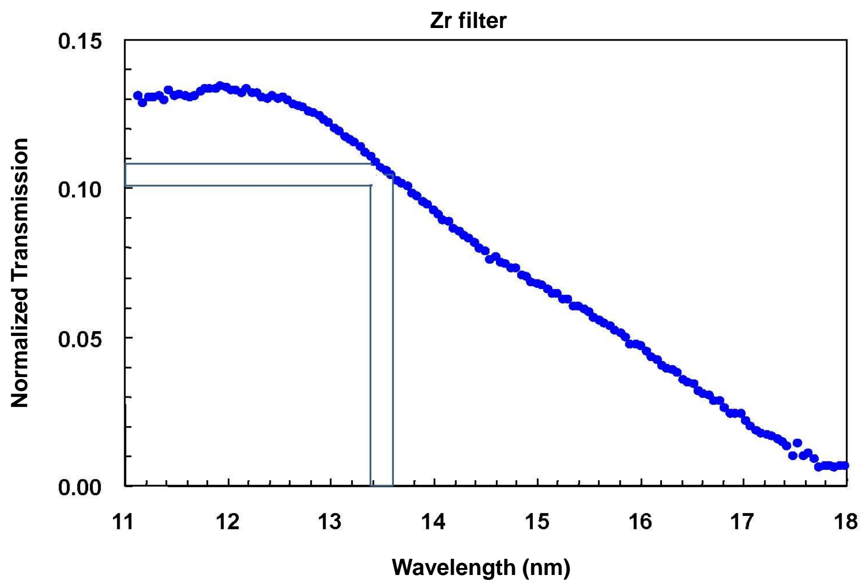

(b) Measured transmission for the 0.5 μm Zr filter

Figure 5.13: Calibration curves obtained from NIST for the EUV detector components

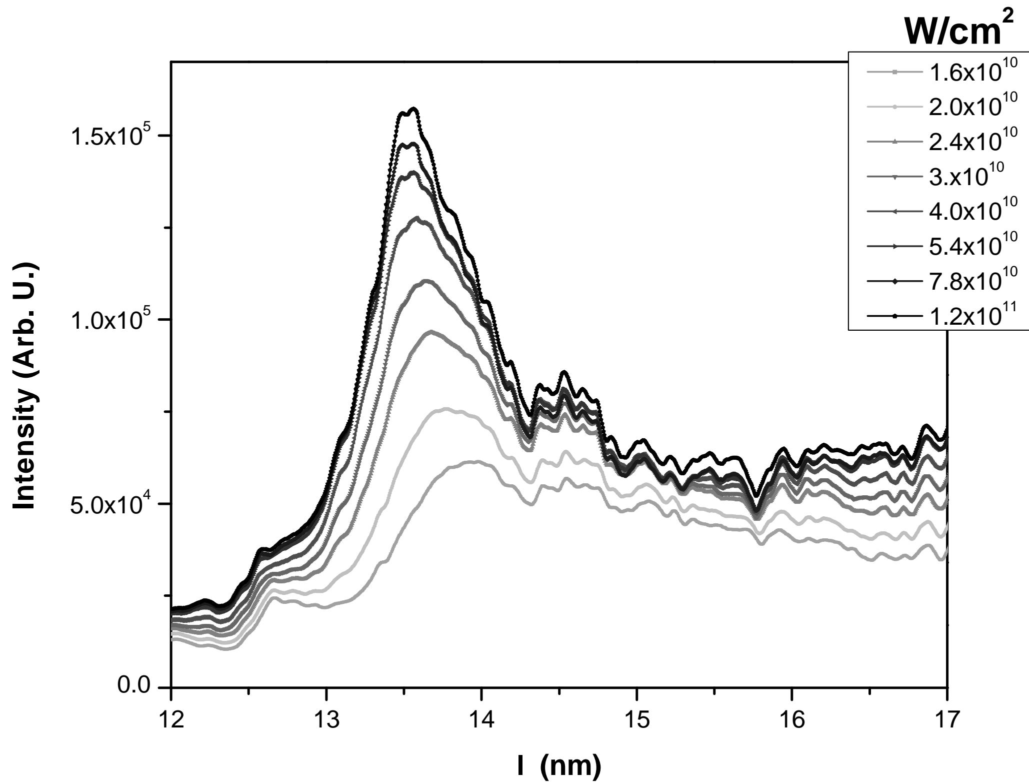

Figure 5.14: Spectral measurements obtained for pplanar Sn target as the intensity is varied by varying the laser beam focal diameter. Maximum counts are observed for an intensity of 1×10^{11} W/cm^2

Figure 5.14 shows corrected spectral data obtained using the FFS. Intensity variation is obtained by varying the laser beam focal width at target. With increasing intensity we observe that the UTA narrows as it grows in height and migrates toward the lower wavelength region. This can be attributed to the higher tin ionization stages becoming populated in the plasma. By optimizing the intensity conditions, we should still see much higher conversion efficiency from this target at 13.5 nm.

To better illustrate the changes in the charge-state distribution in the plasma, the set

of spectra for Fig. 5.15 was normalized with respect to the UTA peak. It is more obvious from here that the lower tin ions populate the plasma at lower intensities giving a flatter distribution. As the higher ionized Sn species become dominant in the plasma, the spectra narrows and emission is concentrated into the region between 13 nm and 14 nm. This compares well to the calculated spectral results where the dominant ion species for high EUV-yield are identified to be Sn^{9+} and Sn^{11+} at average plasma temperatures near 35 eV, as calculated. The trend is the same in all other sets of data where spectral measurements were obtained; thus they are not presented here. If precise control of the plasma temperature and density can be accomplished, then it is obvious from these measurements that the emission bandwidth can be tuned quite accurately.

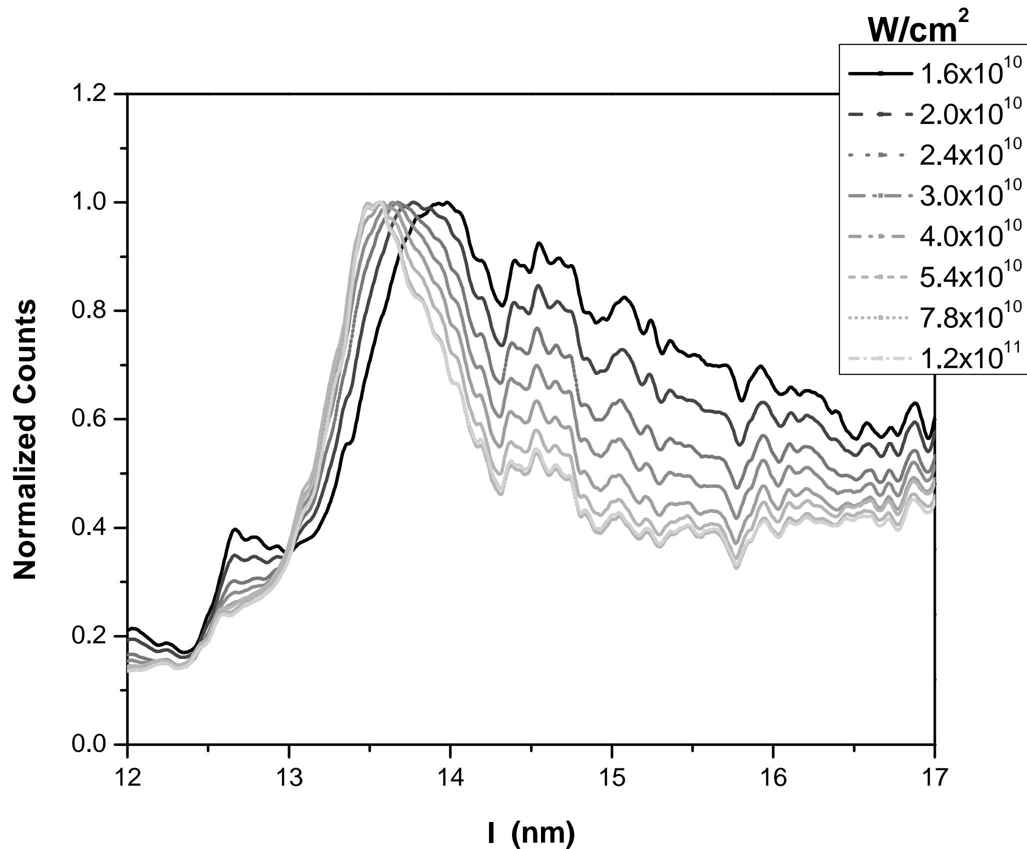

Figure 5.15: The spectra are normalized with respect to the peak emission. The small feature sizes of the spectrum remain at the same position as intensity is increased. The changes predominantly occur in the UTA. The shift to 13.5nm and the narrowing is more obvious here

5.4.2 Conversion Efficiency and Calculation Methods

Measurements of the efficiency of laser energy conversion to EUV light (CE) into the mirror bandwidth is very important in source development. One method is to calculate CE from the output oscilloscope signal from the FC EUV energy detector as described [27, 16].

The EUV energy radiated over 2π steradian solid angle and into the 2% bandwidth of the Mo-Si MLM centered at 13.50nm is obtained by taking into account all components in the energy detector that will have affected final measured signal, giving

$$E_{BW} = \frac{2\pi}{\Omega R_{scope}} \left[\frac{\int_{BW} I_s(\lambda) d\lambda}{\int_{all} I_s(\lambda) T_{gas}(\lambda) R_{mirror}(\lambda) T_{filter}(\lambda) \eta_{diode}(\lambda) d\lambda} \right] A_{scope} \tag{5.7}$$

where Ω is the collection solid angle at the limiting aperture of the detector, A_{scope} is the integrated area under the measured EUV signal, R_{scope} is the impedance of the oscilloscope, T_{gas} is the transmission function of the atmospheric conditions in the chamber, calculated as a function of pressure, R_{mirror} is the reflectivity curve of the MLM, T_{filter} is the transmission of the Zr filter isolating EUV region, η_{diode} is the responsivity of the AXUV photodiode, and $I_s(\lambda)$ is the corrected spectrum obtained during the energy measurement.

The limiting aperture for the FC detector is the mirror diameter, since full aperture of the reflected radiation is focused into the detector. The solid angle is given by

$$\Omega = \frac{1/4\pi D^2_{dmirror}}{L^2} \tag{5.8}$$

calculated for these measurements is is 5.0×10^{-4} Sr, based on a mirror diaphragm $D_d ia$ of 23 mm, and a source to mirror distance, L^2, of 910 mm.

When many energy measurements are needed for a variety of irradiation conditions, the calibration fidelity of the Mo-Si multilayer mirror becomes a concern. Plasma debris on the multilayer surface can degrade the mirror reflectivity. To prevent degradation and in order to keep the reflectivity constant throughout the duration of the experiments, the FFS is used together with the FC for CE compilation. When completing an energy measurement, a spectral measurement was also completed simultaneously for a particular irradiation measurement. The background-corrected spectral measurement is then calibrated against the corresponding energy meausrement. The CE calculated for this particular point is used as

a reference point for other spectral measurements completed for the same experiment. Essentially the FFS becomes a calibrated instrument for measuring CE. Tabulating CE in this method limits the number of times the FC components needs to be exposed to the plasma, thus preserving calibrations. The reasoning behind this method is outlined as follows. The signal from the oscilloscope is assumed to be proportional to the spectral measurement and the reflected and transmitted radiation through the FC components, where

$$A_{scope} \propto \int_{all} I_s(\lambda) T_{gas}(\lambda) R_{mirror}(\lambda) T_{filter}(\lambda) \eta_{diode}(\lambda) d\lambda \tag{5.9}$$

The energy equation, 5.7 can be expressed in terms of the oscilloscope signal A_{scope}, a constant C, and the integrated in-band spectral bandwidth factor, BW_f to be

$$E_{BW} = C A_{scope} BW_f \tag{5.10}$$

A single value for η_{diode} is used in these calculations, then it follows that

$$C = \frac{2\pi}{\Omega R_{scope} \eta_{diode}} \tag{5.11}$$

where C is a constant and

$$BW_f = \frac{\int_{BW} I_s(\lambda) d\lambda}{\int_{all} I_s(\lambda) T_{gas}(\lambda) R_{mirror}(\lambda) T_{filter}(\lambda) d\lambda} \tag{5.12}$$

By introducing a spectrometer calibration coefficient, C_s, we define,

$$C \cdot A_{scope} = C_s \int_{all} I_s(\lambda) T_{gas}(\lambda) R_{mirror}(\lambda) T_{filter}(\lambda) \eta_{diode}(\lambda) d\lambda \tag{5.13}$$

and by making the appropriate substitutions, the in-band EUV energy is obtained as

$$E_{BW} = C_s \int_{BW} I_s(\lambda) d\lambda \tag{5.14}$$

giving an energy value for the spectral counts in 2π sr x $2\% BW$ at 13.5nm. The method outlines assumes isotropic emission from the source and the limits of integration for the 2%

BW centered at 13.50nm are from 13.365nm to 13.635nm. CE values are given as "percent CE at 2πSr and 2%BW at 13.5nm" as a standard in literature. The CE is the ratio of the calculated in-band EUV energy, $E_{BW,ref}$, to the laser energy at target, $E_{L,ref}$, and for a given reference measurement is,

$$CE_{ref} = \frac{E_{BW,ref}}{E_{L,ref}} \times 100\% \frac{C_s \int_{BW} I_{s,ref}(\lambda)d\lambda}{E_{L,ref}} \tag{5.15}$$

Then, for any spectral measurement obtained obtained using FFS where a reference was collected, the EUV energy is given by

$$E_{BW,i} = C_s \int_{BW} I_{s,i}(\lambda)d\lambda \tag{5.16}$$

and the CE_i can be calculated by solving for the constant,

$$CE_i = \left(\frac{I_{s,i}(\lambda)d\lambda}{I_{s,ref}(\lambda)d\lambda}\right)\left(\frac{E_{L,ref}}{E_{L,i}}\right) CE_{ref} \tag{5.17}$$

All CE calculations discussed in this chapter and in the rest of the thesis will be calculated using the method discussed.

CE as a Function of Irradiance Intensity

The CEs tabulated for each set of measurements were analyzed in two ways. First, calculated CE is plotted with respect to lens focus position (Fig. 5.16a). The separation distance between the target position and the minimum focus position of the laser beam was varied by translating the focusing lens along the laser axis. The position scan was made from one side of the focus to the other side, passing the minimum focus. Translation step size used was 200 μm, and at each step, a spectral measurement was obtained. Each CE value is an average over 20 laser shots. The highest conversion efficiency calculated for these

experiments is 4.889 % for the laser energy at 70mJ and the corresponding laser power density calculated to be near 1.2 $\times$ 10^{11}W/cm^2 (Fig. 5.16b). A minimum is observed in (Fig. 5.16a) which is the measurement for the narrowest region of the focal plane irradiating the target.The dip in CE measurements are minimum focus was observed in other data sets from this measurement series down to 30mJ. Below this laser energy input, the CE distribution follows measured spot size distribution of the lens, with the maximum CE found at the smallest focus. Two explanations can be offered for this. One possibility may be that at high laser energies, the intensity is too high at the minimum focus and charge-state populations in the plasma is at higher ionization states, thus reducing emission into the 13.5 nm region. The other contributing factor maybe the plasma size, where it is smaller than the 80 μ laser beam diameter for which the highest EUV energy was found. Comparing measurements for the same spot diameters from the various data sets as a function of intensity does not provide any conclusive information. A more careful study is needed.

CE as a Function of Laser Energy

The CE maximum measured for each laser energy data set was plotted against the corresponding laser energy and this is given in Fig. 5.17. The plot shows increase in CE, but shows signs of saturating at even higher energies. It was not possible to extract higher energies from this laser in the far-field region while conducting measurements, thus limiting further exploration of the trends in CE and laser energy.

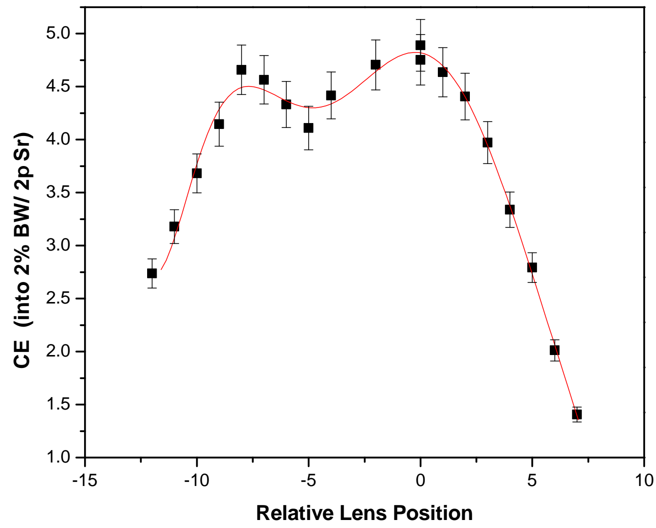

(a) Conversion efficiency as a function of lens focus

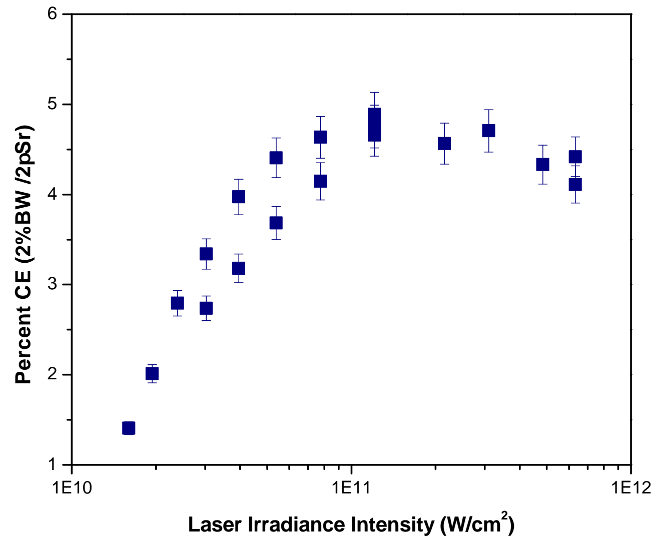

(b) Smae CE plotted as a function of intensity

Figure 5.16: Intensity and lens spot size dependencies of measured conversion efficiency for 13.5 nm

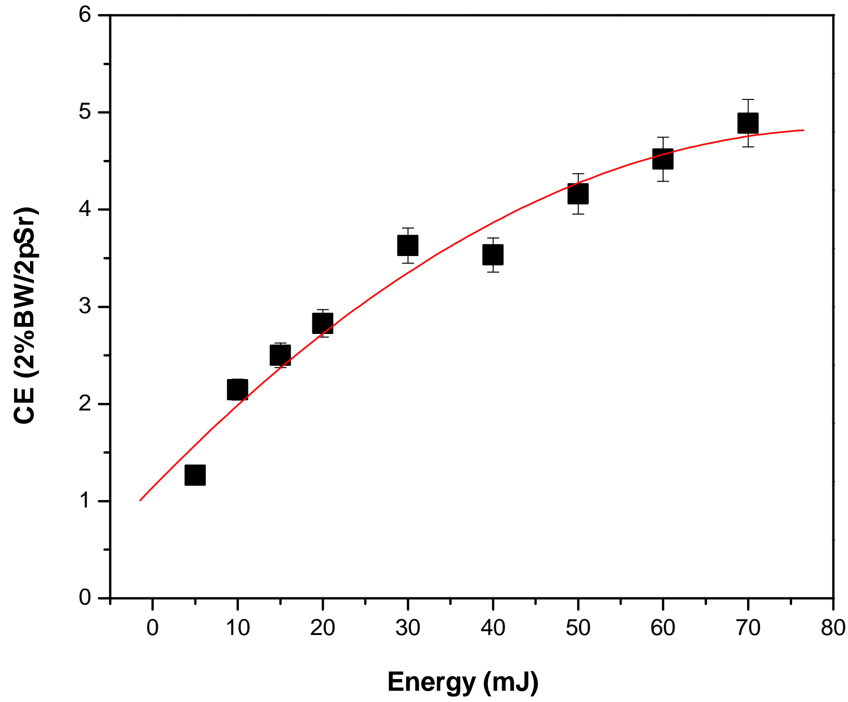

Figure 5.17: Conversion efficiency as a function of laser energy

5.5 Discussion

The major assumption used in the CE calculation is isotropic emission from the source. Studies have shown that this is not the case in planar targets, and that the emission is highly directional in laser plasmas generated from planar geometries. Angular distribution measurements by other groups have shown CE scaling by $\cos^2\theta$. Angular distribution measurements are not completed for this set of data due to limitations in the experimental configurations. Future experiments in a chamber with the capability for conducting measurements for energy as well as debris distribution are being planned. Although, solid tin

allows for high conversion, debris mitigation studies show this material to be unsuitable as a viable EUV light source [5].

5.6 Summary

Studies of Solid Sn laser produced plasma are conducted, using a Nd:YAG, Q-switched, 1064 nm, 1 kHz laser, with a pulse length of 11.5 ns. Spectral data was collected using a high resolution Flat-Field Grazing Incidence Spectrometer coupled to an x-ray CCD, and recorded as a function of varying laser input energy, varying laser spot size, and analyzed as a function of intensity. An EUV diagnostic specially constructed for calibrated measurements of EUV emission was used in determining CE at 13.5 nm. The highest, calibrated conversion efficiency measured to date at 4.889% is reported. Simulations of the experimental conditions were completed using MED 103 which is 1D-Lagrangian hydrodynamic code for insights into the plasma dynamics. COWAN code was used in predicting the atomic transitions.

5.7 References

[1] David J. Nagel, Charles M. Brown, M. C. Peckerar, Marshall L. Ginter, J. A. Robinson, Thomas J. McIlrath, and P. K. Carroll. Repetitively pulsed-plasma soft x-ray source. *Appl. Opt.*, 23(9):1428, 1984.

[2] R. C. Spitzer, T. J. Orzechowski, D. W. Phillion, R. L. Kauffman, and C. Cerjan. Conversion efficiencies from laser-produced plasmas in the extreme ultraviolet regime. *Journal of Applied Physics*, 79(5):2251–2258, 1996.

[3] Winnie Svendsen and Gerard O'Sullivan. Statistics and characteristics of xuv transition arrays from laser-produced plasmas of the elements tin through iodine. *Phys. Rev. A*, 50(5):3710–3718, Nov 1994.

[4] Banqiu Wu and Ajay Kumar. Extreme ultraviolet lithography: A review. *Journal of Vacuum Science and Technology B: Microelectronics and Nanometer Structures*, 25(6):1743–1761, 2007.

[5] Kazutoshi Takenoshita. *Debris characterization and mitigation of droplet laser plasma sources for EUV lithography.* PhD thesis, University of Central Florida, Department of Electrical Enigineering and Computer Engineering, 2006.

[6] Donna J. O'Connell. Characterization of a lithium laser produced plasma at 135 å for extreme ultraviolet projection lithography. Master's thesis, University of Central Florida, CREOL & FPCE: The College of Optics and Photonics, 1994.

[7] Marc A. Klosner. *Intense capillary dischrge plasma extreme-ultraviolet sources for EUV lithography and other EUV imaging applications.* PhD thesis, University of Central Florida, CREOL & FPCE: The College of Optics and Photonics, 1998.

[8] Gerry O'Sullivan. Modelling euv atomic emission from xe and sn plasmas with available atomic structure and plasma codes. Presentation at EUVL Source Modelling Workshop, Antwerp, Sept. 28th 2003.

[9] A. Djaoui. *A User Guide for the Laser-Plasma Simulation Code: MED103.* The Central Laboratory of the Research Councils, Rutheford Appleton Laboratory, Oxfordshire, 1996. Technical Report RAL-TR-96-099.

[10] Robert D. Cowan. *The Theory of Atomic Structure and Spectra.* University of California Press, Berkeley, first edition, 1981.

[11] Alexander Kramida. Cowan code package for atomic physics. Technical report, http://das101.isan.troitsk.ru/cowan.htm.

[12] M. Al-Rabban. Term structure of 4d-electron configurations and calculated spectrum in sn-isonuclear sequence. *J. Quant. Spec. and Rad. Trans.*, 97:278–316, 2006.

[13] Moza Al-Rabban, Christian Keyser, Simi George, Howard Scott, Vivek Bakshi, and Martin Richardson. Radiation transport modeling for xe and sn-doped droplet laser-plasma sources. volume 5751, pages 769–778. SPIE, 2005.

[14] Harvey Elliot White. *Introduction to Atomic Spectra.* McGraw-Hill Book Company, New York, first edition, 1934.

[15] Chiew-Seng Koay. *Radiation studies of the tin-doped microscopic droplet laser plasma light source specific to EUV lithography.* PhD thesis, University of Central Florida, CREOL & FPCE: The College of Optics and Photonics, 2005.

[16] Scott Mackay, editor. *High conversion efficiency microscopic tin-doped droplet target laser-plasma source for EUVL*, volume 5751 of *Proc. SPIE*, 2005.

[17] James A. R. Samson. *Techniques of Vacuum Ultraviolet Spectrosocpy.* John Wiley and Sons, Inc., New York, first edition, 1967.

[18] James A. Samson and David L. Ederer. *Vacuum Ultraviolet Spectroscopy I.* Academic Press, San Diego, 1972.

[19] Ralph A. Sawyer. *Experimental Spectroscopy.* Prentice-Hall, Inc., New York, second edition, 1951.

[20] George R. Harrison, Richard C. Lord, and John R. Loofbourow. *Practical Spectroscopy.* Prentice-Hall, Inc., New Jersey, 1948.

[21] Tatsuo Harada and Toshiaki Kita. Mechanically ruled aberration-corrected concave gratings. *Appl. Opt.*, 19(23):3987–, 1980.

[22] W. Schwanda, K. Eidmann, and M. C. Richardson. Characterization of a flat-field grazing-incidence xuv spectrometer. *Journal of X-Ray Science and Technology*, 4(1):8–17, 1993.

[23] T. Kita, T. Harada, N. Nakano, and H. Kuroda. Mechanically ruled aberration-corrected concave gratings for a flat-field grazing-incidence spectrograph. *Appl. Opt.*, 22(4):512, 1983.

[24] Christian Keyser. *Optical and spectral characterization of the water droplet laser plasma EUV source.* PhD thesis, University of Central Florida, Department of Physics, 1994.

[25] Hitachi aberration corrected concave gratings for flat-filed spectrographs. Technical report, `http://www.hitachi-hta.com/media/ConcaveGrating-Spectrograph-Grazing(1).pdf`, 2005.

[26] X-ray cameras. Technical report, `http://www.piacton.com/products/xraycam/pisx/default.aspx`, 2007.

[27] R. Stuik, F. Scholze, J. Tummler, and F. Bijkerk. Absolute calibration of a multilayer-based xuv diagnostic. *Nucl. Instrum. Methods*, 492:305–316, 2002.

[28] International radiation detectors inc. axuv photodiodes operating principles. Technical report, http://www.ird-inc.com/axuvope.html, 2007.

CHAPTER 6

EUV GENERATION FROM SOLID TIN AND SOLID LITHIUM: A COMPARISON

6.1 Introduction

Laser plasmas are compact, intense light sources that are advantageous due to power scalability, high repetition rates thus greater dose stability, small source size with large solid angle for collection, and energy stability. Few materials are efficient emitters of 13.5 nm radiation. Currently three sources are being favored for generating this bandwidth and these are xenon, tin, and lithium. Of these, tin and lithium targets are expected to produce the output power levels needed.

Hydrogen-like line emission from lithium has long been considered a candidate for a EUV light source for lithography, as well as photoelectron spectroscopy (PEEM). Early laser-plasma experiments with lithium foil showed promising results [1], and lithium was also tried as a medium in discharge plasmas [2]. Recently the leading industrial light source supplier, Cymer, has chosen lithium LPP as the primary EUV source to use with their excimer laser systems for high volume manufacturing (HVM). An intense, single transition line from doubly ionized lithium exactly at 13.5 nm is observed and reported in previous works [**?** **?** 3]. Many groups around the world are working on improving emission level of lithium into 13.5 nm for both discharge, and laser plasma schemes [**?** **?**].

In this chapter, the potential of lithium as a laser-plasma source is investigated both theoretically and experimentally. A direct comparison of EUV emission from tin and lithium

planar solid targets for a variety of experimental parameters are presented. Through detailed spectroscopic studies, optimum EUV emission conditions is isolated for both targets and compared.

6.2 Plasma Generation

Focused laser radiation on target surface creates hot-dense plasma with temperatures sufficient enough to produce emission in the soft x-ray region of the electromagnetic spectrum. Laser plasma emission characteristics are directly dependent on the plasma temperature and density resulting from the laser beam interaction with the target surface. Laser wavelength, target material, and geometry are parameters that affect the plasma density, due to the variations in optical coupling efficiency. Plasma temperature and density vary in time and distance, as well. Optimizing emission from plasmas to a specific wavelength means isolating temperature and density condition ideal for that emission, which can be achieved using spectroscopy. For temperature and density calculations from the spectroscopic quantities, few assumptions are made about the laser plasmas. For low-Z lithium plasma, analysis can be simplified by assuming optically thin plasma, isotropy of emission, and the existence of local thermodynamic equilibrium (LTE). At high enough densities ($> 10^{18}$ cm^{-3}) conditions for LTE are valid, plasma temperatures can be calculated quite accurately for line emission from lithium, assuming that the plasma density is known. In a plasma with H-like emission, where all the transitions are to the ground state (Lyman series), the Inglis-Teller limit for last distinguishable transition can be applied to estimate the electron density. A transition from a higher state, n_i, to the ground state will be resolvable if the electron density, n_e, is

[4, 2]

$$n_e \leq \frac{Z^{9/2}}{120a_0^3}\left(\frac{1}{n_i^2} - \frac{1}{(n_i^2+1)^2}\right)^{3/2}(n_i^2-1)^{-3/2} \tag{6.1}$$

where Z is the atomic number of the plasma source, and a_0 is the Bohr radius in appropriate units. Once the electron density is known, an estimate of the electron temperature can be obtained using ratio of intensities of emission lines originating from consecutive ionization stages as follows.

$$\frac{I'}{I} = \frac{f'g'\lambda^3}{fg\lambda'^3}(4\pi^{3/2}a_0^3 n_e)^{-1}\left(\frac{kT}{E_H}\right)^{3/2}\exp\left[-\frac{E' + E_\infty - E_H - \Delta E_\infty}{kT}\right] \tag{6.2}$$

Primes notate transition line parameters from the higher ionization stage; ΔE_∞ is the reduction of the ionization energy, E_∞, of the lower ionization stage, and E_H is the ionization potential of hydrogen at 13.6 eV. For an emission spectrum with unresolved transition arrays as in the case of tin, brute force calculations are not practical for temperature calculations and sophisticated numerical schemes are used.

6.3 Experimental Arrangements

Studies conducted for this chapter are completed with a different set-up than the one described in the previous chapter (5). Main features of the set-up in contrast to the previous set of measurements will be discussed in the following sections.

6.3.1 Laser

The laser used in the studies is a commercially available, Q-switched, Nd:YAG system from Quantel, that can be operated at 10 Hz, 5 Hz, or 2 Hz. The maximum attainable energy

of approximately 200 mJ per pulse. The far-field profile of the laser beam is shown in Fig. 6.1. As in the case of previous experiments, the laser wavelength used was 1064 nm with a

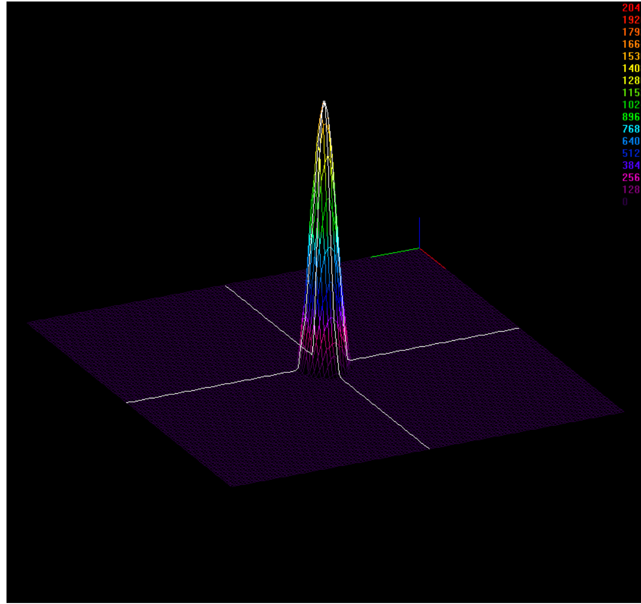

Figure 6.1: Measured far-field laser beam profile for the 10 Hz laser

pulse duration (FWHM) of 10.5 ns and a beam diameter at 9 mm. The beam was focused using a 50 mm diameter, anti-reflection coated, 100 mm focal length plano-convex lens onto the sample surface in p-polarization at an angle of 45. A detailed map of the focal region was obtained by imaging the beam focus with a 10X microscope objective on to a Spiricon SP980M CCD camera (Fig. 6.2). Thus laser irradiation intensity at target for a given spectral measurement can be calculated. Minimum spot size achieved was 30 μm within error limits, and the lens was translated to vary the spot size, changing the peak intensity. Background gas pressure below 4×10^{-6} Torr was maintained during experiments.

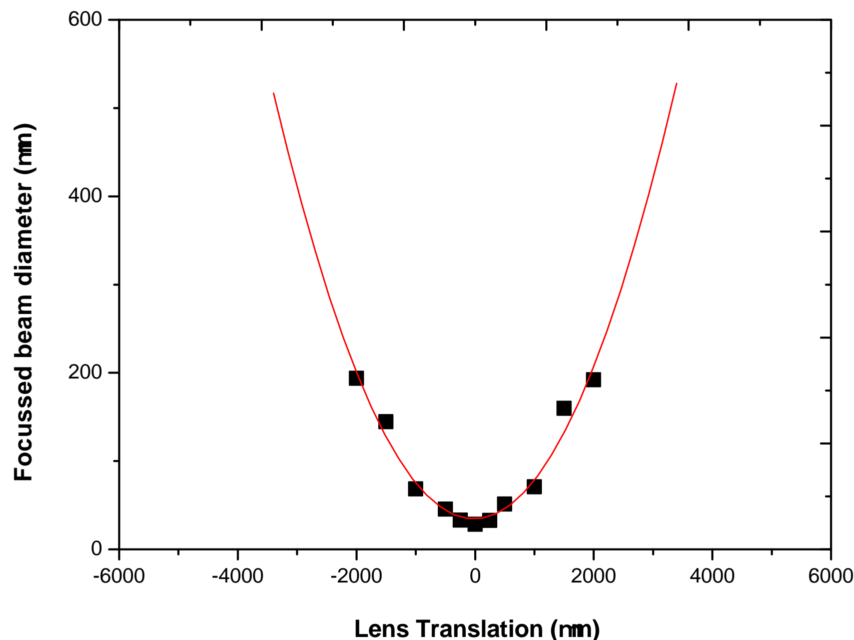

Figure 6.2: Measured focal range of the lens used in the experiments used for calculating irradiances

6.3.2 Chamber and Instrumentation

The chamber used for the studies is 33 cm in diameter, 18 cm in height, with eight ports separated by 45, and eight 1/2 inch NPT feedthroughs. The experimental set-up and chamber are shown in Fig. 6.3. The EUV detector is placed at a 45° angle with respect to the laser beam axis and normal to the smaple surfaces. The FFS spectrometer is at a 90° angle with respect to the laser axis.

High resolution spectra were collected using a flat-field grazing incidence reflection grating spectrograph (FFS). The principles of this spectrometer is described in detail in chapter 5. This spectrometer has a fixed entrance slit of approximately 200 μm, and a variably spaced 1200 lines/mm curved grating with wavelength imaging range of 5 nm to 20

nm. Digital spectral images are obtained using micro-channel plates in chevron configuration, fiber optically coupled coupled to a Photometric 300 series, 1024 x 1024, 24 μm pixel, cooled spectroscopic CCD [2]. During experiments the laser was operated at 2 Hz, and the energy per pulse is selected by changing flashlamp voltage. A shutter was used to obtain single shot spectra. The target surface was also translated parallel to itself in order to obtain a fresh surface for each measurement. Tin and lithium were both used in a single target mount, in order to switch between metals without pause or vacuum venting.

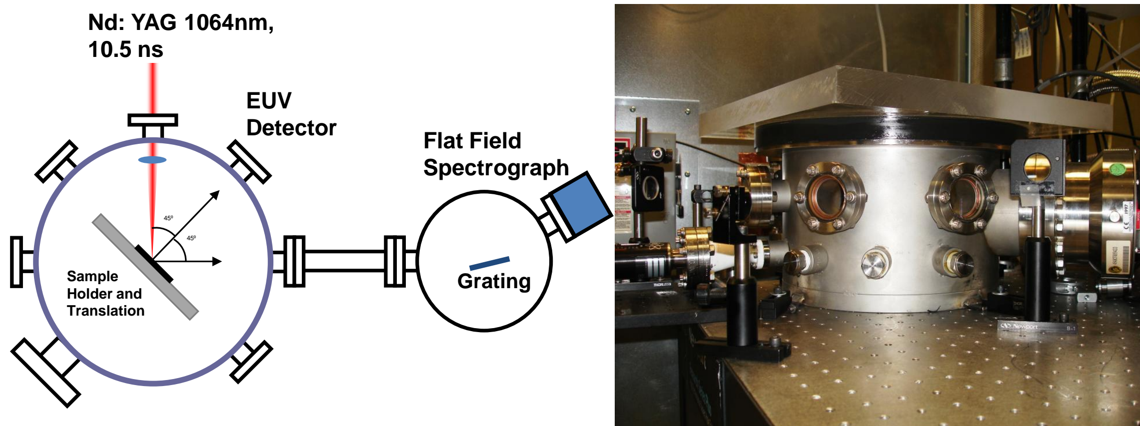

Figure 6.3: Experimental configuration of the chamber and instrumentation

To measure the EUV energy, a 22 V biased AXUV-100G diode with an efficiency of 0.24 A/W was used in combination with a 45 Mo/Si MLM and a 0.5 μm Zr filter. Reflectivity of the MLM and transmission of the Zr filter was calibrated by the National Institute of Standards and Technology (NIST). The EUV detector was placed inside the chamber and aligned normal to the target surface. The limiting aperture is the diameter of the Zr filter diaphragm mount which is approximately 7.1 mm located after the MLM. The distance of the filter mount is 120 mm from the plasma source resulting in a collecting solid angle of

2.75×10^{-3} Sr. This detector was calibrated against the Flying Circus [5] EUV diagnostic instrument with calibrated optics and a solid angle of 5.0×10^{-4} Sr in order to ensure proper accounting of EUV energy. Description of the EUV measurements, calibration methods, and method for calculating CE are presented in detail in the previous chapter 5.

Debris measurements for particle detection using mirror witness plates placed normal to the target surface 20 cm away from the plasma were conducted for both Li and Sn. The witness plates used are pieced Si wafers, which can be interchanged during an experiment without having to bring main chamber up to atmosphere. The samples were then analyzed using Optical Microscopy.

6.4 Experimental Results

For each input laser energy, many spectral measurements are obtained at different beam focal diameters. At the start of the focal scan, the minimum focus of the lens was placed well away from the target surface, and scan was completed by translating the lens toward the target surface in 200 μm steps.

6.4.1 Spectral Measurements as a Function of Intensity

Over twenty spectra were collected for a given input laser energy as a function of intensity for both targets in order to identify optimum emission temperature of the plasma. Spectra as a function of intensity for Li solid target at an input laser energy per pulse of 65.5 mJ, is shown in Fig.6.4. The emission lines from the He-like transitions of Li^{+}(1s-2p), Li^{+}(1s-3p), and Li^{+}(1s-4p) can found at 19.9 nm, 17.8, and 17.2 respectively. H-like transitions of Li^{2+}(1s-2p) at 13.5 nm, Li^{2+}(1s-3p) at 11.39 nm, and Li^{2+}(1s-4p) at 10.8 nm are also identified in the measured spectra. Variations of the line emission with increasing

intensity (counts) of the Li^{2+} transitions as the laser irradiance intensity is increased is clearly observed.

The most intense of these emission lines is the Li^{2+}(1s-2p) at 13.5 nm, which is produced at plasma temperatures greater than 10 eV. The emission at 13.5 nm was found to be optimum for the intensity region of $1-5\times10^{11}$ W/cm^2. The strongest 13.5 nm transition line is found to be near an intensity of 2.2×10^{11} W/cm^2, for the data set shown.

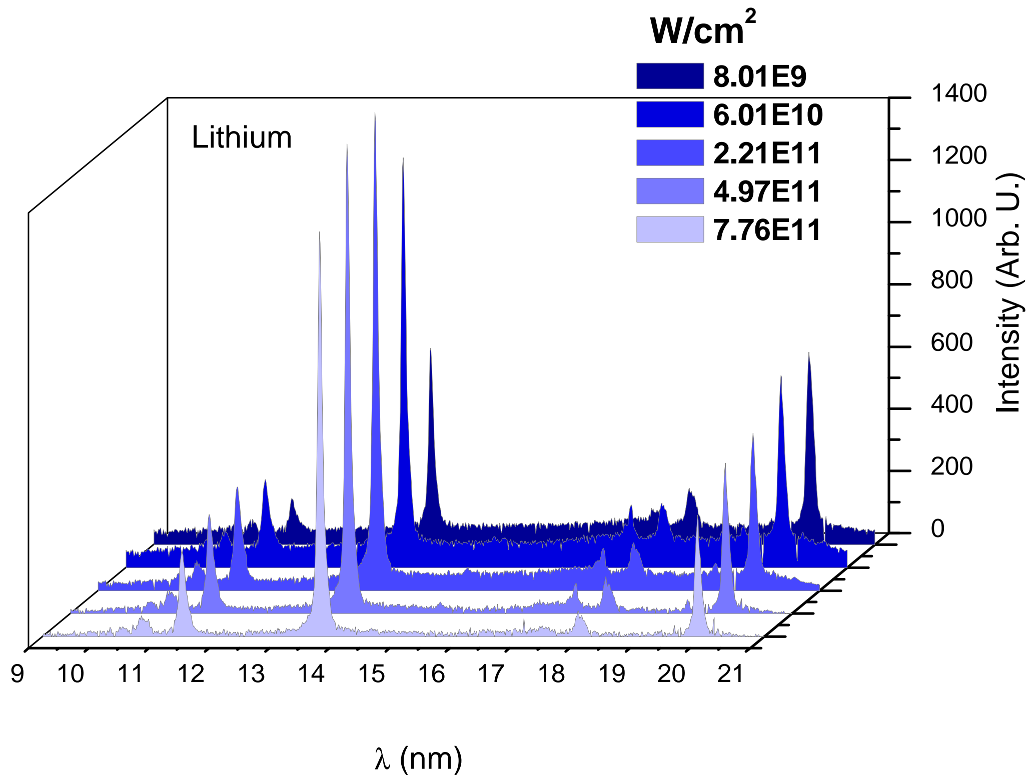

Figure 6.4: Spectrum from a planar lithium laser plasma source in the EUV region as function of laser intensity

For lithium, the last resolvable transition before quasi-continuum is the Li^{2+} (1s-5p) at 10.5 nm. Based on the Inglis-Teller limit, an estimate of the upper-bound on plasma

electron density in the EUV emitting region is taken as 9.0×10^{19} cm^{-3} for the measurements. The average plasma temperature calculated using the ratios of observed line intensities of successive ionization stages, and the above electron density, is approximately 14 eV. This method of evaluation is presented in much more detail in reference [1]. This temperature estimation is valid if the transition levels are in local thermodynamic equilibrium with higher quantum levels, an assumption that is appropriate for the plasma region close to the target surface. If the estimated electron densities were an order of magnitude higher, then the temperature estimated will be closer to 17 eV for lithium plasmas studied here.

Tin spectra (Fig. 6.5)show the expected unresolved transition array (UTA) emission band originating from the Sn^{7+} to Sn^{12+} ions with the ground configuration $[Kr]4p^6 4d^n$, where n = 2 to 7. The thousands of tin emission lines in the spectral region around 13.5 nm originate from transitions between the excited configurations, $4p^5\,4d^{n+1}$ and $4p^6\,4d^{n-1}\,4f^1$. Maximum emission at 13.5 nm is found to be at intensities in the region of $1 - 2 \times 10^{11}$ W/cm^2 with a plasma temperature of about 30 eV obtained from numerical simulations.

Both tin and lithium data sets show similar behavior, where the emission into 13.5 nm decreases with higher than optimum intensity. Research on droplet plasmas that will be presented in the next chapter (Chap. 7 has shown that tin emission into the 13.5 nm is strongest in the intensity region of $1 - 2 \times 10^{11}$ W/cm^2. The spectral data also show that the lithium line emission is almost twice as intense in counts as the tin UTA at 13.5 nm.

6.4.2 CE as a function of laser irradiance intensity

Calibrated CE measurements were completed for each spectral measurement thus providing a detailed map of the EUV emission with respect to intensity for both Sn and Li

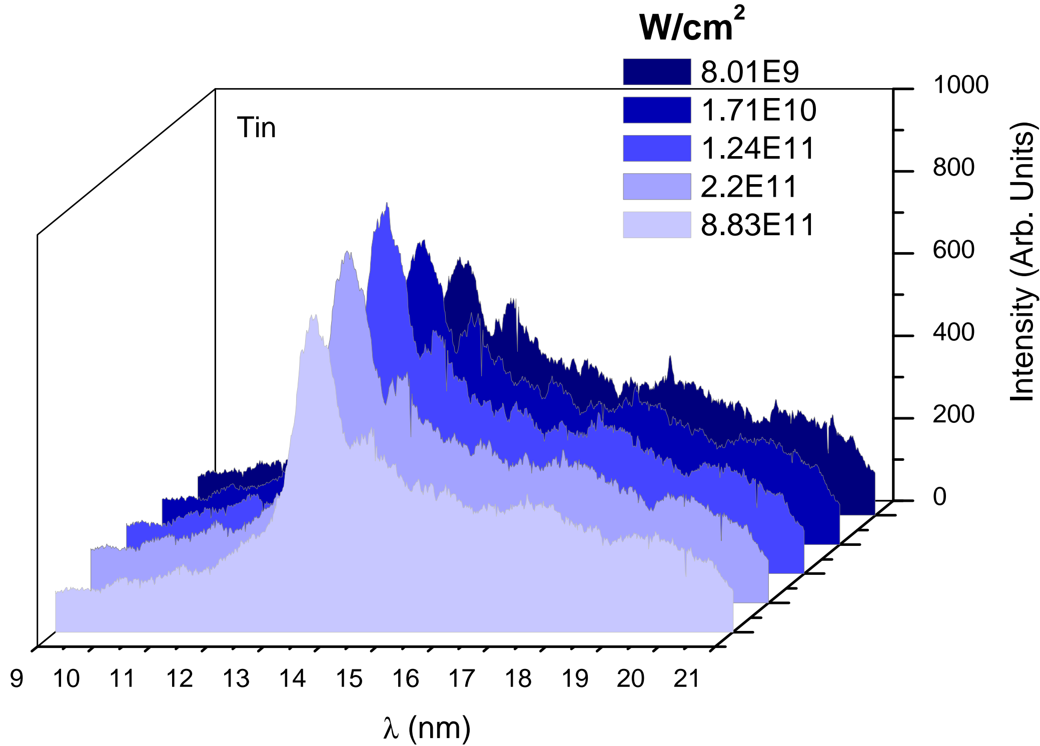

Figure 6.5: Spectra from the planar tin laser plasma source in the EUV region

(Fig. 6.6). Transmission through the background gas was neglected, since EUV absorption is minimal at the background pressure conditions used. Results of the initial experiments were previously published [6], with 2.1% CE from lithium near 1.6×10^{11} W/cm^2, and 4.0% from tin near 1.2×10^{11} W/cm^2.

The maximum CE measured since the initial publication is 2.2% in lithium at an intensity of 6.6×10^{10} W/cm^2. For tin, the highest CE obtained is 4.9% at laser intensities near 9.2×10^{10} W/cm^2. The small scatter in the CE data is attributable to the target surface roughness on the sub-100 μm scale. This data is published in optics letters [7]. It is observed that the conversion efficiency increases with increasing laser intensity. This was

also observed in the measurements completed in the previous chapter (5). At the same time the irradiance at which the high CE is found for each laser energy is similar, while the beam spot diameter increases with increasing laser energy for high conversion. Basically, as the laser energy is increased, the optimum intensity is found for larger plasma sizes, and this is important in source size consideration. Methods for increasing CE without changing the plasma source size needs to be investigated.

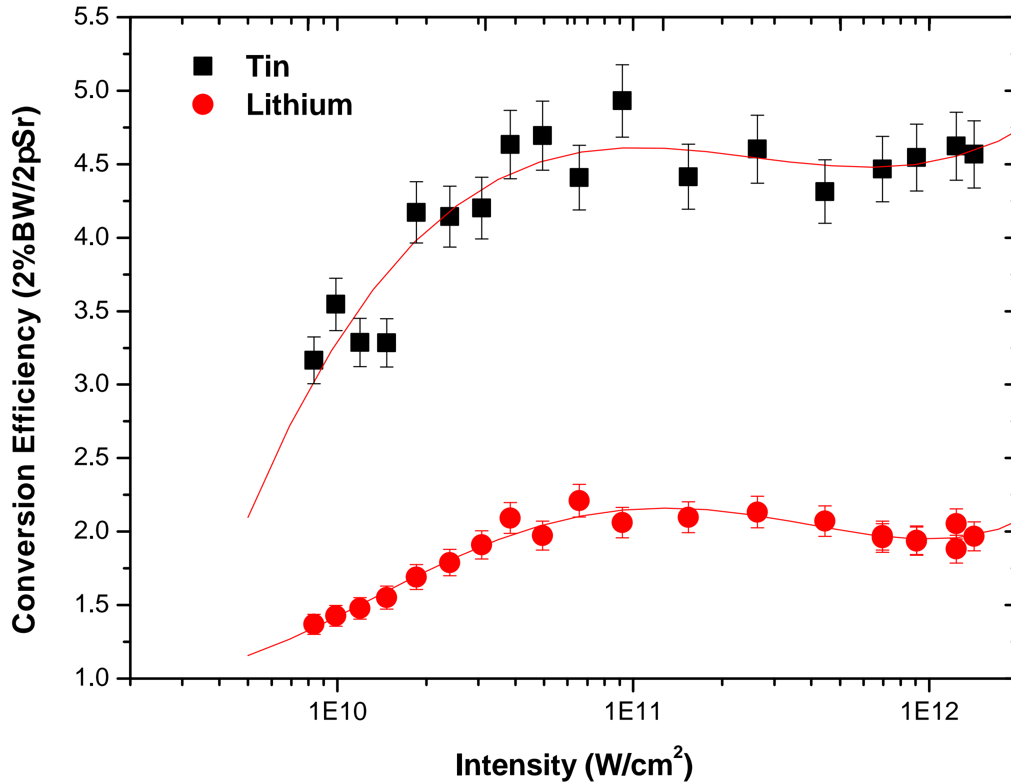

Figure 6.6: Highest conversion efficiencies measured for both planar tin and lithium targets

6.4.3 Debris studies

Witness plate tests for debris were completed at 20 cm from the source for a total of 1000 laser shots for both Li and Sn, at an intensity of 1×10^{11} W/cm^2. The debris from these two targets impact the sample surface in different ways (Fig. 6.7). The lighter lithium ions with higher velocity shatter the mirror surface upon impact, while the tin ions mostly deposit on the surface. The lithium deposits were smaller in size than the tin particles on the mirror surface. Analysis of the witness plate for lithium show a spray of debris on the surface. Almost all of the lithium debris are in clusters and are embedded into the Si wafer surface resulting in craters that are a few nanometers to 300 nm in depth. A few of the deepest craters have large diameters measuring approximately 50 μm. Tin samples show a nearly even coating of tin across the surface of the Si wafer, with some surface damage found at the center of the witness sample. The depth measured for tin at sample center is near 450 nm with a diameter about 30 μm. Tin samples also show tin debris adhered to the surface, that are about 40 μm in diameter, and these may respond well to surface cleaning methods.

6.5 Comparison to Calculations

The experimental conditions were input into a 1-D Lagrangian based, hydrodynamic code discussed in chapter 3 to study the expansion characteristics of the plasma temperature and density for lithium. This code assumes local thermodynamic equilibrium (LTE) and isotropic emission. For a 1064 nm wavelength, 10 ns gaussian laser pulse with a 50 μm beam radius at target, the maximum plasma temperature is calculated to be 18 eV (Fig. 6.8). The density region is closer to 10^{21} /cm^3 (Fig. 6.8). This correlates to the estimated values of temperature and density from the line height ratios.

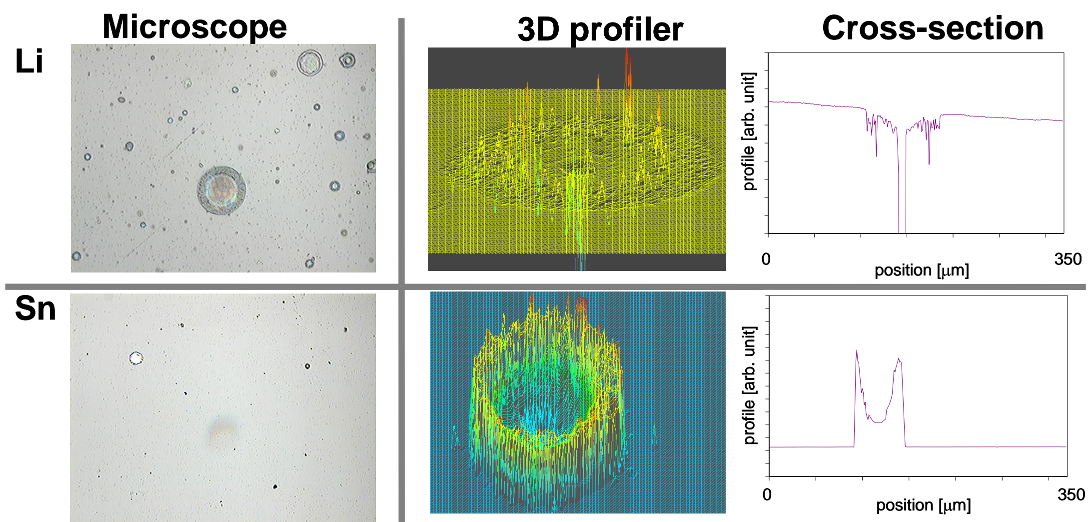

Figure 6.7: Processed images of the debris deposited on silicon wafer sample surfaces, obtained using optical microscopy

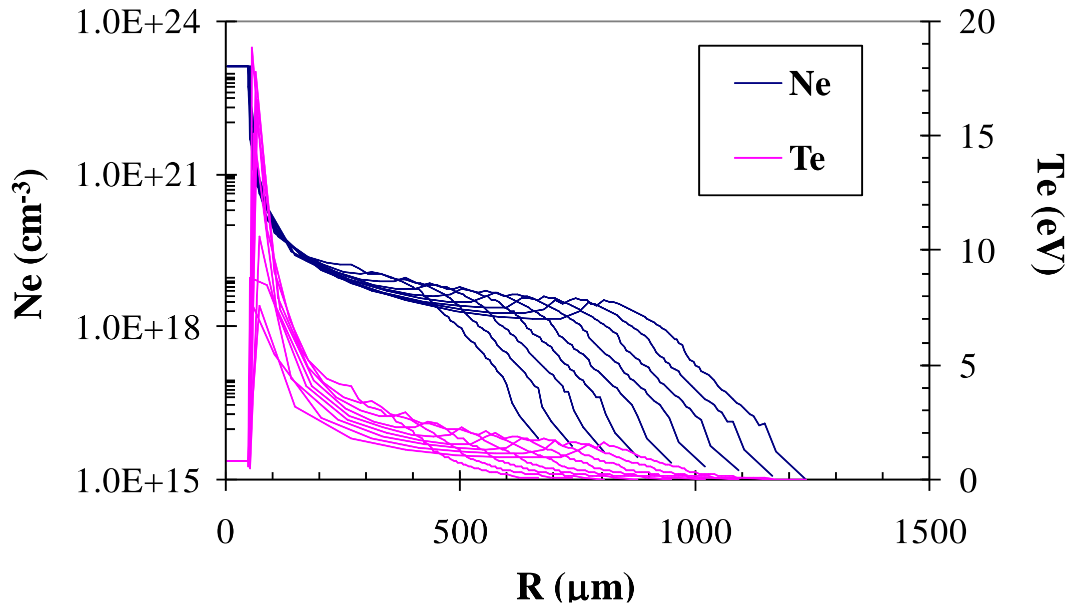

Figure 6.8: Spectrum from a Li laser plasma source in the EUV region

Under LTE, using the Saha equation, lithium isosequences with the fractional population for two different ion densities were calculated (Fig. 6.9). Figure 6.9 (a), calculated for the electron density at 10^{20} /cm^2 show that H-like ions are populated at a plasma temperature range from 10-20 eV, which is comparable to the experimental temperature determination obtained from the line height ratios. At larger distances and greater time scales, the number densities of the plasma are low and the movement of the boundary region is rapid, so LTE is probably not a good assumption for accurate temperature determinations and more detailed calculations are necessary.

6.5.1 Atomic Level Structure Determinations

Oscillator strengths of transitions of lithium ionization stages were also obtained using atomic physics calculations obtained using the cowan suite of codes. The transitions resulting from the excited states of the Li II and Li III ions are shown in Fig. 6.10.

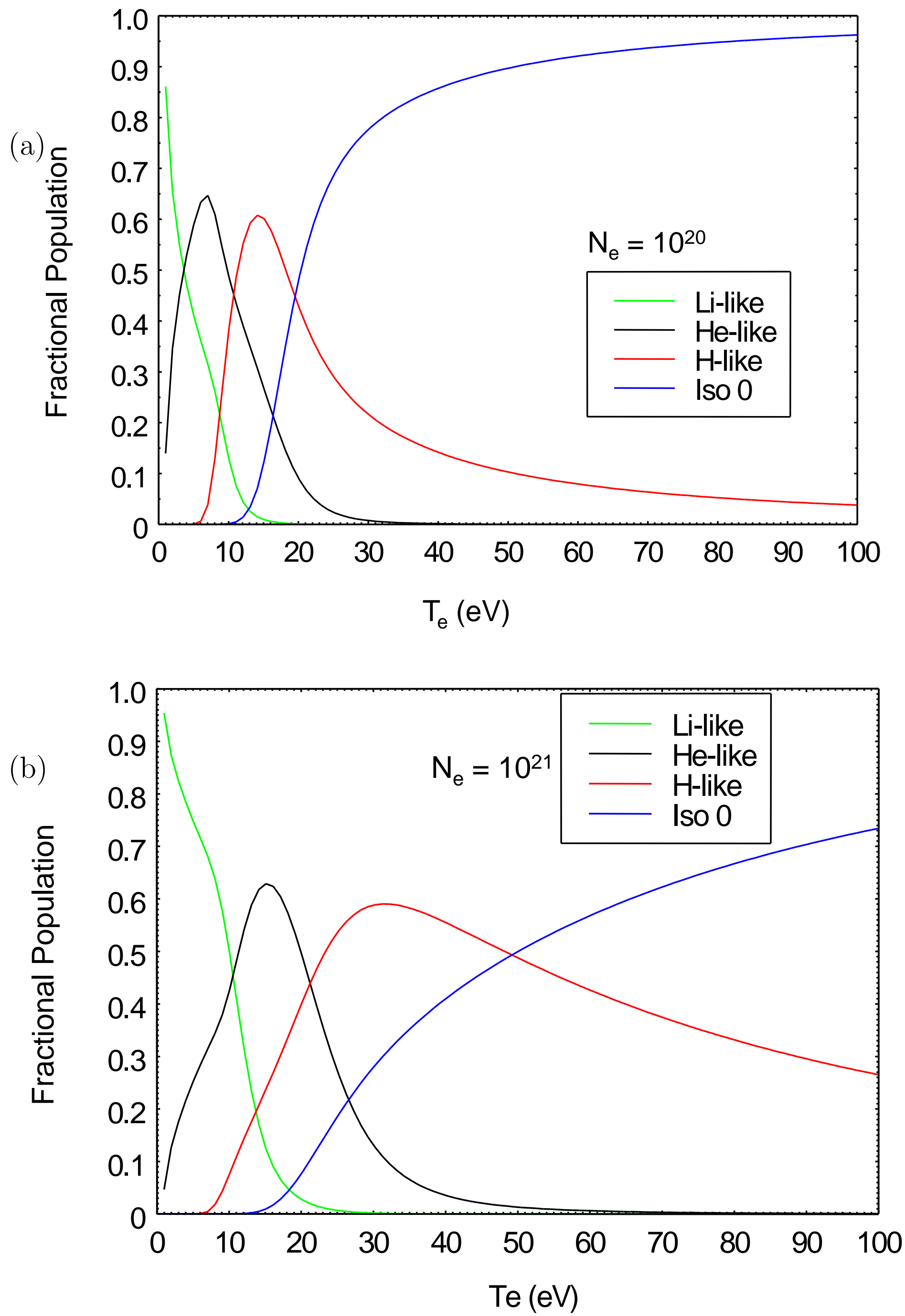

Figure 6.9: Lithium charge-state distribution as a function of temperature for two different electron densities

6.5.2 Radiation Transport

Details of the plasma processes can be better understood through the use of codes that are multi-dimensional, and treat the plasma evolution in the non-LTE, time dependant regime. CRETIN code is a 2D, LTE/non-LTE atomic kinetics radiation transfer code, developed at Lawrence Livermore National Laboratory (LLNL) for modeling laser plasmas [8]. Energy transfer processes from laser to target such as inverse bremsstrahlung and resonance absorption, temporal evolution of plasma determined by the hydrodynamic and electron temperature calculations, and detailed calculations on atomic populations are all coupled to be included in Cretin simulations. Description of plasma matter at the atomic level and transition strengths are supplied to the code as external files. Hydrodynamic inputs can be post processed from the existing 1-D code or can be calculated using lagrangian routine in CRETIN. For lithium calculations, MEDUSA output for plasma expansion was provided for cretin calculations. Detailed atomic kinetics, radiation transport, plasma temperature evolution, and time evolved spectral distribution of atomic populations are obtained. CRETIN self-consistently follows the time evolution of atomic populations and photon distributions as radiation interacts with low-density plasma. Distribution of electrons in various atomic levels, relating to each atomic state is modeled for each element in the plasma. Synthetic spectra were calculated for lithium laser plasma for a number of laser irradiance conditions, as the populations evolve in time.

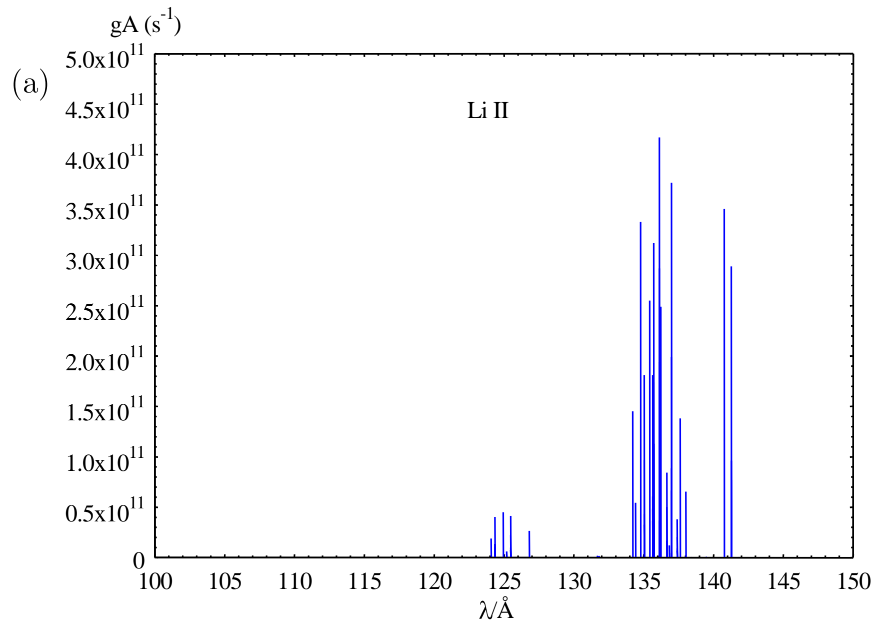

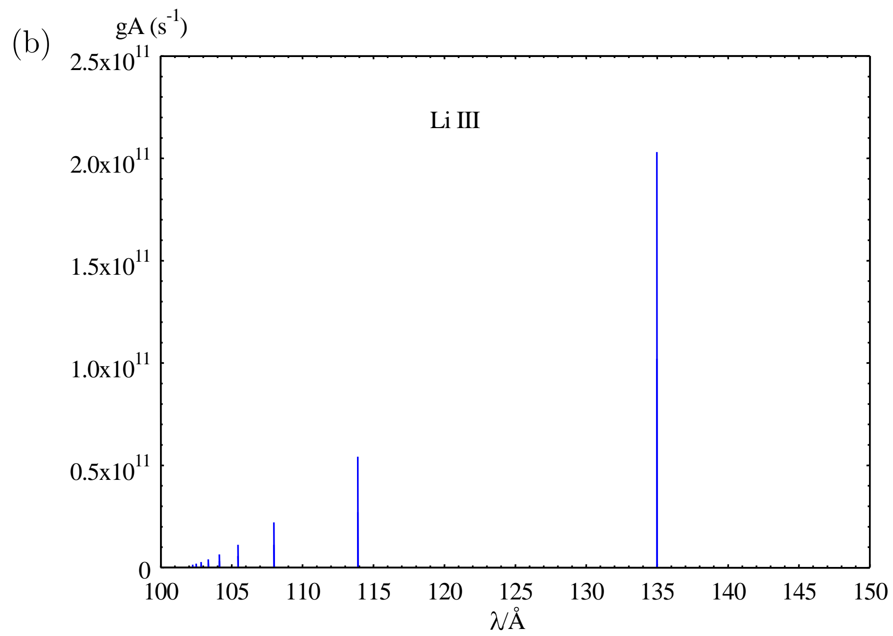

Figure 6.10: Calculated transition lines for Li^{+} and Li^{2+} ions

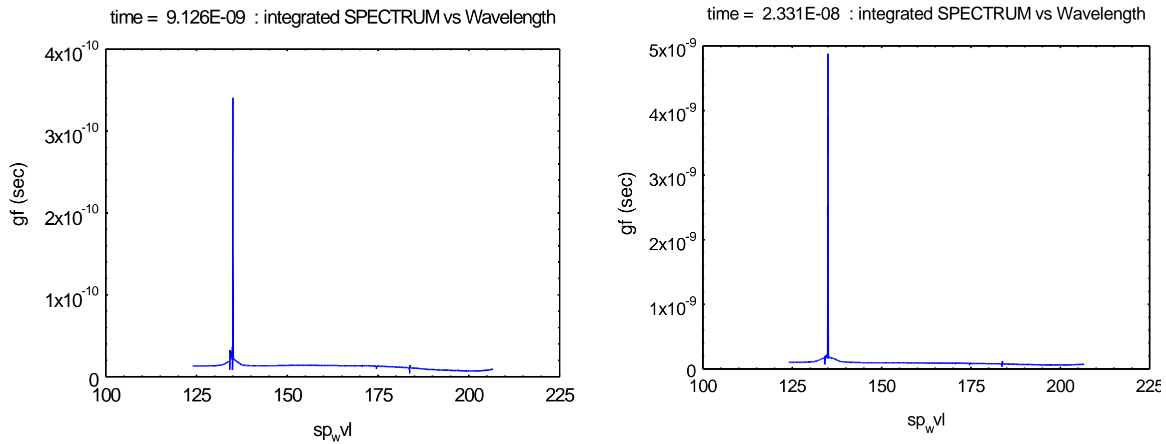

Figure 6.11: CRETIN 2D-radiation transport code [8, 6] calculated spectrum from of lithium laser plasma source at 13.5 nm

6.6 Discussion

Sn and Li laser produced plasmas have proven to be viable, efficient sources for EUV. Single, bright line emission from lithium at 13.5 nm makes this source a strong candidate for lithography light source. In addition, lithium is spectrally clean requiring no additional spectral purity filters, and it is abundant in nature. It is disadvantageous in that it is difficult to handle, and oxidizes easily. UTA emission in tin is brighter than single line emission, leading to higher conversion efficiencies, but it also leads to spectral purity issues.

Aside from achieving high power levels, both source schemes suffer from debris issues. Ions, particulates, and dust from coming off the plasma can damage the surface layers of the mirror, reducing the reflectivity of MLM, thus decreasing the source lifetime. EUV lithography tool design requires high repetition rate, and mass limited targets to minimize debris emanated from source. Tin-doped mass limited micro-plasma EUV sources developed at UCF are considered to be well suited for use as the next generation EUV sources. Our

studies have shown high conversion efficiency for this source, with minimal tin usage. Extensive data collected for different mitigation schemes show promising results for the tin droplet target, as well [9].

6.7 Summary

The evaluation of the potential of lithium as a laser-plasma source, both theoretically and experimentally, was completed in this chapter. Theoretical calculations show optimum intensity region for lithium for attaining high conversion is close to 5.0×10^{11} W/cm^2 with a plasma temperature near 18 eV. Experimental studies compare directly, the conversion efficiency and optimum irradiation conditions for both planar tin and lithium solid targets. At 13.5 nm, the best conversion efficiency (CE) for lithium was found to be 2.2% at intensities near 7×10^{10} W/cm^2. The highest CE measured for tin was near 5.0% at an intensity region close to 1×10^{11} W/cm^2.

6.8 References

[1] Donna J. O'Connell. Characterization of a lithium laser produced plasma at 135 å for extreme ultraviolet projection lithography. Master's thesis, University of Central Florida, CREOL & FPCE: The College of Optics and Photonics, 1994.

[2] Marc A. Klosner. *Intense capillary dischrge plasma extreme-ultraviolet sources for EUV lithography and other EUV imaging applications.* PhD thesis, University of Central Florida, CREOL & FPCE: The College of Optics and Photonics, 1998.

[3] D. Brandt. Lpp euv source development for hvm, presented at euvl symposium. Presentation at EUVL Source Workshop, Baltimore, MA, Oct. 17 2006.

[4] Hans R. Griem. *Plasma Spectroscopy.* McGraw-Hill Book Company, New York, 1964.

[5] R. Stuik, F. Scholze, J. Tummler, and F. Bijkerk. Absolute calibration of a multilayer-based xuv diagnostic. *Nucl. Instrum. Methods*, 492:305–316, 2002.

[6] Simi A. George, William Silfvast, Kazutoshi Takenoshita, Robert Bernath, Chiew-Seng Koay, Greg Shimkaveg, Martin Richardson, Moza Al-Rabban, and Howard Scott. Euv generation from lithium laser plasma for lithography. volume 6151, page 615143. SPIE, 2006.

[7] Simi A. George, William T. Silfvast, Kazutoshi Takenoshita, Robert T. Bernath, Chiew-Seng Koay, Gregory Shimkaveg, and Martin C. Richardson. Comparative extreme ultraviolet emission measurements for lithium and tin laser plasmas. *Opt. Lett.*, 32(8):997–999, 2007.

[8] Howard Scott. *CRETIN User's Manual.* Lawrence Livermore National Laboratory, 2001. UCRL-MA-124173.

[9] Kazutoshi Takenoshita. *Debris characterization and mitigation of droplet laser plasma sources for EUV lithography.* PhD thesis, University of Central Florida, Department of Electrical Enigineering and Computer Engineering, 2006.

CHAPTER 7

CALIBRATED BROAD-BAND SPECTROSCOPY OF SN-DOPED DROPLET LASER PLASMAS

7.1 Introduction

A realistic EUV source for lithography and microscopy needs to meet stringent requirements on high-power, high efficiency, and long lifetime. The patented source scheme being developed at laser plasma laboratory utilize droplets that are of diameter less than 50 μm. These droplets are generates are high repetition rates and are coupled to a focused laser beam. This source configuration has the potential to meet all of the needed requirements for a high-power, laboratory EUV source. In this chapter, a summary of in-band and broad-band investigations of emission from sn-doped droplet laser plasma source are presented. The evaluation of out-of-band (OOB) radiation in the context of the source requirements set-forth for EUVL is completed.

7.2 High-Repetition Rate Tin-doped Droplet Laser Produced Micro-plasma Source

The source development utilizes patented [1], mass-limited source concept [2], where the number of atoms emitting EUV is limited to only what is required for high efficiency EUV yield. Then, with complete ionization on the target, minimal debris is expected from the plasma generation process. Controlling of debris from plasma will limit the number of

particles reaching expensive optics, thus extending the lifetime of the source-collector module (SoCoMo).

Initial mass-limited laser plasma source studies were completed with water droplet targets [3]. The strong O^{5+} (4d-2p) transition at 13 nm (Fig. 7.1), low debris on collector optics, cost effectiveness, and discrete line emission made water droplets very attractive as an EUV source. Although debris free, water droplets did not provide the high conversion efficiencies into the 13.5 nm needed. Since tin was found to be an efficient emitter of EUV radiation into the required bandwidth, a water based solution of tin as a mass-limited droplet source was proposed. Broad-band studies of emission from tin-doped droplet plasmas are completed in this chapter.

7.2.1 Need for Out-of-Band Emission Studies

Mo-Si interference coatings are highly reflective in the VUV/Visible/Infra-red region, thus source spectral purity is a requirement. Mo-Si MLM average reflectivity for 130 nm-400 nm is near 60%, where these wavelengths reaching the wafer behave as flare affecting the critical dimension control [4]. More than 90% reflectivity is expected for IR radiation where it will be transmitted through an optical system with nominal attenuation.

Current research for a high power EUV source is driven by the semiconductor industry with their need for enhanced chip performance. In an EUVL scanner system, IR radiation is expected to cause thermal expansion of the wafer, therefore, reducing overlay accuracy. Wavelengths absorbed by the mirror surfaces can result in mirror heating leading to accelerated degradation of the multilayer structures. Thus, quantitative assessment of spectral purity of any source configuration in these wavelength regions becomes a necessity in order

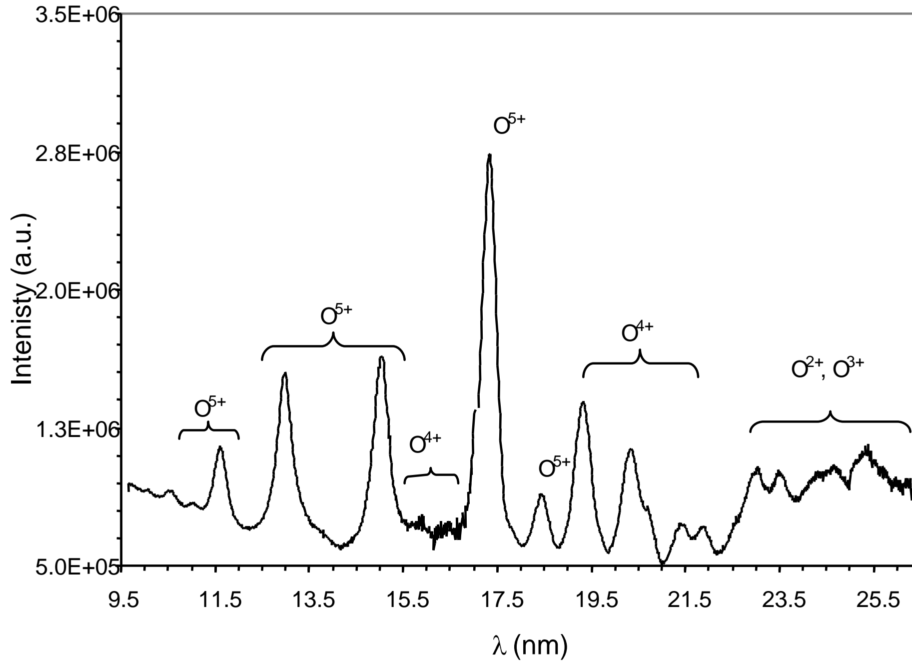

Figure 7.1: Spectrum from water droplet plasma source in the EUV region [3]

to design an appropriate method to control propagation of unwanted radiation through the optical system.

Broad-band emission from sources such as laser plasmas that are candidates for EUV lithography stepper systems needs to be accurately assessed. Design requirements for the stepper tool dictate high spectral purity of the high-power light source at the illuminator entrance, with low levels of radiation in specific off-band spectral regions. Quantifying the emission levels arising from atomic transitions, Planckian radiation, and laser scattering is imperative to the successful implementation of laser plasma sources for EUVL. Attempts on evaluating and quantitatively assessing emission from tin-droplet laser plasma source in the X-Ray, Ultra-Violet (UV), Visible and Infra-Red (IR) region from the source is presented.

7.3 Experimental Arrangements

A number of different spectroscopic instruments are used for the measurements completed in this chapter. Each instrument requires different levels of throughput for optimum signal to noise ratio, necessitating the use of more than one experimental set-up. Two laser systems were available for completing spectroscopy, metrology and debris experiments involving EUV generation. The majority of the EUV radiation studies utilize a custom built, Q-switched Nd:YAG oscillator-amplifier laser system with laser wavelength at 1064 nm, operating at 1 Hz, producing 1.6 J per pulse, and with pulse duration of 11.5 ns. The laser beam output has an M^2 of 1.5, which is focused in the far-field to a spot size diameter of 35 μm using a 10 cm lens. Details of the laser layout, the far-field beam profile, the temporal pulse shape, and detailed mapping of the focal region are reported in chapter 5. The beam from this laser is directed in to a 12-port cylindrical vacuum chamber, and the targets are placed at the center of the chamber. The diameter of the chamber is 45 cm, and experiments are conducted at a pressure below 10^{-3} Torr, obtained using a 361 liters/s turbo-molecular drag pump backed by a roughing pump. The spectrometers are interchanged with the back-illuminated CCD, and are set-up 90° to the pump laser beam. The flying circs EUV detector is set-up 30° to the incident laser beam.

The second laser accessible to the EUV experiments is the Quanta-Ray GCR 190-100 which is a commercially available laser from Spectra-Physics. This laser is Q-switched, Nd:YAG at 1064 nm, providing higher repetition rates at 100 Hz with 340 mJ maximum energy and a pulse length of 10 ns. This laser is primarily used for multi-pulse debris measurements [5]. The beam from this laser was used for the visible and near-band spectroscopy

of the Sn-doped and water droplet spherical targets described in this chapter.

7.3.1 Tin-doped Droplet Generation

Utilizing the mass-limited target concept, liquid droplets of about 30 μm - 50 μm in diameter with each droplet containing a small amount of tin was generated using commercial ink-jet capillary. The target solution is prepared with stannous Chloride ($SnCl_2$) and deionized water. This solution is forced through a capillary by pressurizing the reservoir. The fluid back pressure is maintained through the use of compressed nitrogen; the backpressure is usually on the order of 1000 kPa.

The ink-jet capillary is made of glass and has a 10 μm diameter. The glass capillary is resonantly driven by a piezo-crystal, which is in turn driven by a square wave voltage signal. Frequencies of 10 kHz - 200 kHz can be obtained and the typical frequency of droplet generation for experiments completed for this thesis is 34 kHZ. A portion of the jet-driving signal is split off and fed into phase-locked loop electronics that triggers the ionizing laser. By adjusting the delay between the droplet formation and the laser trigger, the synchronization of the laser pulse to a droplet is achieved.

The droplet generation frequency and the laser repetition-rates are typically quite different. This means that for the 1 Hz laser and 34 kHz droplet generation, only one droplet out of the 34 droplets generated is ionized. Thus, the unused droplets need to be collected in a way that the vacuum levels inside the chamber can be preserved. A cryogenic trap cooled by liquid nitrogen is used to collect the unused droplet train and an electric chopper is used to impede the ice crystal formation. The droplets are generated at velocities of 2×10^4 cm/s or better with stabilities of 3 μm at distances of about 10 mm from the capillary opening.

In order to monitor the droplet stability and laser coupling during experiments, the droplets are back illuminated and the images are acquired using a visible CCD. Methods used for this are presented in much more detail in thesis by Chiew-Seng Koay [6]. The illumination source is a green light-emitting diode (LED) by Luxeon V Star, model # LXHL-LM5C, with lambertian radiation pattern. The LED provides up to 160 lumens of brightness. The LED is strobed to match the droplet generation frequency using the input electrical signal from the phase-locked loop which is the same signal that drives the droplet generation. An image of the droplets at a given frequency is given in Fig. 7.2

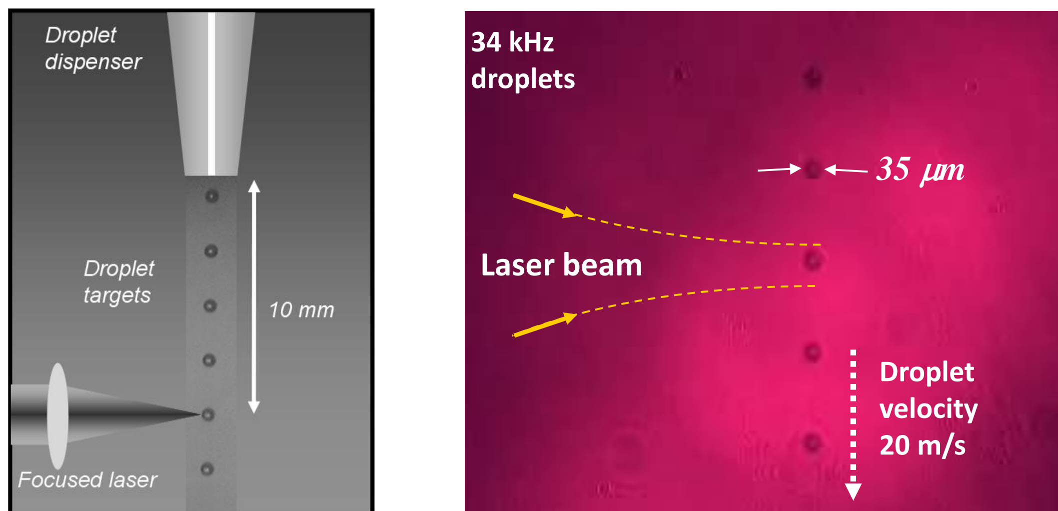

Figure 7.2: Photograph of a thin chain of droplet targets together with a cartoon of a laser beam focused on a droplet

Different spectroscopic methods are used to characterize emission in the different bandwidth regions [7]. A high resolution flat field grating spectrograph is used in order to study the in-band emission wavelength, a transmission grating spectrometer for near-band region and a digital triple grating spectrograph for investigating UV-Visible-Near IR

regions of emission from the plasma. For measurements in the VUV region, from 30 nm-200 nm, a Seya-Namioka design based monochromator is used. Detailed description of each of the instruments and the results obtained are reported in the next section. The spectral data obtained using each of the instruments is a convolution of the plasma emission with the filter transmission, grating diffraction efficiency, and CCD sensitivity. True intensity of the emission is determined through the deconvolution of these factors from the recorded data. Calibrated transmission curves for the filters and mirrors used in the experiments were obtained from NIST and details of the deconvolution methods can be found in previous student theses [3, 6].

7.4 Emission from Tin-doped Droplets

Initial studies were conducted for determining the best sn concentration in the droplet for high conversion efficiency, while keeping the debris to a minimum. The data published (Fig. 7.3), found that 27-30% Sn solution gives the best CE [8]. At these concentrations, each droplet contains about 10^{13} - 10^{15} tin atoms.

7.4.1 In-band Spectroscopy and Metrology

A summary of in-band emission studies of tin-doped droplets completed and reported in the previous graduate thesis is given [6]. As in the case of planar tin spectra, an increase in UTA height and spectral narrowing as a function of intensity is observed. In contrast to the planar tin spectra, the droplet spectral data show contributions from the oxygen lines. Emission lines from the dominant O^{5+} ion at wavelengths of 11.6 nm, 13.0 nm, 15.0 nm, and 17.3 nm are observed. The highest emission for tin droplets are found to be near an

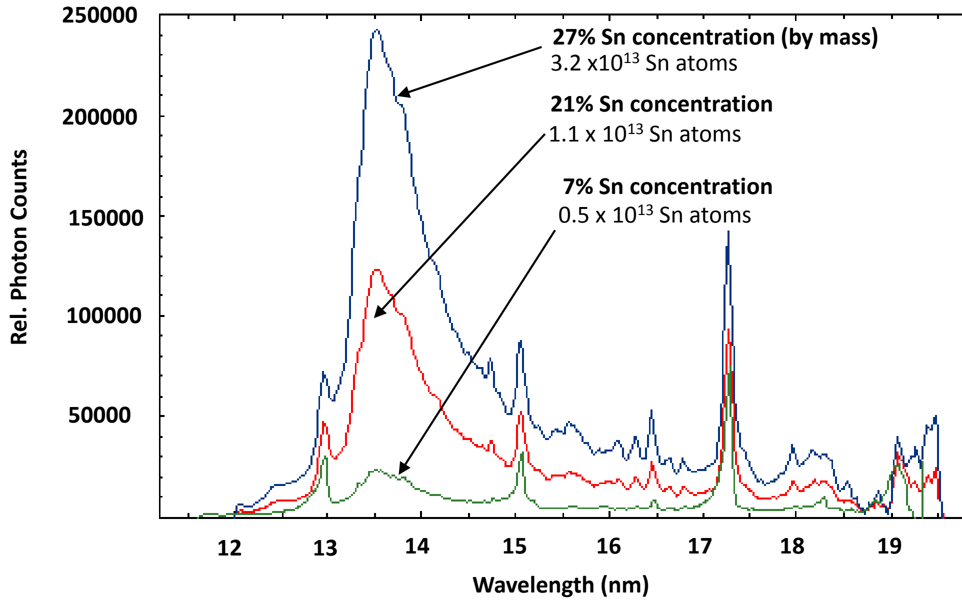

Figure 7.3: EUV emission in the 12 nm - 20 nm region from Sn-doped droplets at various concentrations

intensity of 1.4×10^{11} W/cm^2 giving conversion efficiencies that are better than 2.0%.

EUV images of the tin droplets plasmas were obtained as the focusing lens is translated along the z-axis [6]. The source size changes as the lens is translated due to the change in beam spot size at target. The arbitrary position labels, P0 - P8, shows plasma size variation from 75 μm - 125 μm given in Fig. 7.5. The smallest plasma is found at P4 which is concluded to be the minimum focal spot or at the tightest focus of the lens at target.

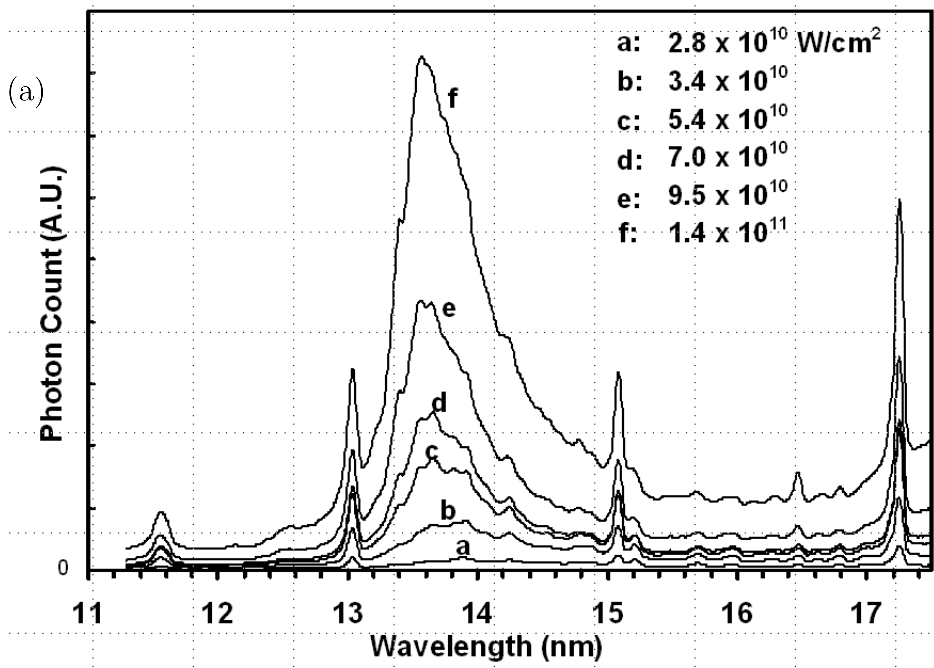

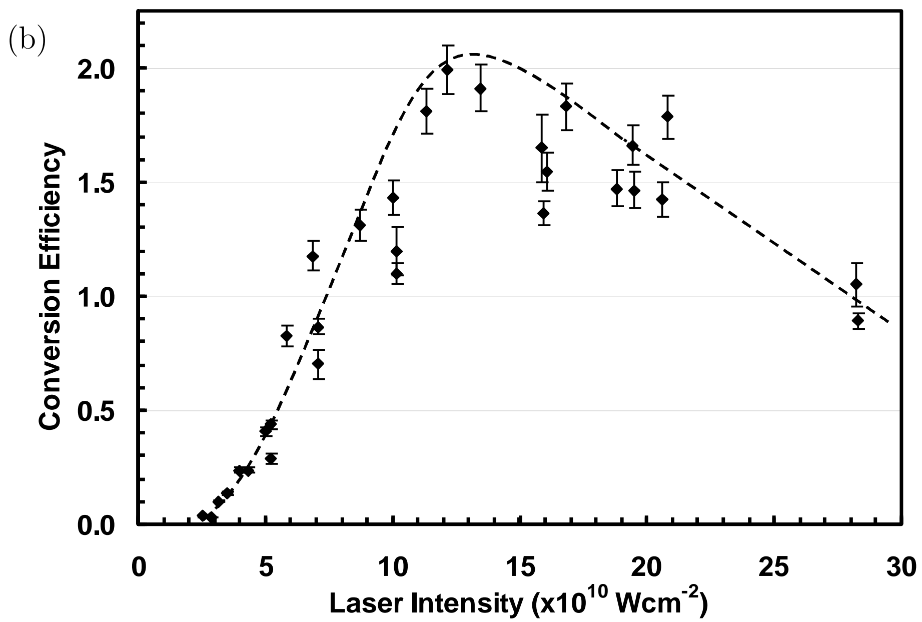

Figure 7.4: (a) In-band emission spectra and (b) high conversion efficiencies measured from tin-doped droplet targets

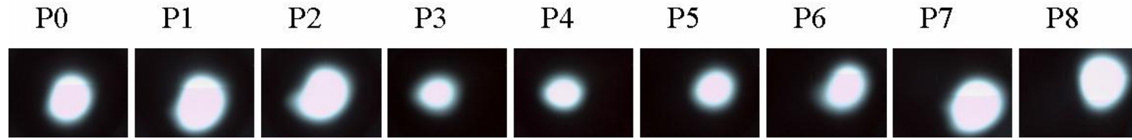

Figure 7.5: Images of the Sn EUV plasma as the focal diameter at the droplet target is varied by translating the lens from from one position to the next.

7.4.2 Broad-band EUV Spectroscopy

Transmission Grating Spectrometer (TGS) is used to survey the broad band emission in the immediate vicinity of the 13 nm UTA, complimentary to the FFS. The radiation source illuminates the grating at near normal incidence through the slit located in the entrance arm of the TGS. The grating diffracts the incoming radiation in an angle, where the angle of diffraction is dependent on the wavelength and diffraction order. The diffracted radiation is collected on a detector plane located at the end of the observation arm of the TGS, where it is recorded using a CCD camera. Higher order diffraction intensities will depend on the diffraction efficiency of the grating in the higher order, and the filter is placed between the recording medium and the slit.

The TGS used for experiments here utilizes a free-standing 10,000 lines/mm Si_3N_4 grating, giving a resolution about 0.06 nm (Fig. 7.6. The slit size being used is 40 μm, and we have on hand slit sizes ranging from 10 μm - 200 μm. Metal Zr/Al/Sn filters, each of thickness 0.5 μm, are being used for wavelength selection in the 1 nm-20 nm region. Corrected spectra for near band region from 0 nm - 28 nm for tin droplet source is shown in fig 7.7, at an intensity of 1.0×10^{11} W/cm^2 [9, 10]. High resolution makes individual line identification possible and comparison of transitions to calculated line strengths. Sn UTA and lines from oxygen ions in the short wavelength region is found.

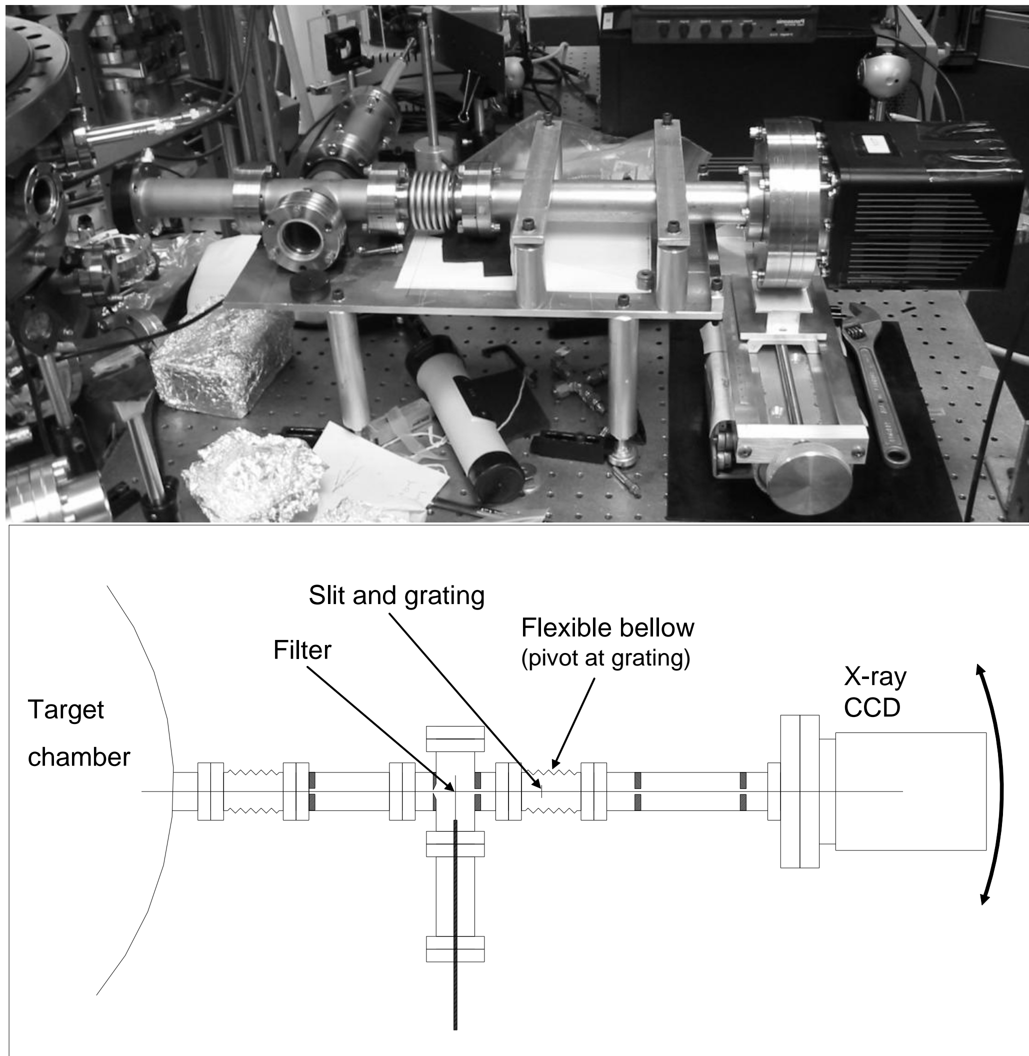

Figure 7.6: Picture and schematic of the transmission grating spectrometer

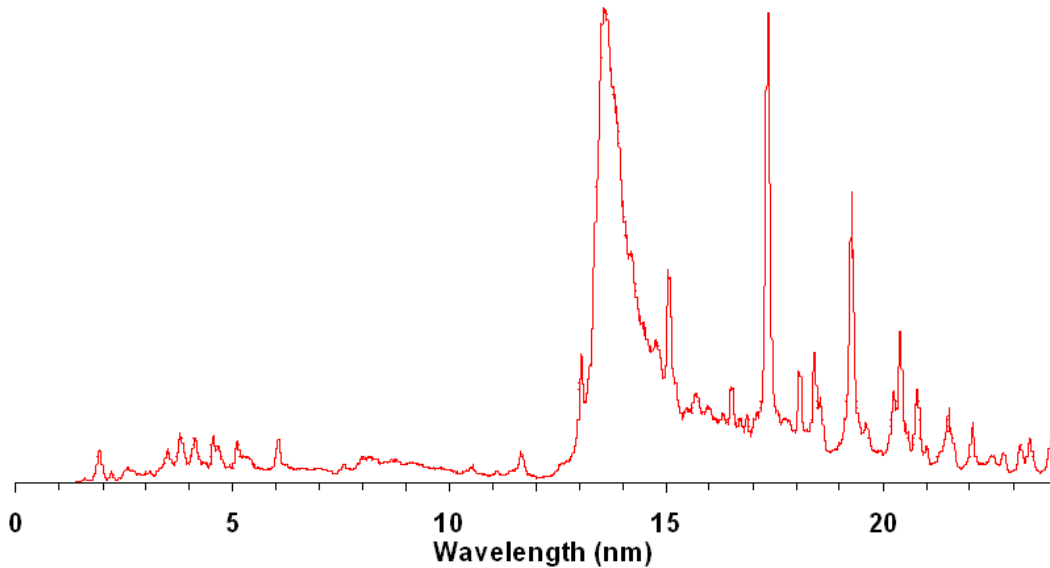

Figure 7.7: TGS spectral measurements obtained sn-doped droplets in the EUV region from 1 - 28 nm at an intensity of 1.0×10^{11} W/cm^2

For oxygen line identification, the tabulated data provided by NIST atomic spectral database was used for oxygen. At these temperatures, the only oxygen ions of up to O^{5+} are expected and a plot of all the expected emission lines from these ions in given in Fig. 7.8.

7.4.3 VUV Spectroscopy

Commercially available spectrometers were used for the longer wavelength study. Initial spectral measurements in the VUV region were completed using a Model 234/302 scanning monochromator developed by McPherson. This instrument covers a spectral range from 25 nm - 400 nm. The optical design of the monochromator is based on the seya-namioka mounting principle [11] and the grating in this monochromator is focused at 200 mm. The entrance and exit slits are placed at the focus of the grating and the slits are separated by

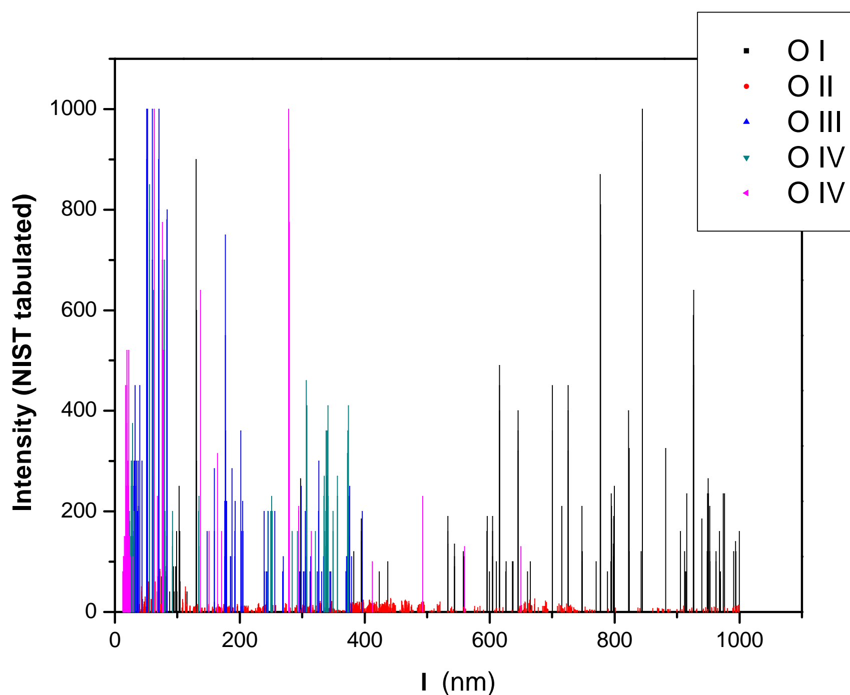

Figure 7.8: Observed lines from all oxygen lines compiled by the National Institute of Standards and Technology

a 64° angle.

Measurements were completed using a 600 lines/mm, type IV, holographic, aberration corrected, concave grating with reflective coating of Al w/MgF_2, giving an approximate resolution of 0.2 nm. The slit width is is adjustable from 10 μm to 3 mm. McPherson model 789A-3 scan controller is used for scanning across wavelengths. The detector system consists of a model R6095, end-on PMT with the detection capability ranging from 300 nm - 650 nm. The detection peak for the PMT is at 420 nm, and this is coupled to a sodium salicylate scintillator window with peak fluorescence also at 420 nm. The scintillator response is from below 30 nm to greater than 340 nm. The PMT power supply maximum output is -1000

VDC, and a Keithley model 6485 picoammeter is used for signal measurements. A new 1200 lines/mm grating is installed in the monochromator, which will provide better resolution with a scanning range of ¡30 nm - 550 nm. There are a number of strong transitions from

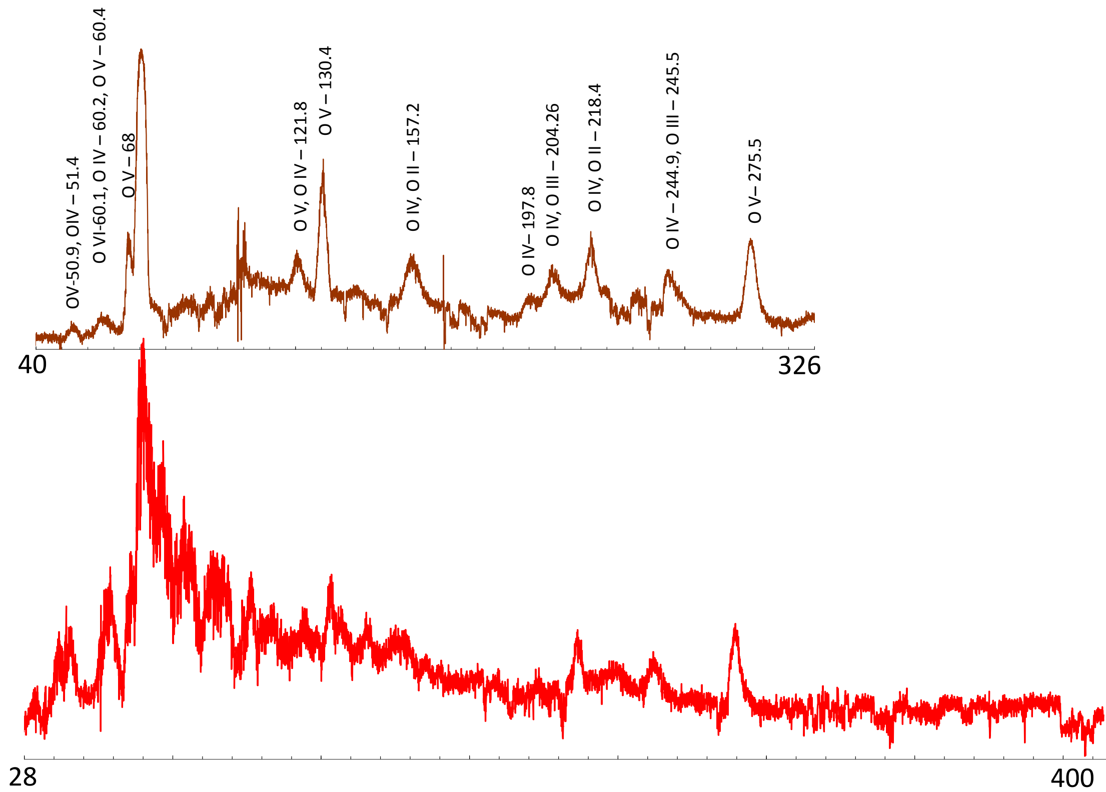

Figure 7.9: Spectral measurement sn-doped and pure water droplets in the VUV region

oxygen ions, O^{5+} and O^{4+} and a small amount of UTA emission detected from the droplet plasma outside the mirror bandwidth (Fig. 7.9). Exact line identification is not possible for this measurement, since the resolution is poor. New grating with higher line density was installed and further measurements with improved optical resolution will be obtained in the near term. The emission in the EUV region from 1 nm to 100 nm, external to mirror bandwidth is not considered critical for imaging, since MLM reflects very little or none of

the radiation emitted in this region. Emission energies from tin targets above 50 nm up to 200 nm region from this source needs to be quantified and this is to be completed. This initial measurements show very little emission in the critical wavelength region, but actual energy of emission cannot be determined until the monochromator or a spectrometer can be absolutely calibrated for measurements in this region.

7.4.4 Visible/IR Spectrocopy

A Model 1235 Digital Triple Grating spectrometer by EG&G-Princeton Applied Research was used to record the spectral output of tin-doped droplets and pure deionized water droplets in the 400 nm to 1200 nm region. The spectra was collected by imaging the plasma on to the numerical aperture a fiber optic cable, which is the input to the spectrometer.

For direct calibration and calculation of the energy output from both sources in this wavelength region, a fast photodiode coupled to an oscilloscope was used to detect and record all radiation collected by the spectrometer. The procedure was repeated after blocking scattered laser radiation, so that the energy contribution of the source to the visible region can be determined. For energy calibration, a laser diode source of known power and wavelength was used at the fiber input. In this way, the counts detected by the spectrometer can be translated into energy units.

Every single peak observed in the tin spectra is also observed in the pure water target spectral signature (Fig. 7.10). In fact, the spectral signature for both targets is identical except for the difference in peak heights owing to the longer exposure time of the water droplets during data collection. Calculations also predict strong transitions in the visible region for Chlorine, but Chlorine lines are not observed in the spectral measurements obtained. It is concluded that there are no detectable transition lines found from both Sn and Cl in the wavelength region being investigated. This may be partly because the percent composition of Chlorine (16%) and Sn in the droplet is small in comparison to hydrogen and oxygen. Lower ionization states typically emit more in the visible region, so it seems more plausible to conclude that at 120 mJ of laser energy, higher ionization states are populated for both atoms, thus they do not have strong emission lines in the long wavelength region.

The energy produced by the source for these wavelengths was calculated for the Sn-doped droplet. The input laser energy was approximately 120 mJ. From the photodiode signal, about 0.5 mW of power from all radiation into the 2πSr was measured. This is crucial to the heating considerations of the stepper system.

7.5 Broad-band spectrum

A series of experiments in the extended electromagnetic spectral range to quantify the line and Planckian emission, as well as the amount of laser scattering of plasma produced from tin and water droplet target sources have been completed. The spectral signatures of the two sources are compared and the line identifications have been made. Two methods of calibration of the spectral data are performed using a laser source with known emission wavelength in the region of investigation. The complete source spectrum obtained for the

Sn-doped droplet plasma generation at an intensity of approximately 1×10^{11} W/cm^2 is given in Fig. 7.11.

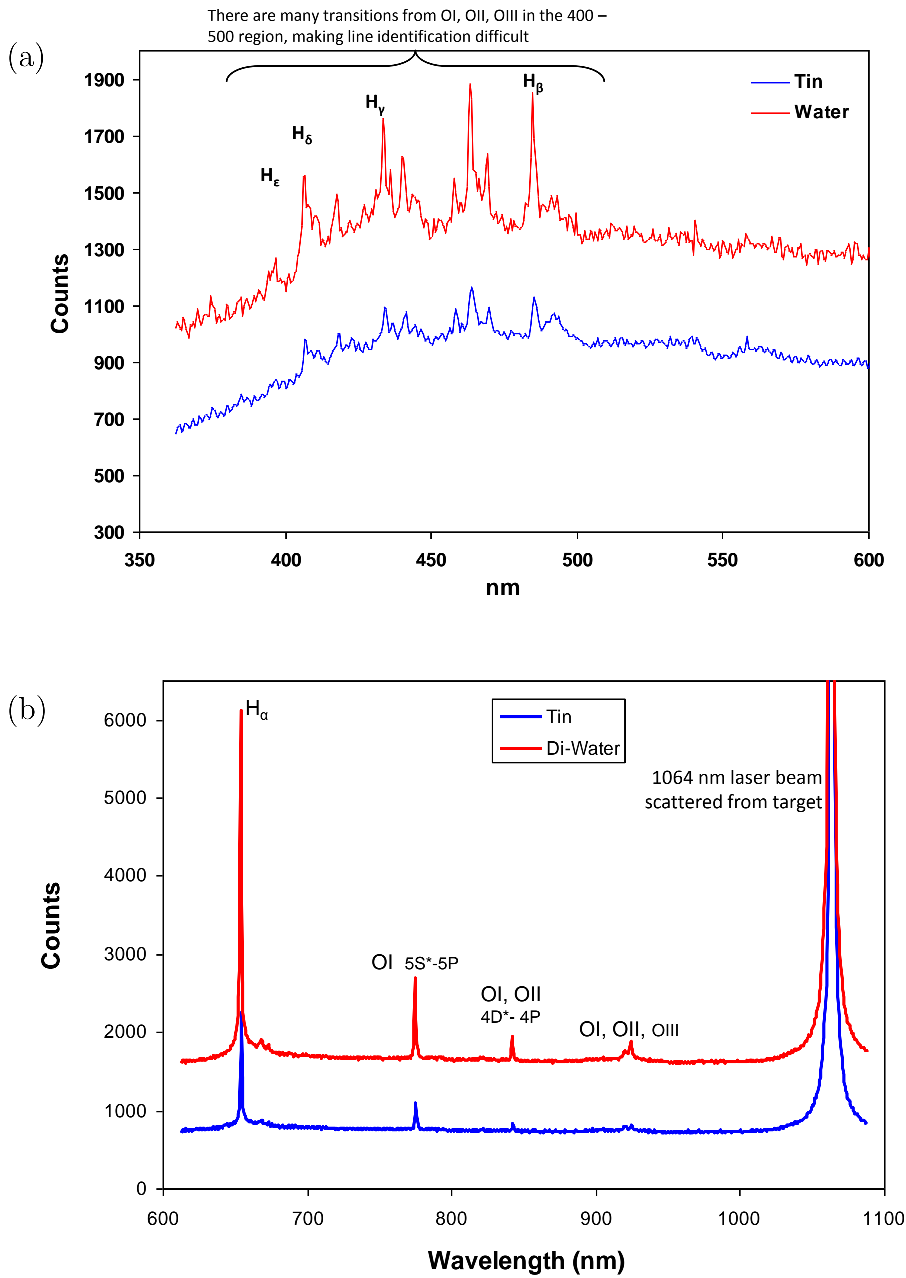

Figure 7.10: Visible emission from sn-doped droplet targets at optimum EUV emission conditions

7.6 Summary

Extensive studies of laser plasmas under controlled experimental conditions with laboratory developed spectroscopic techniques as the primary diagnostic have allowed the improvement of EUV output from the tin-doped droplet target considerably. The irradiance parameters are modeled with existing hydrodynamic, and atomic codes, to better understand the plasma parameters that best contribute to EUV emission for this target. Detailed computational studies are underway for providing calculations that are more accurate, thus the underlying physical processes can be better explored, resulting in source efficiency.

7.7 References

[1] Martin C. Richardson. Micro-droplet plasmas, March 2005.

[2] F. Jin and M. Richardson. New laser plasma source for extreme-ultraviolet lithography. *Appl. Opt.*, 34(25):5750, 1995.

[3] Christian Keyser. *Optical and spectral characterization of the water droplet laser plasma EUV source.* PhD thesis, University of Central Florida, Department of Physics, 1994.

[4] Vivek Bakshi, editor. *EUV Sources for Lithography.* SPIE Press, Washington, 2005.

[5] Kazutoshi Takenoshita. *Debris characterization and mitigation of droplet laser plasma sources for EUV lithography.* PhD thesis, University of Central Florida, Department of Electrical Enigineering and Computer Engineering, 2006.

[6] Chiew-Seng Koay. *Radiation studies of the tin-doped microscopic droplet laser plasma*

light source specific to EUV lithography. PhD thesis, University of Central Florida, CREOL & FPCE: The College of Optics and Photonics, 2005.

[7] Martin C. Richardson, Chiew-Seng Koay, Kazutoshi Takenoshita, C. Keyser, S. George, Somsak Teerawattansook, Moza M. Al-Rabban, and H. Scott. Laser plasma euvl sources: progress and challenges. volume 5374, pages 447–453. SPIE, 2004.

[8] M. Richardson, C.-S. Koay, K. Takenoshita, C. Keyser, and M. Al-Rabban. High conversion efficiency mass-limited sn-based laser plasma source for extreme ultraviolet lithography. *Journal of Vacuum Science and Technology B: Microelectronics and Nanometer Structures*, 22(2):785–790, 2004.

[9] Scott Mackay, editor. *High conversion efficiency microscopic tin-doped droplet target laser-plasma source for EUVL*, volume 5751 of *Proc. SPIE*, 2005.

[10] Scott Mackay, editor. *EUV spectroscopy of mass-limited Sn-doped laser micro-plasmas*, volume 5751 of *Proc. SPIE*, 2005.

[11] James A. R. Samson. *Techniques of Vacuum Ultraviolet Spectrosocpy.* John Wiley and Sons, Inc., New York, first edition, 1967.

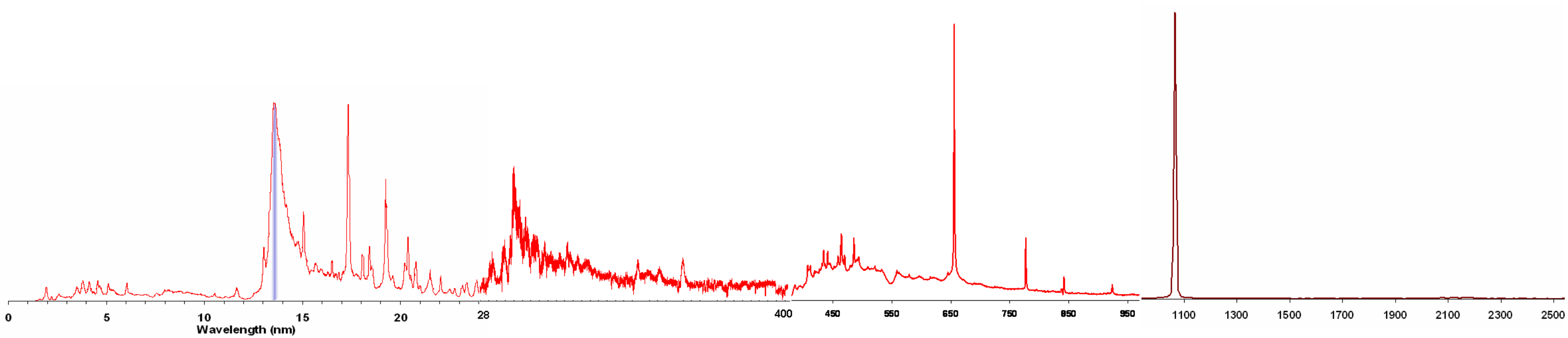

Figure 7.11: Complete spectral emission from the tin-doped droplet target at conditions optimum for EUV emission. Different spectrometric configurations were used for detection of emission into the different wavelength regions. The y-axis units are not used in this plot since the different instruments are not cross calibrated against each other.

CHAPTER 8

EUV GENERATION WITH A FIBER LASER

8.1 Introduction

This chapter demonstrates the experimental methods employed for improving narrow-band EUV source power levels by creating electron temperature and ion density conditions that are optimum for 13.5 nm emission from fiber laser and tin-doped droplet target. Tin as a target material is advantageous since it is shown to have many transitions arising from Sn^{7+}-Sn^{13+} [1]. The ground configuration [Kr] $4p^6 4d^n$, n = 2 to 7 [2], of these ions contribute to the strong unresolved transition arrays (UTA) observed in the required 2% bandwidth at 13.5nm [3, 4, 5, 6, 7]. The EUV source being developed at the Laser Plasma Laboratory (LPL), is a laser driven plasma generated from tin-doped droplets that are approximately 35 μm in diameter, as described in previously 7.

8.1.1 Target System and Configuration

The patented source design (US patent 6,862,339) [8] utilizes mass-limited droplets[9] of tin with only enough tin atoms for the required emission [10]. Other key features of this design are the high-repetition rate droplet generation (up to 200 kHz) that can be stably synchronized to the laser pulse generation. Complete ionization of each droplet can be achieved at the end of each laser pulse with this source configuration allowing for low debris plasma generation. The source size is well within the specified etendue limits of 3.3 $mm^2 Sr$[11], and

debris mitigation schemes can be implemented with relative ease as needed [12]. High EUV conversion efficiencies were measured and reported previously, as well [7].

8.2 Fiber Laser System

Currently the field of fiber lasers are under rapid development. Higher powers, new wavelengths, heat dissipation characteristics, and new fibre designs for pulsed and CW applications, poses this class of lasers as a low cost and compact alternative to solid state and gas laser technology. Kilowatt levels of power have already been demonstrated [13]. The fiber laser system used for the studies to be described here is under development at the University of Michigan, at the Center for Ultrafast Optical Sciences (Fig.8.1).

At the front end of the laser is an electric-pulse-driven Fabry-Perot semiconductor laser diode emitting 1064 nm, with which repetition rate, pulse duration and pulse shape can easily manipulated. The entire system is packaged into a cascaded four-stage Master Oscillator Power Amplifier (MOPA) configuration using ytterbium-doped fiber amplifier for the seed pulse amplification to high peak powers (Fig. 8.2. The beam quality of the large effective mode area (2749 μm^2) fiber is improved through coiling and mode matching techniques with measured beam quality at an M^2 of 1.3 [14]. More than 100W of power is possible from this laser, with pulse duration near 5 ns, and 5 mJ of energy per pulse. The capability of this laser system to generate pre-pulses of varying durations and delays with ease is an advantage, since pre-pulse [15, 16] plasmas are reported to improve the efficiency of laser energy to EUV light conversion. EUV generation from solid tin targets utilizing this laser system was demonstrated previously [17]. This study reports the first results of efficient EUV generation obtained by coupling this laser to high repetition rate source operation.

8.3 Experimental Configuration

The vacuum chamber used for these experiments is 45 cm in diameter, with 12 vacuum ports positioned around the chamber at 30° separation. The plasma and EUV diagnostics are set-up on the various ports of the chamber, as needed. For this study, the target is positioned at the center of the chamber and the laser beam is focused with a 60 mm focal length lens mounted inside the chamber. The droplets are situated at the focus of the lens, and the laser beam is normally incident on the droplets (Fig. 8.3). The flat-field spectrometer (FFS) and the narrow band EUV energy detector, both, are placed at 30° on

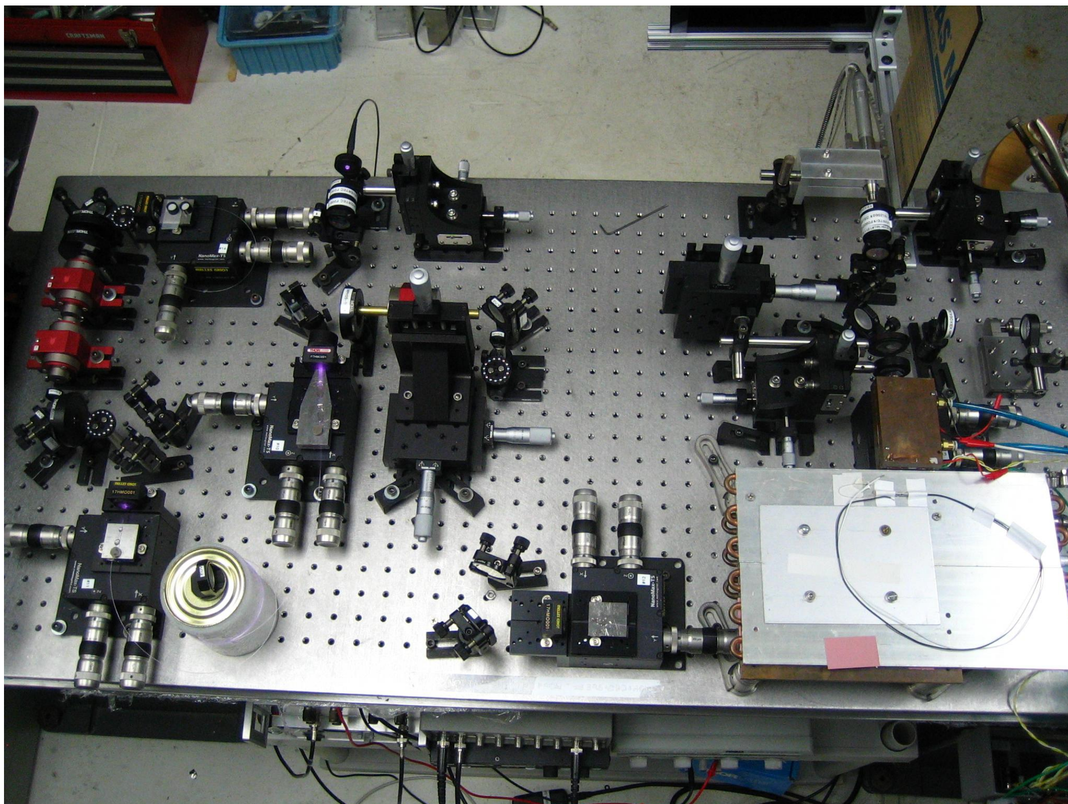

Figure 8.1: The picture of the fiber laser

both sides of the laser beam axis (Fig. 8.3). Droplet generation at a rate of 31 kHz is used for these experiments and the laser pulse is synchronized to the droplet train. The EUV wavelengths are generated under operating pressures better than 10^{-3} Torr.

The flat-field spectrograph (FFS) [18] is used to record spectra from the source for the 13.5 nm mirror bandwidth EUV calibrations. The instrument covers the EUV spectral region from 11 nm-19 nm. Details of the spectrometer design is reported previously [7, 5, 6]. The narrow-band EUV emission from the source is measured with an EUV energy detector known as the Flying Circus (FC) in the source community, developed at the FOM-Institute for Plasma Physics Rijnhuizen [19]. This instrument consists of a calibrated, curved normal incidence Mo-Si MLM, 0.5 μm Zr filter and an AXUV-100G photodiode. The MLM is used to select the wavelength band at approximately 3%, and the Zr filter selects the EUV spectral range. The photodiode enables time resolved and high repetition rate measurements, with a spectral responsivity of 0.24 A/W at 13.5nm. The filter and the MLM used in the experiments were sent to National Institute of Standards and Technology (NIST) in order

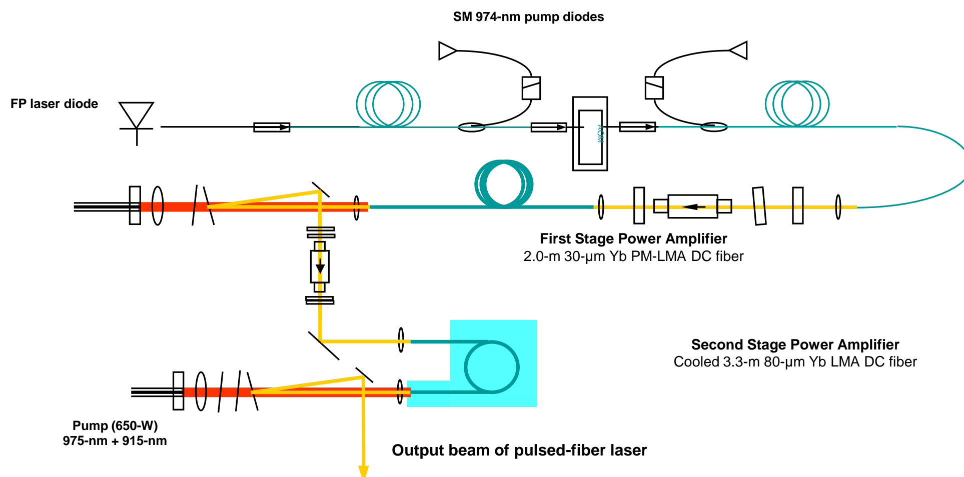

Figure 8.2: Yb-doped fiber laser schematic

to obtain efficiency data for EUV energy calculations. The methods for calculating CE into 2πSr and 2% BW of MLM is described in detail in previously published works [7, 5], as well as in chapter 5. The spectrometer measurements are also cross-calibrated to the FC, making the FFS a calibrated instrument for in-band EUV energy measurements.

For the imaging system, an uncoated BK-7 lens with focal length of 75 mm is used to create a real image on the visible CCD. The imaging lens is placed inside the vacuum chamber while the CCD is outside. A black and white TV monitor is used to observe the image captured by the CCD. The position of the CCD was adjusted to its best position where the sharpest image of the droplets are observed. The total magnification of the system from the droplet to the image on the TV monitor is about 600.

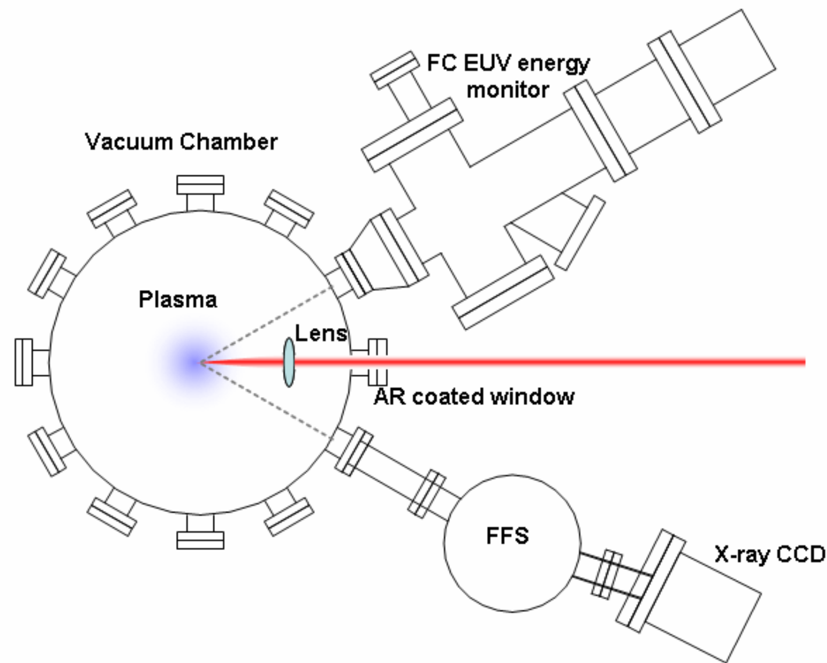

Figure 8.3: Chamber set-up and diagnostics

8.4 Results

8.4.1 Results from pre-plasma generation

A number of laser irradiation conditions were investigated using precision spectroscopy and calibrated metrology. Optimum conditions for generating 13.5 nm emission from the fiber laser and the tin-doped droplet combination was isolated. Each spectral result presented in this paper is an average of approximately 1700 shots. The CCD accumulation duration was set to 1 second. Shorter accumulation times resulted in blurring and smearing of the spectral information requiring additional image processing. Non-linear pixel to wavelength calibrations with respect to the prominent oxygen lines appearing in the spectral measurements were completed for accuracy of the CE calculations. The best spectral and CE results obtained with pre-pulse plasma scale-length optimization is shown in fig. 8.4.

The spectral measurements show tin UTA centered between 13 nm and 15 nm. Four dominant oxygen peaks, O^{5+} emission at 11.6, 12.98, 15.0, and 17.3 nm is seen as well. The typical variations in the tin UTA is seen as the intensity is varied by changing focused beam size, as reported previously [7, 6]. In Fig. 8.4(a), rapid change in the plasma temperature is observed with the change in intensity. Fig. 8.4(b) shows variations in the spectral counts which is thought to be due to minor changes in the laser-droplet target synchronization. This can be improved with a target stabilization system which was not in place for this study. Fig. 8.4(c) shows that at the smallest focus (near 20 μm), the measured efficiency is lower. Fig. 8.4(d) illustrates CE as a function of in laser beam intensity, with best efficiency is obtained for irradiance intensity near 8×10^{10} W/cm^2. At higher beam intensity and smaller focus, CE is seen to drop.

The highest conversion efficiencies measured are at irradiances near 8×10^{10} W/cm^2.

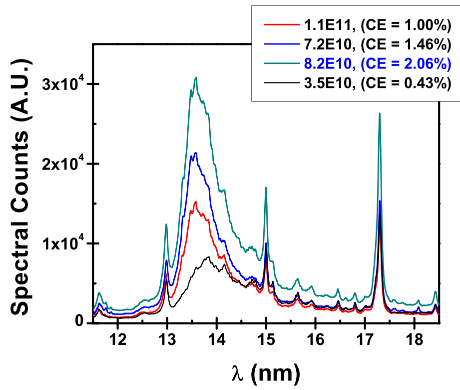

(a) Spectra as a function of intensity for varying laser beam spot size obtained by translating the focusing lens

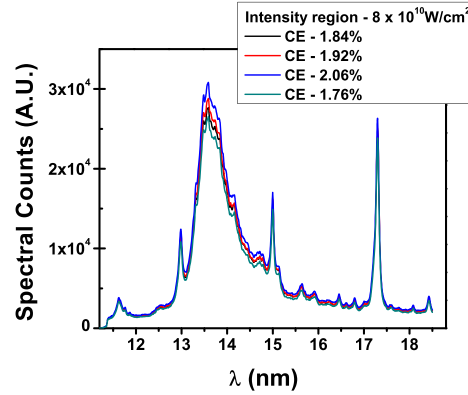

(b) Multiple measurements taken at the best CE condition

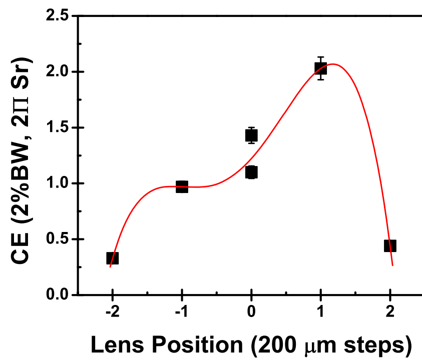

(c) Averaged CE as a function of lens position

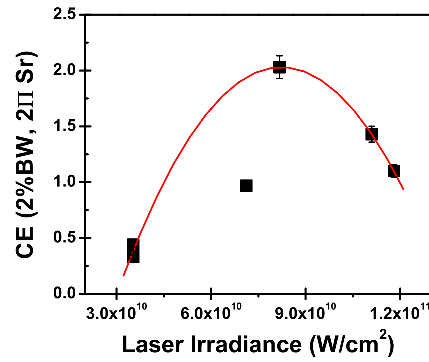

(d) Averaged CE as a function of intensity

Figure 8.4: Best results obtained for 13.5 nm generation from the series of experiments conducted using fiber laser.

The energy per pulse used is 6 mJ and the pulse duration is 6.0 ns. The best CE measurement is 2.1 % into $2\pi\,\mathrm{Sr}/2\%\mathrm{BW}$. To check the repeatability of the results, multiple measurements were taken at each experimental condition, giving the highest averaged CE at 1.9 %. The measurements were obtained with the laser running at 10 W. This is measured before the high power isolator that is in place to remove feedback from plasma/target to

fiber, and the optics directing the beam to the chamber. At the start of the experiment, laser energy at target is 80 % of the energy before the optical path into the chamber. After the experiment the total transmission in chamber through the isolator, mirrors, window and the lens is 51.4%. This drop in the total energy transmission is taken into account in the CE measurements.

8.4.2 Results without pre-plasma generation

To compare how the generation of a pre-plasma affects the EUV generation, a set of measurements without pre-pulse heating of the target was obtained. The results from these energy measurements are shown in Fig. 8.5. In this case, it can be observed from Fig. 8.5(a) that the best result obtained is a CE of 1% near the focus of the lens. This is only half of the highest conversion efficiency obtained for the previous set of measurements. It is interesting to note that we obtained the same CE at the focal region in 8.4(c). Fig. 8.5(b) shows linear increase on CE with increasing laser irradiance.

8.4.3 Effects of laser pulse duration on EUV generation

Another unique characteristic of the fiber laser used here, is the capability for changing the pulse width as needed. For comparison, the previous results and the best result obtained from the short pulse duration is plotted together as shown in Fig. 8.6. Fig. 8.6(a) shows the true spectral results and Fig. 8.6(b) gives the same spectra normalized to the 12.98 nm oxygen peak. Even though, the irradiance intensity is much higher for the short pulse measurement, it does not translate into a high average plasma electron temperature. Thus, the emission levels expected from the target are not measured. A possible explanation

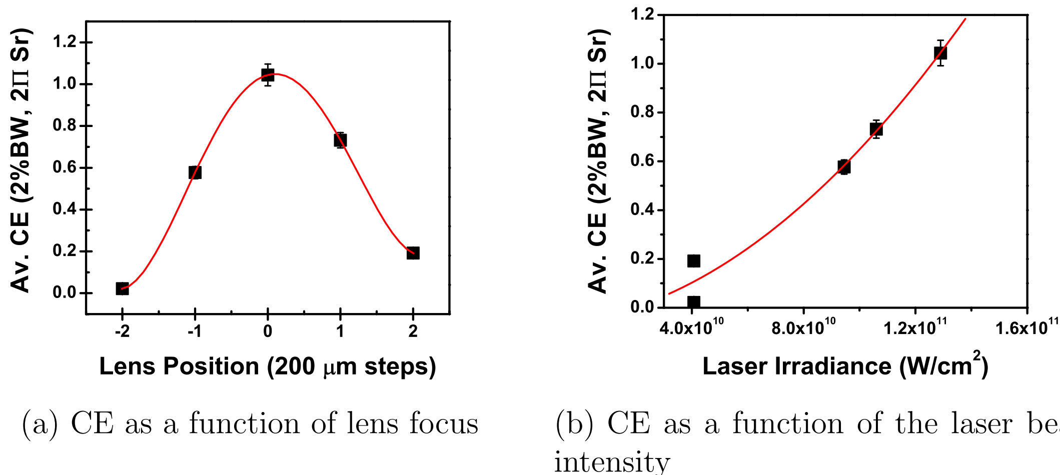

(a) CE as a function of lens focus

(b) CE as a function of the laser beam intensity

Figure 8.5: Energy measurements obtained without the generation of pre-plasma for scale-length optimization. Energies measured are much lower.

could be that the short laser pulse leads to a short laser-plasma interaction lengths. Short scale lengths lead to the inefficient absorption of the laser radiation by the plasma. Further investigation is necessary for conclusive results in this area.

8.4.4 Tin debris on lens

In all of the previous results, in order to attain high laser irradiance intensities, a short focal length lens was used. Short focal lengths provided smaller beam focus. In all of the experiments, large tin particulate deposits on the focusing lens were observed. This leads to a rapid transmission loss during experiments, that is difficult to account for in the CE calculations. Fig. 8.7 is the surface of the lens obtained using a scanning white light interferometer. Large amount Sn debris is observed on the surface.

The focal spot obtained with the short focal length lens is considerably smaller than

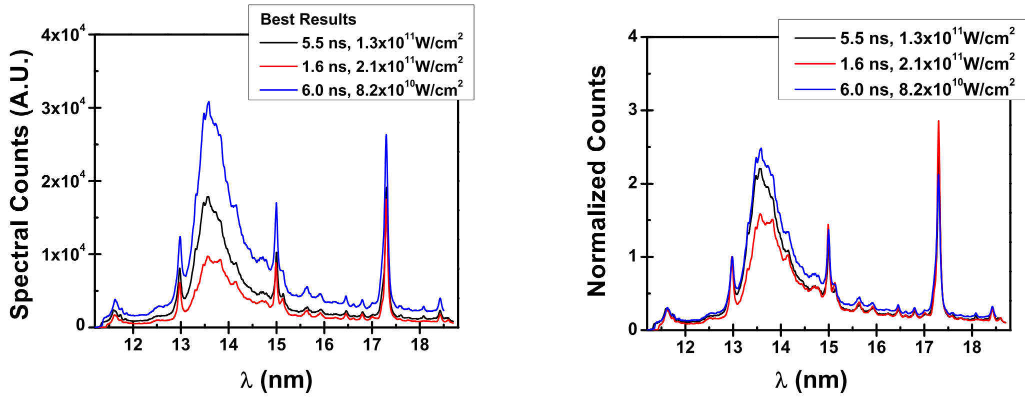

(a) Highest spectral results obtained for different laser pulse widths.

(b) Normalized with 13 nm oxygen line.

Figure 8.6: Comparing the effect of pulse duration on plasma temperature.

the size of the droplet. An explanation for this is that this condition, where there is a smaller spot with low laser energy near 3-5 mJ, fails to ionize the target fully, leading to excess deposits on the optics. It was found that cleaning the lens surface immediately after the experiments preserved the antireflection coating on the lens. Eventually the coating was etched to a point that there were noticeable focal distortions, rendering it unviable for further use. In our previous experiments with laser pulse energies of 100 mJ and a droplet diameter of 35μm, debris is minimized [20].

8.5 Discussion

To produce efficient EUV emission from a source material, it is necessary to ensure conditions for maximum laser energy absorption. Not only that, almost all of the absorbed laser energy needs to be converted into thermal energy capable of producing the required excited states for emission into a given wavelength region. One way to maximize laser absorption is to keep laser irradiance intensities below threshold conditions for creating parametric instabilities in

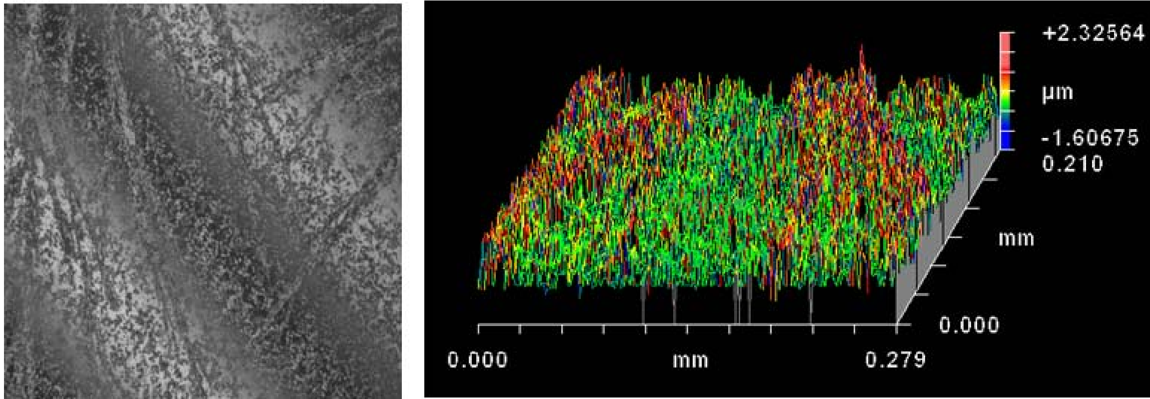

Figure 8.7: Sn particulates deposited on the lens during an experiment with tin droplets.

the plasma.

With the tin-doped droplets and fiber laser, this experimental study demonstrates two results that will impact the EUV source development. First, it can be seen that efficient, high-power, and high repetition rate source operation is possible with fiber lasers. Second, high CE for 13.5 nm can be obtained with low laser energy per pulse as long the plasma scale length is optimized for the required emission. Fig. 8.8 compares the best results obtained with a 1 Hz, 100 mJ, 35 μm spot to the fiber laser best spectra. The spectra is normalized to the oxygen peak at 12.98 nm.

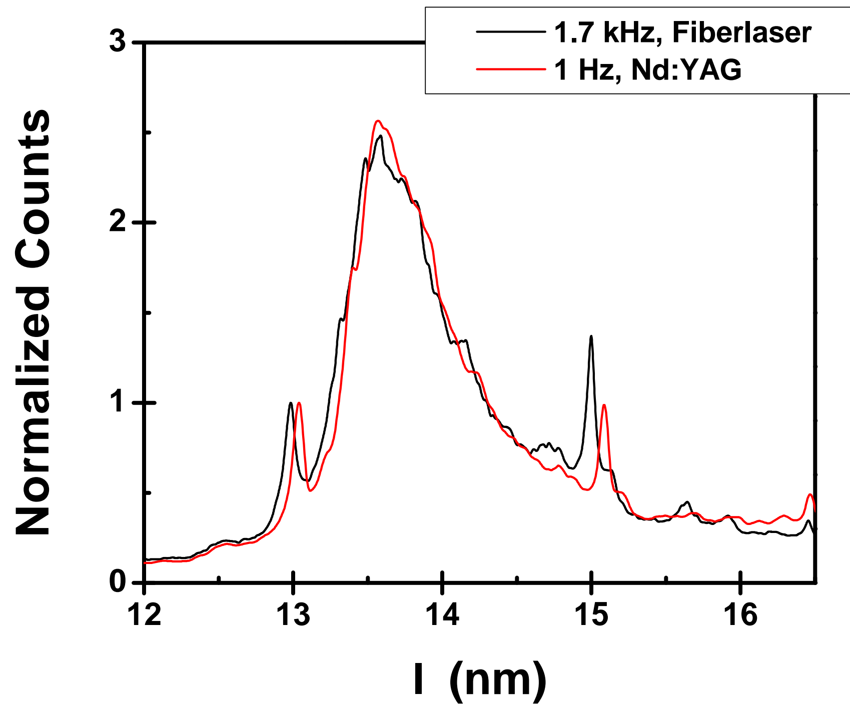

Figure 8.8: Comparison of fiber laser spectral measurement to the highest Nd:YAG laser measurement for the same target

The target conditions are identical, and it can be seen from the Fig. 8.8 that the fiber laser has successfully emulated solid-state laser results, and gives identical CE results near 2.0%. Higher CE is expected with using a target stabilization system and by using smaller droplet sizes that match beam focal diameter. Droplet diameters that match the laser beam spot size is also expected to reduce the debris produced during plasma generation as well.

8.6 References

[1] Winnie Svendsen and Gerard O'Sullivan. Statistics and characteristics of xuv transition arrays from laser-produced plasmas of the elements tin through iodine. *Phys. Rev. A*,

50(5):3710–3718, Nov 1994.

[2] M. Al-Rabban. Term structure of 4d-electron configurations and calculated spectrum in sn-isonuclear sequence. *J. Quant. Spec. and Rad. Trans.*, 97:278–316, 2006.

[3] David J. Nagel, Charles M. Brown, M. C. Peckerar, Marshall L. Ginter, J. A. Robinson, Thomas J. McIlrath, and P. K. Carroll. Repetitively pulsed-plasma soft x-ray source. *Appl. Opt.*, 23(9):1428, 1984.

[4] R. C. Spitzer, T. J. Orzechowski, D. W. Phillion, R. L. Kauffman, and C. Cerjan. Conversion efficiencies from laser-produced plasmas in the extreme ultraviolet regime. *Journal of Applied Physics*, 79(5):2251–2258, 1996.

[5] Chiew-Seng Koay. *Radiation studies of the tin-doped microscopic droplet laser plasma light source specific to EUV lithography.* PhD thesis, University of Central Florida, CREOL & FPCE: The College of Optics and Photonics, 2005.

[6] Simi A. George, William Silfvast, Kazutoshi Takenoshita, Robert Bernath, Chiew-Seng Koay, Greg Shimkaveg, Martin Richardson, Moza Al-Rabban, and Howard Scott. Euv generation from lithium laser plasma for lithography. volume 6151, page 615143. SPIE, 2006.

[7] Scott Mackay, editor. *High conversion efficiency microscopic tin-doped droplet target laser-plasma source for EUVL*, volume 5751 of *Proc. SPIE*, 2005.

[8] Martin C. Richardson. Micro-droplet plasmas, March 2005.

[9] F. Jin and M. Richardson. New laser plasma source for extreme-ultraviolet lithography. *Appl. Opt.*, 34(25):5750, 1995.

[10] M. Richardson, C.-S. Koay, K. Takenoshita, C. Keyser, and M. Al-Rabban. High conversion efficiency mass-limited sn-based laser plasma source for extreme ultraviolet lithography. *Journal of Vacuum Science and Technology B: Microelectronics and Nanometer Structures*, 22(2):785–790, 2004.

[11] Vivek Bakshi, editor. *EUV Sources for Lithography.* SPIE Press, Washington, 2005.

[12] Kazutoshi Takenoshita, Chiew-Seng Koay, Somsak Teerawattansook, Martin Richardson, and Vivek Bakshi. Debris characterization and mitigation from microscopic laser-plasma tin-doped droplet euv sources. volume 5751, pages 563–571. SPIE, 2005.

[13] Jeff Hecht. Photonic frontiers: High-power fiber lasers: Pumping up the power. Technical report, `http://www.laserfocusworld.com/articles/article_display.html?id=234077`, 2007.

[14] K-C. Hou. Multi-mw peak power scaling of single-transverse mode pulses using 80-m core yb-doped lma fibers. presented in Post Deadline Paper session at Advanced Solid-State Photonics, 2006.

[15] S. Düsterer, H. Schwoerer, W. Ziegler, C. Ziener, and R. Sauerbrey. Optimization of EUV radiation yield from laser-produced plasma. *Applied Physics B: Lasers and Optics*, 73:693–698, 2001.

[16] P. Dunne, G. O'Sullivan, and D. O'Reilly. Prepulse-enhanced narrow bandwidth soft x-ray emission from a low debris, subnanosecond, laser plasma source. *Applied Physics Letters*, 76:34–+, January 2000.

[17] Aghapi G. Mordovanakis, Kai-Chung Hou, Yu-Chung Chang, Ming-Yuan Cheng, John Nees, Bixue Hou, Anatoly Maksimchuk, Gerard Mourou, Almantas Galvanauskas, and

Bruno Lafontaine. Demonstration of fiber-laser-produced plasma source and application to efficient extreme uv light generation. *Opt. Lett.*, 31(17):2517–2519, 2006.

[18] Tatsuo Harada and Toshiaki Kita. Mechanically ruled aberration-corrected concave gratings. *Appl. Opt.*, 19(23):3987–, 1980.

[19] R. Stuik, F. Scholze, J. Tummler, and F. Bijkerk. Absolute calibration of a multilayer-based xuv diagnostic. *Nucl. Instrum. Methods*, 492:305–316, 2002.

[20] Kazutoshi Takenoshita. *Debris characterization and mitigation of droplet laser plasma sources for EUV lithography.* PhD thesis, University of Central Florida, Department of Electrical Enigineering and Computer Engineering, 2006.

CHAPTER 9
CONCLUSION AND FUTURE WORK

9.1 Summary

A compact laboratory light source that is capable generating clean EUV light (only the needed bandwidths) at high repetition rates is necessary for advancing scientific explorations in the region near the atomic resonances of many materials. High reflectivity MLMs and zone plate lenses for the 13.5 nm wavelength have been demonstrated by researchers. In this thesis, materials and methods for developing a high power, 13.5 nm light source from laser-produced plasmas are extensively investigated. The generation and optimization of EUV emission from planar tin and lithium targets and tin-doped droplet targets were presented. Interpretation of the spectral data was completed using calculations and simulations.

The first studies were conducted of a solid Sn laser-produced plasmas. Planar tin slab target and a Nd:YAG, 1 Hz laser with a pulse duration of 11.5 ns were used. The highest, calibrated conversion efficiency in to the narrow Mo-Si MLM bandwidth was measured to be at 4.889% which corresponds to a laser power density calculated to be near 1.2×10^{11}W/cm^2.

The second set of studies compared EUV emission from two different source materials, the low-Z lithium and the high-Z tin target. At 13.5 nm, the best conversion efficiency for lithium was found to be 2.2% at intensities near 7×10^{10} W/cm^2. The EUV emission from lithium is due to the H-like transition line originating from Li^{2+}(1s-2p). The highest CE measured for tin was near 5.0% at an intensity region close to 1×10^{11} W/cm^2. The Sn and Li atomic structures of the open shells of ions contributing to the 13 nm EUV emission

were calculated. Calculations using a CRE model for various ion densities provide us with average charge state populations and temperatures existing in the plasma for experimental comparisons. The dynamics of the plasma expansion was modeled using 1D-codes for both targets.

To meet the industry requirements for an efficient, low debris EUV source, LPL is developing a laser plasma based on a tin-doped droplet target. The droplet configuration utilizes the mass-limited concept with complete ionization resulting in low debris, and can be extended easily to high repetition rates. Chapter 7 presents the characterization and optimization of the EUV emission from the tin-doped droplet laser-plasma source using spectroscopy. CE of 2.25% is obtained for irradiance intensities in the region of $1-2\times10^{11}$ W/cm^2.

An extensive survey of the source's spectrum was achieved from 2 nm to 2.5 μm which covers the region of interest in the electromagnetic spectrum. The source conversion efficiencies are characterized under various laser irradiation conditions using calibrated metrology. Experimental conditions are modeled to determine the electron temperature and density conditions of the plasma state. The highest conversion efficiency for the 1 Hz laser measured is 2.25% [1]. The size of the plasma was characterized and was determined to be safely within the etendue limit set by the optical elements in the EUVL [1].

A comprehensive study of the spectral and Mo-Si mirror in-band EUV emission from tin-doped droplet laser plasma targets irradiated with a single 1064 nm beam from an Yb:doped fiber laser is also reported. With pre-pulse enhancement, in-band conversion efficiency of approximately 2.1% is measured for laser irradiance intensities near 8×10^{10} W/cm^2. This is the first study to be reported that uses a high-power, high repetition rate fiber laser with the high repetition rate droplet targets for measurements EUV generation.

By using pre-pulse enhancement, high EUV yields were demonstrated from the very small energy per pulse of the fiber laser.

For taking the source development to real applications, high power demonstrations were completed using high-repetition rate Nd:YAG laser and the tin-doped droplets targets. Two commercially available, high-repetition rate, Nd:YAG lasers from POWERLASE were temporally multiplexed and coupled to the tin droplets. 23 W of average EUV power into the Mo-Si multilayer mirror bandwidth was demonstrated at source from the tin-doped droplets [2].

Numerous studies are still needed in order to fully evaluate EUV generation from Sn planar and droplet targets. Calculations completed by other researchers have shown that Sn EUV emission can be Improved considerable by using longer wavelength laser beams. Studies of this are being planned with CO_2 laser with a wavelength of 10 μm. The spatial and temporal evolution of the plasma for all targets are very important to fundamental studies. Pinhole imaging and interferometries can give details about the electron density evolution of the plasma. Improved modeling is also planned for better interpretation of spectral data and this is under way. Calibrated emissions from the source into all wavelengths are also being planned. The spectral region from 20 nm - 120 nm is very difficult to measure. A higher resolution spectrometer that is capable of detecting spectral information from the plasma sources in this region was designed and its installation on a vacuum chamber is currently complete. Measurements using this spectrometer will provide high resolution spectral information in the longer EUV region, which has never been completed.

The real future of this EUV source development depends on its applicability to science and technology. Thus, future work includes using the light source for microcopy in the laboratory and for lithography in the high volume manufacturing of computer chips.

9.2 References

[1] Chiew-Seng Koay. *Radiation studies of the tin-doped microscopic droplet laser plasma light source specific to EUV lithography.* PhD thesis, University of Central Florida, CREOL & FPCE: The College of Optics and Photonics, 2005.

[2] Kazutoshi Takenoshita, Simi A. George, Tobias Schmid, Chiew-Seng Koay, Jose Cunado, Robert Bernath, Christopher Brown, Moza M. Al-Rabban, William T. Silfvast, and Martin C. Richardson. Characterization of the tin-doped droplet laser plasma euvl sources for hvm. volume 6517, page 65173O. SPIE, 2007.

APPENDIX
LIST OF PAPERS

1. S. A. George, K-C Hou, K. Takenoshita, A. Galvanauskas, and M. C. Richardson. 13.5 nm EUV generation from tin-doped droplets using a Fiber Laser. Optics Express, Volume 15, No. 25 (2007).

2. S. A. George, W. T. Silfvast, K. Takenoshita, R. Bernath, C-S Koay, G. Shimkaveg, and M. C. Richardson. Comparative EUV emission measurements for Li and Sn laser plasmas. Optics Letters, Volume 32, Issue 8, pp. 997-999 (2007).

3. K. Takenoshita, S. A. George, T. Schmid, C-S. Koay, J. Cunado, M. Richardson, et. al. Characterization of the Tin-doped droplet laser plasma EUVL sources for HVM. Proc. SPIE, Volume 6517 (2007).

4. S. A. George, M. Al-Rabban,, G. Shimkaveg, W. Silfvast, C-S. Koay, K. Takenoshita, R. Bernath, M. Richardson, H. Scott. EUV generation from lithium laser plasma for lithography. Proc. SPIE, Volume 6151, pp. 1051-1058 (2006).

5. Martin C. Richardson, Chiew-Seng Koay, Kazutoshi Takenoshita, Christian Keyser, Simi A. George, Moza Mohammad Al-Rabban, Vivek Bakshi, Laser plasma EUV sources based on droplet target technology, EUV Sources for Lithography. Ed: Vivek Bakshi, SPIE Press, Chapter 26, pp. 687-718 (2006).

6. S. A. George, C-S. Koay, K. Takenoshita, R. Bernath, M. Al-Rabban, C. Keyser, V. Bakshi, H. Scott, M. Richardson. EUV spectroscopy of mass-limited Sn-doped laser microplasmas. Proc. SPIE, Volume 5751, pp. 798-807 (2005).

7. M. Al-Rabban, S. A. George, C. Keyser, H. Scott, V. Bakshi, M. C. Richardson. Radiation transport modeling for Xe and Sn-doped droplet laser-plasma sources. Proc. SPIE, Volume 5751, pp. 769-778 (2005)

8. C-S. Koay, S. A. George, K.Takenoshita, R. Bernath, E. Fujiwara, M. C. Richardson, V. Bakshi, High conversion efficiency microscopic tin-doped droplet target laser-plasma source for EUVL. Proc. SPIE, Volume 5751 (2005).

9. K. Takenoshita, C-S. Koay, S. A.George, S. Teerawattanasook, M.C. Richardson, V. Bakshi. Ion emission measurements and mirror erosion studies for extreme ultraviolet lithography. J.Vac. Sci. and Tech. B, Volume 23, 6. pp. 2879-2884 (2005).

10. M. C. Richardson, C.-S. Koay, K. Takenoshita, S. A. George, R. Bernath, M. Al-Rabban, V.Bakshi, Efficient 13.5 nm EUV generation from a laser plasma. Quantum Electronics and Laser Science (QELS), Volume 3, pp. 1947- 1949 (2005).

11. M. C. Richardson, C.-S. Koay, K. Takenoshita, C. Keyser, R. Bernath, S. A. George, S. Teerawattanasook, Diagnostics for laser plasma EUV sources. Proc. of SPIE, Volume 5580, pp. 434-442 (2005).

12. M. C. Richardson, C.-S. Koay, K. Takenoshita, C. Keyser, S. A. George, S. Teerawattanasook, M. Al-Rabban, H. Scott. Laser plasma EUVL sources - progress and challenges, Proc. SPIE, Volume 5374, pp. 447-453 (2004).

References

[1] David Attwood. *Soft X-rays and Extreme Ultraviolet Radiation: Principles and Applications*. Cambridge University Press, Berkeley, 1999.

[2] Eric Gullikson. Multilayer reflectivity. Technical report, http://henke.lbl.gov/optical_constants/, 2007.

[3] Peter Kürz. The euv optics development program at carl zeiss smt ag. Technical report, http://www.sematech.org/meetings/archives/litho/euvl/20030930/presentations/8A%20P%20Kurz%20EUV%20Symp.pdf, 2003.

[4] How is synchrotron light created? Technical report, http://www.synchrotron.vic.gov.au/content.asp?Document_ID=97, 2004.

[5] J. Davis, R. Clark, M. Blaha, and J.L. Giuliani. Atomic physics and non-lte effects. *Laser and Particle Beams*, 19:557–577, October 2001.

[6] Gerry O'Sullivan. Modelling euv atomic emission from xe and sn plasmas with available atomic structure and plasma codes. Presentation at EUVL Source Modelling Workshop, Antwerp, Sept. 28th 2003.

[7] Moza Al-Rabban, Christian Keyser, Simi George, Howard Scott, Vivek Bakshi, and Martin Richardson. Radiation transport modeling for xe and sn-doped droplet laser-plasma sources. volume 5751, pages 769–778. SPIE, 2005.

[8] M. Al-Rabban. Term structure of 4d-electron configurations and calculated spectrum in sn-isonuclear sequence. *J. Quant. Spec. and Rad. Trans.*, 97:278–316, 2006.

[9] Chiew-Seng Koay. *Radiation studies of the tin-doped microscopic droplet laser plasma light source specific to EUV lithography.* PhD thesis, University of Central Florida, CREOL & FPCE: The College of Optics and Photonics, 2005.

[10] Harvey Elliot White. *Introduction to Atomic Spectra.* McGraw-Hill Book Company, New York, first edition, 1934.

[11] R. Stuik, F. Scholze, J. Tummler, and F. Bijkerk. Absolute calibration of a multilayer-based xuv diagnostic. *Nucl. Instrum. Methods*, 492:305–316, 2002.

[12] Howard Scott. *CRETIN User's Manual.* Lawrence Livermore National Laboratory, 2001. UCRL-MA-124173.

[13] Simi A. George, William Silfvast, Kazutoshi Takenoshita, Robert Bernath, Chiew-Seng Koay, Greg Shimkaveg, Martin Richardson, Moza Al-Rabban, and Howard Scott. Euv generation from lithium laser plasma for lithography. volume 6151, page 615143. SPIE, 2006.

[14] James A. R. Samson. *Techniques of Vacuum Ultraviolet Spectrosocpy.* John Wiley and Sons, Inc., New York, first edition, 1967.

[15] Carolyn A. Larabell and Mark A. Le Gros. X-ray Tomography Generates 3-D Reconstructions of the Yeast, Saccharomyces cerevisiae, at 60-nm Resolution. *Mol. Biol. Cell*, 15(3):957–962, 2004.

[16] Max Born and Emil Wolf. *Principles of Optics: Electromagnetic Theory of Propagation, Interference and Diffraction of Light.* Pergamon Press, New York, sixth edition, 1980.

[17] Mark Fox. *Optical Properties of Solids.* Oxford University Press, New York, first edition, 2001.

[18] E. M. Gullikson. Optical properties of materials. In *Vacuum Ultraviolet Spectroscopy I*, chapter 13, pages 257–270. Academic Press, New York, 1998.

[19] B. L. Henke, E. M. Gullikson, and J. C. Davis. X-ray interactions: photoabsorption, scattering, transmission, and reflection at e=50-30000 ev, z = 1-92. *Atomic Data and Nuclear Data Tables*, 54(2):181–342, July 1993.

[20] James A. Samson and David L. Ederer. *Vacuum Ultraviolet Spectroscopy I.* Academic Press, San Diego, 1972.

[21] John David Jackson. *Classical Electrodynamics.* John Wiley & Sons, Inc., New York, third edition, 1999.

[22] Eugene Hecht. *Optics.* Pearson/Addison Wesley, New York, fourth edition, 2002.

[23] Alan G. Michette. *Optical systems for soft x-rays.* Plenum Press, New York, first edition, 1986.

[24] A. V. Vinogradov and B. Ya Zeldovich. X-ray and far-uv multilayer mirrors: Principles and possibilities. *Applied Optics*, 16:89, 1977.

[25] Sasa Bajt, Jennifer B. Alameda, Troy W. Barbee Jr., W. Miles Clift, James A. Folta, Ben Kaufmann, , and Eberhard A. Spiller. Improved reflectance and stability of mo-si multilayers. *Optical Engineering*, 41(8):17971804, 2002.

[26] E Meltchakov, V Vidal, H Faik, M-J Casanove, and B Vidal. Performance of multilayer coatings in relationship to microstructure of metal layers. characterization and optical

properties of mo/si multilayers in extreme ultra-violet and x-ray ranges. *Journal of Physics: Condensed Matter*, 18(13):3355–3365, 2006.

[27] A. I. Erko, V. V. Aristov, and B. Vidal. *Diffraction X-ray Optics*. Institute of Physics Publishing, Philadelphia, 1996.

[28] Eberhard Spiller. *Soft X-ray Optics*. SPIE Optical Engineering Press, Washington, first edition, 1994.

[29] D. Hambach and G. Schneider. High aperture diffractive x-ray and extreme ultraviolet optical elements for microscopy and lithography applications. volume 17, pages 3212–3216. AVS, 1999.

[30] Weilun Chao, Bruce D. Harteneck, J. Alexander Liddle, Erik H. Anderson, and David T. Attwood. Soft x-ray microscopy at a spatial resolution better than 15 nm. *Nature*, 435(7046):1210 – 1213, 2005.

[31] Dong-Hyun Kim, Peter Fischer, Weilun Chao, Erik Anderson, Mi-Young Im, Sung-Chul Shin, and Sug-Bong Choe. Magnetic soft x-ray microscopy at 15 nm resolution probing nanoscale local magnetic hysteresis (invited). volume 99, page 08H303. AIP, 2006.

[32] A. Miyake, H. Kanazawa, V. Banine, and K. Suzuki. "joint requirements". "Presentation at EUV Workshop, Proceedings available at www.sematech.org", "October 19. 2006".

[33] Vivek Bakshi, editor. *EUV Sources for Lithography*. SPIE Press, Washington, 2005.

[34] E. Di Fabrizio. Fermi project: diffractive optics, microscopy and euv lithography. Technical report, `http://www.frielektronlaser.se/Docs/FERMI/SCDiFabrizio.pdf`, 2004.

[35] Pierre Jaeglé. *Coherent Sources of XUV Radiation: Soft X-ray Laser and High-Order Harmonic Generation*. Springer, New York, first edition, 2006.

[36] Göran Johansson. *Compact Soft X-Ray Microscopy*. PhD thesis, Royal Institute of Technology, Department of Physics, 2003.

[37] Stuart Bowyer. Continuous emission source covering the 50-300-a band. *Appl. Opt.*, 32(34):6930, 1993.

[38] David S. Finley, Stuart Bowyer, Francesco Paresce, and Roger F. Malina. Continuous discharge penning source with emission lines between 50 a and 300 a. *Appl. Opt.*, 18(5):649, 1979.

[39] J. Cao, F. Li, L. Qian, B. Chen, Y. Ma, and X. Chen. Penning discharge vuv and soft x-ray source. In J. P. Knauer and G. K. Shenoy, editors, *Proc. SPIE Vol. 1345, p. 71-77, Advanced X-Ray/EUV Radiation Sources and Applications, James P. Knauer; Gopal K. Shenoy; Eds.*, volume 1345 of *Presented at the Society of Photo-Optical Instrumentation Engineers (SPIE) Conference*, pages 71–77, January 1991.

[40] Kellogg E. M., Wargelin B. J., Norton T. J., Eng R., and Kolodziejczak J. J. Penning source for calibration of x-ray and euv optics and spectrometers at wavelengths as short as 50 a. In R. B. Hoover and A. B. Walker, editors, *Proc. SPIE Vol. 2515, p. 418-419, X-Ray and Extreme Ultraviolet Optics, Richard B. Hoover; Arthur B. Walker; Eds.*,

volume 2515 of *Presented at the Society of Photo-Optical Instrumentation Engineers (SPIE) Conference*, pages 418–419, June 1995.

[41] D. C. Ockwell, N. C. E. Crosland, and V. C. Kempson. Synchrotron light as a source for extreme ultraviolet lithography. volume 17, pages 3043–3046. AVS, 1999.

[42] W. B. Colson. Theory of a free electron laser. *Physics Letters A*, 59(3):187–190, 29 November 1976.

[43] D. A. G. Deacon, L. R. Elias, J. M. J. Madey, G. J. Ramian, H. A. Schwettman, and T. I. Smith. First operation of a free-electron laser. *Phys. Rev. Lett.*, 38(16):892–894, Apr 1977.

[44] G. Ramian. Free electron laser: The world wide web virtual library: Free electron laser research and applications. Technical report, `http://sbfel3.ucsb.edu/www/vl_fel.html`, 2006.

[45] Francis F. Chen. *Introduction to Plasma Physics.* Plenum Press, New York, first edition, 1974.

[46] Marc A. Klosner. *Intense capillary dischrge plasma extreme-ultraviolet sources for EUV lithography and other EUV imaging applications.* PhD thesis, University of Central Florida, CREOL & FPCE: The College of Optics and Photonics, 1998.

[47] W. T. Silfvast, M. Klosner, G.M. Shimkaveg, H. Bender, G.D. Kubiak, and N. Fornaciari. High-power plasma discharge source at 13.5 nm and 11.4 nm for EUV lithography. In Y. Vladimirsky, editor, *Proc. SPIE Vol. 3676, p. 272-275, Emerging Lithographic Technologies III, Yuli Vladimirsky; Ed.*, volume 3676 of *Presented at the Society of*

Photo-Optical Instrumentation Engineers (SPIE) Conference, pages 272–275, June 1999.

[48] M. A. Klosner, H. A. Bender, W. T. Silfvast, and J. J. Rocca. Intense plasma discharge source at 13.5 nm for extreme-ultraviolet lithography. *Opt. Lett.*, 22(1):34–36, 1997.

[49] Malcolm McGeoch. Radio-frequency-preionized xenon z-pinch source for extreme ultraviolet lithography. *Appl. Opt.*, 37(9):1651–1658, 1998.

[50] Vladimir M Borisov, Aleksander V Eltsov, Aleksander S Ivanov, Yuriy B Kiryukhin, Oleg B Khristoforov, Valentin A Mishchenko, Aleksander V Prokofiev, Aleksander Yu Vinokhodov, and Vladimir A Vodchits. Euv sources using xe and sn discharge plasmas. *Journal of Physics D: Applied Physics*, 37(23):3254–3265, 2004.

[51] Klaus Bergmann, Guido Schriever, Oliver Rosier, Martin Müller, Willi Neff, and Rainer Lebert. Highly repetitive, extreme-ultraviolet radiation source based on a gas-discharge plasma. *Appl. Opt.*, 38(25):5413–5417, 1999.

[52] I V Fomenkov, N Böwering, C L Rettig, S T Melnychuk, I R Oliver, J R Hoffman, O V Khodykin, R M Ness, and W N Partlo. Euv discharge light source based on a dense plasma focus operated with positive and negative polarity. *Journal of Physics D: Applied Physics*, 37(23):3266–3276, 2004.

[53] Howard A. Bender III. *Analysis of the operation and plasma dynamics of extreme-ultraviolet and soft x-ray lasers*. PhD thesis, University of Central Florida, Department of Physics, 1998.

[54] Hiroyuki Daido. Review of soft x-ray laser researches and developments. *Reports on Progress in Physics*, 65(10):1513–1576, 2002.

[55] D. L. Matthews, P. L. Hagelstein, M. D. Rosen, M. J. Eckart, N. M. Ceglio, A. U. Hazi, H. Medecki, B. J. MacGowan, J. E. Trebes, B. L. Whitten, E. M. Campbell, C. W. Hatcher, A. M. Hawryluk, R. L. Kauffman, L. D. Pleasance, G. Rambach, J. H. Scofield, G. Stone, and T. A. Weaver. Demonstration of a soft x-ray amplifier. *Phys. Rev. Lett.*, 54(2):110–113, Jan 1985.

[56] J. J. Rocca, E. C. Hammarsten, E. Jankowska, J. Filevich, M. C. Marconi, S. Moon, and V. N. Shlyaptsev. Application of extremely compact capillary discharge soft x-ray lasers to dense plasma diagnostics. *Physics of Plasmas*, 10(5):2031–2038, 2003.

[57] B. R. Benware, C. D. Macchietto, C. H. Moreno, and J. J. Rocca. Demonstration of a high average power tabletop soft x-ray laser. *Phys. Rev. Lett.*, 81(26):5804–5807, Dec 1998.

[58] P. M. Paul, E. S. Toma, P. Breger, G. Mullot, F. Auge, Ph. Balcou, H. G. Muller, and P. Agostini. Observation of a Train of Attosecond Pulses from High Harmonic Generation. *Science*, 292(5522):1689–1692, 2001.

[59] Tenio Popmintchev, Michael E. Grisham, David M. Gaudiosi, Brendan A. Reagan, Oren Cohen, Mark A. Berrill, Margaret M. Murnane, Henry C. Kapteyn, and Jorge J. Rocca. Enhanced high harmonic generation in xe, kr and ar using a capillary discharge. In *Conference on Lasers and Electro-Optics/Quantum Electronics and Laser Science Conference and Photonic Applications Systems Technologies*, page JFA3. Optical Society of America, 2007.

[60] Donna J. O'Connell. Characterization of a lithium laser produced plasma at 135 å

for extreme ultraviolet projection lithography. Master's thesis, University of Central Florida, CREOL & FPCE: The College of Optics and Photonics, 1994.

[61] Paddy Hayden, Anthony Cummings, Nicola Murphy, Gerry O'Sullivan, Paul Sheridan, John White, and Padraig Dunne. 13.5 nm extreme ultraviolet emission from tin based laser produced plasma sources. *Journal of Applied Physics*, 99(9), 2006.

[62] Björn A M Hansson and Hans M Hertz. Liquid-jet laser plasma extreme ultraviolet sources: from droplets to filaments. *Journal of Physics D: Applied Physics*, 37(23):3233–3243, 2004.

[63] S. Bollanti, F. Bonfigli, E. Burattini, P. Di Lazzaro, F. Flora, A. Grilli, T. Letardi, N. Lisi, A. Marinai, L. Mezi, D. Murra, and C. Zheng. High-efficiency clean euv plasma source at 1030 nm, driven by a long-pulse-width excimer laser. *Applied Physics B: Lasers and Optics*, 76(3):277–, 2003.

[64] S. Namba, S. Fujioka, H. Nishimura, Y. Yasuda, K. Nagai, N. Miyanaga, Y. Izawa, K. Mima, and K. Takiyama. Spectroscopic study of debris mitigation with minimum-mass sn laser plasma for extreme ultraviolet lithography. *Applied Physics Letters*, 88(17):171503, 2006.

[65] T. Auguste, F. de Gaufridy de Dortan, T. Ceccotti, J. F. Hergott, O. Sublemontier, D. Descamps, and M. Schmidt. Numerical study of nanosecond laser interactions with micro-sized single droplets and sprays of xenon. *Journal of Applied Physics*, 101(4):043302, 2007.

[66] M. Richardson, C.-S. Koay, K. Takenoshita, C. Keyser, and M. Al-Rabban. High conversion efficiency mass-limited sn-based laser plasma source for extreme ultravio-

let lithography. *Journal of Vacuum Science and Technology B: Microelectronics and Nanometer Structures*, 22(2):785–790, 2004.

[67] Martin Richardson, David Torres, Chris DePriest, Feng Jin, and Gregory Shimkaveg. Mass-limited, debris-free laser-plasma euv source. *Optics Communications*, 145:109–112, 1998.

[68] Christian Keyser. *Optical and spectral characterization of the water droplet laser plasma EUV source*. PhD thesis, University of Central Florida, Department of Physics, 1994.

[69] Kazutoshi Takenoshita. *Debris characterization and mitigation of droplet laser plasma sources for EUV lithography*. PhD thesis, University of Central Florida, Department of Electrical Enigineering and Computer Engineering, 2006.

[70] F. Jin and M. Richardson. New laser plasma source for extreme-ultraviolet lithography. *Appl. Opt.*, 34(25):5750, 1995.

[71] R. C. Spitzer, T. J. Orzechowski, D. W. Phillion, R. L. Kauffman, and C. Cerjan. Conversion efficiencies from laser-produced plasmas in the extreme ultraviolet regime. *Journal of Applied Physics*, 79(5):2251–2258, 1996.

[72] H. C. Gerritsen, H. van Brug, F. Bijkerk, and M. J. van der Wiel. Laser-generated plasma as soft x-ray source. *Journal of Applied Physics*, 59(7):2337–2344, 1986.

[73] Robert J. Goldston and Paul H. Rutherford. *Introduction to Plasma Physics*. Institute of Physics Publishing, Philadelphia, first edition, 1995.

[74] William L. Kruer. *The Physics of Laser Plasma Interactions*. Westview Press, Colorado, 2003.

[75] L. Spitzer. *Physics of Fully Ionized Gases*. Interscience, New York, second edition, 1962.

[76] I. C. E. Turcu and J. B. Dance. *X-rays from Laser Plasmas: Generation and Applications*. Wiley, New York, first edition, 1999.

[77] Danilo Giulietti and Leonida A. Gizzi. X-ray emission from laser produced plasmas. *La Rivista del Nuovo Cimento*, 21(10):1–93, 1998.

[78] John M. Dawson. On the production of plasma by giant pulse lasers. *Physics of Fluids*, 7(7):981–987, 1964.

[79] Tudor Wyatt Johnston and John M. Dawson. Correct values for high-frequency power absorption by inverse bremsstrahlung in plasmas. *Physics of Fluids*, 16(5):722–722, 1973.

[80] H. A. Baldis, E. M. Campbell, and W. L. Kruer. Laser-plasma interactions. In *Physics of Laser Plasma*, chapter 9, pages 361–435. North-Holland, New York, 1991.

[81] J. P. Christiansen, D. E. T. F. Ashby, , and K. V. Roberts. Medusa - a one-dimensional laser fusion code. *Comput. Phys. Commun.*, 7:271, 1974.

[82] A. Djaoui. *A User Guide for the Laser-Plasma Simulation Code: MED103*. The Central Laboratory of the Research Councils, Rutheford Appleton Laboratory, Oxfordshire, 1996. Technical Report RAL-TR-96-099.

[83] A. Djaoui and A. A. Offenberger. Heating of underdense plasmas by intense short-pulse lasers. *Phys. Rev. E*, 50(6):4961–4968, Dec 1994.

[84] A. Djaoui and S. J. Rose. Calculation of the time-dependent excitation and ionization in a laser-produced plasma. *Journal of Physics B: Atomic, Molecular and Optical Physics*, 25(11):2745–2762, 1992.

[85] Hans R. Griem. *Plasma Spectroscopy.* McGraw-Hill Book Company, New York, 1964.

[86] Hans R. Griem. *Principles of Plasma Spectroscopy.* Cambridge University Press, New York, 1997.

[87] Hans R. Griem. *Spectral Line Broadening by Plasmas.* Academic Press, New York, 1974.

[88] Takashi Fujimoto. *Plasma Spectroscopy.* Clarendon Press, Oxford, 2004.

[89] David Salzmann. *Atomic Physics in Hot Plasmas.* Oxford University Press, New York, 1998.

[90] V. P. Shevelko and L. A. Vainshtein. *Atomic Physics for Hot Plasmas.* Institute of Physics Publishing, Philadelphia, 1993.

[91] Robert D. Cowan. *The Theory of Atomic Structure and Spectra.* University of California Press, Berkeley, first edition, 1981.

[92] F. Coester. Principle of detailed balance. *Phys. Rev.*, 84(6):1259, Dec 1951.

[93] D. R. Inglis and E. Teller. Ionic depression of series limits in cne-electron spectra. *The Astrophysical Journal*, 90:439–448, October 1939.

[94] M. H. Key and R. J. Hutcheon. Spectroscopy of laser-produced plasmas. *Adv. At. Mol. Phys.*, 16:201–280, 1980.

[95] R W P McWhirter and A G Hearn. A calculation of the instantaneous population densities of the excited levels of hydrogen-like ions in a plasma. *Proceedings of the Physical Society*, 82(5):641–654, 1963.

[96] R. W. P. McWhirter. Spectral intensities. In R. H. Huddlestone and S. L. Leonard, editors, *Plasma Diagnostic Techniques*, pages 201–210, 1965.

[97] D. R. Bates, A. E. Kingston, and R. W. P. McWhirter. Recombination between electrons and atomic ions. ii. optically thick plasmas. *Royal Society of London Proceedings Series A*, 270:155–167, November 1962.

[98] L. L. House. Ionization equilibrium of the elements from h to fe. *Astrophysical Journal Supplement*, 8:307–320, January 1964.

[99] D. Colombant and G. F. Tonon. X-ray emission in laser-produced plasmas. *Journal of Applied Physics*, 44(8):3524–3537, 1973.

[100] Gerry O'Sullivan, Padraig Dunne, Emma Sokell, Anthony Cummings, Nicola Murphy, Kenneth Fahy, Paddy Hayden, Michael Lysaght, Luke McKinney, Paul Sheridan, and John White. Recent results on euv emission from laser produced plasmas with slab targets containing sn. Presentation at 3rd EUVL Symposium in Miyazaki in Japan. Proceedings available at www.sematech.org, November 2004.

[101] David J. Nagel, Charles M. Brown, M. C. Peckerar, Marshall L. Ginter, J. A. Robinson, Thomas J. McIlrath, and P. K. Carroll. Repetitively pulsed-plasma soft x-ray source. *Appl. Opt.*, 23(9):1428, 1984.

[102] Winnie Svendsen and Gerard O'Sullivan. Statistics and characteristics of xuv transition arrays from laser-produced plasmas of the elements tin through iodine. *Phys. Rev. A*, 50(5):3710–3718, Nov 1994.

[103] Banqiu Wu and Ajay Kumar. Extreme ultraviolet lithography: A review. *Journal of Vacuum Science and Technology B: Microelectronics and Nanometer Structures*, 25(6):1743–1761, 2007.

[104] Alexander Kramida. Cowan code package for atomic physics. Technical report, http://das101.isan.troitsk.ru/cowan.htm.

[105] Scott Mackay, editor. *High conversion efficiency microscopic tin-doped droplet target laser-plasma source for EUVL*, volume 5751 of *Proc. SPIE*, 2005.

[106] Ralph A. Sawyer. *Experimental Spectroscopy.* Prentice-Hall, Inc., New York, second edition, 1951.

[107] George R. Harrison, Richard C. Lord, and John R. Loofbourow. *Practical Spectroscopy.* Prentice-Hall, Inc., New Jersey, 1948.

[108] Tatsuo Harada and Toshiaki Kita. Mechanically ruled aberration-corrected concave gratings. *Appl. Opt.*, 19(23):3987–, 1980.

[109] W. Schwanda, K. Eidmann, and M. C. Richardson. Characterization of a flat-field grazing-incidence xuv spectrometer. *Journal of X-Ray Science and Technology*, 4(1):8–17, 1993.

[110] T. Kita, T. Harada, N. Nakano, and H. Kuroda. Mechanically ruled aberration-

corrected concave gratings for a flat-field grazing-incidence spectrograph. *Appl. Opt.*, 22(4):512, 1983.

[111] Hitachi aberration corrected concave gratings for flat-filed spectrographs. Technical report, http://www.hitachi-hta.com/media/ConcaveGrating-Spectrograph-Grazing(1).pdf, 2005.

[112] X-ray cameras. Technical report, http://www.piacton.com/products/xraycam/pisx/default.aspx, 2007.

[113] International radiation detectors inc. axuv photodiodes operating principles. Technical report, http://www.ird-inc.com/axuvope.html, 2007.

[114] D. Brandt. Lpp euv source development for hvm, presented at euvl symposium. Presentation at EUVL Source Workshop, Baltimore, MA, Oct. 17 2006.

[115] Simi A. George, William T. Silfvast, Kazutoshi Takenoshita, Robert T. Bernath, Chiew-Seng Koay, Gregory Shimkaveg, and Martin C. Richardson. Comparative extreme ultraviolet emission measurements for lithium and tin laser plasmas. *Opt. Lett.*, 32(8):997–999, 2007.

[116] Martin C. Richardson. Micro-droplet plasmas, March 2005.

[117] Martin C. Richardson, Chiew-Seng Koay, Kazutoshi Takenoshita, C. Keyser, S. George, Somsak Teerawattansook, Moza M. Al-Rabban, and H. Scott. Laser plasma euvl sources: progress and challenges. volume 5374, pages 447–453. SPIE, 2004.

[118] Scott Mackay, editor. *EUV spectroscopy of mass-limited Sn-doped laser micro-plasmas*, volume 5751 of *Proc. SPIE*, 2005.

[119] Kazutoshi Takenoshita, Chiew-Seng Koay, Somsak Teerawattansook, Martin Richardson, and Vivek Bakshi. Debris characterization and mitigation from microscopic laser-plasma tin-doped droplet euv sources. volume 5751, pages 563–571. SPIE, 2005.

[120] Jeff Hecht. Photonic frontiers: High-power fiber lasers: Pumping up the power. Technical report, http://www.laserfocusworld.com/articles/article_display.html?id=234077, 2007.

[121] K-C. Hou. Multi-mw peak power scaling of single-transverse mode pulses using 80-m core yb-doped lma fibers. presented in Post Deadline Paper session at Advanced Solid-State Photonics, 2006.

[122] S. Düsterer, H. Schwoerer, W. Ziegler, C. Ziener, and R. Sauerbrey. Optimization of EUV radiation yield from laser-produced plasma. *Applied Physics B: Lasers and Optics*, 73:693–698, 2001.

[123] P. Dunne, G. O'Sullivan, and D. O'Reilly. Prepulse-enhanced narrow bandwidth soft x-ray emission from a low debris, subnanosecond, laser plasma source. *Applied Physics Letters*, 76:34–+, January 2000.

[124] Aghapi G. Mordovanakis, Kai-Chung Hou, Yu-Chung Chang, Ming-Yuan Cheng, John Nees, Bixue Hou, Anatoly Maksimchuk, Gerard Mourou, Almantas Galvanauskas, and Bruno Lafontaine. Demonstration of fiber-laser-produced plasma source and application to efficient extreme uv light generation. *Opt. Lett.*, 31(17):2517–2519, 2006.

[125] Kazutoshi Takenoshita, Simi A. George, Tobias Schmid, Chiew-Seng Koay, Jose Cunado, Robert Bernath, Christopher Brown, Moza M. Al-Rabban, William T. Silfvast,

and Martin C. Richardson. Characterization of the tin-doped droplet laser plasma euvl sources for hvm. volume 6517, page 65173O. SPIE, 2007.